Effects of Grit Roughness and Pitch Oscillations on the LS(1)-0421MOD Airfoil
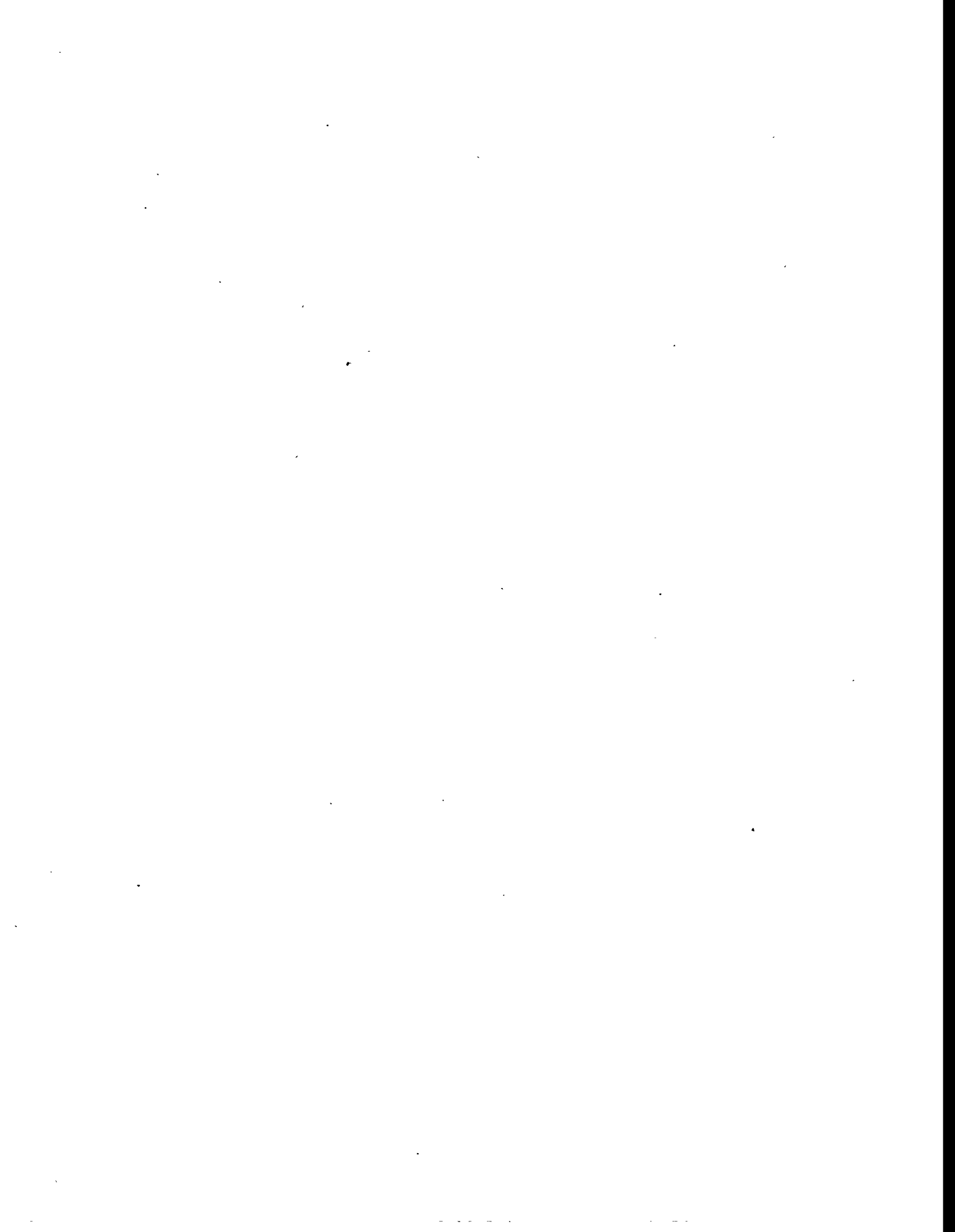
R. L. Reuss
M. J. Hoffman
G. M. Gregorek
The Ohio State University
Columbus, Ohio

MASTER

Effects of Grit Roughness and Pitch Oscillations on the LS(1)-0421MOD Airfoil

R. L. Reuss
M. J. Hoffman
G. M. Gregorek
The Ohio State University
Columbus, Ohio

NREL Technical Monitor:
C. P. Butterfield

◆NREL   MASTER

NOTICE

Available to DOE and DOE contractors from:
> Office of Scientific and Technical Information (OSTI)
> P.O. Box 62
> Oak Ridge, TN 37831

Prices available by calling (615) 576-8401

Available to the public from:
> National Technical Information Service (NTIS)
> U.S. Department of Commerce
> 5285 Port Royal Road
> Springfield, VA 22161
> (703) 487-4650

Printed on paper containing at least 50% wastepaper, including 10% postconsumer waste
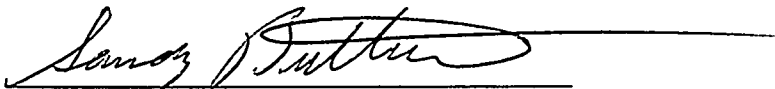
Foreword

Airfoils for wind turbines have been selected by comparing data from different wind tunnels, tested under different conditions, making it difficult to make accurate comparisons. Most wind tunnel data sets do not contain airfoil performance in stall commonly experienced by turbines operating in the field. Wind turbines commonly experience extreme roughness for which there is very little data. Finally, recent tests have shown that dynamic stall is a common occurrence for most wind turbines operating in yawed, stall or turbulent conditions. Very little dynamic stall data exists for the airfoils of interest to a wind turbine designer. In summary, very little airfoil performance data exists which is appropriate for wind turbine design.

Recognizing the need for a wind turbine airfoil performance data base, the National Renewable Energy Laboratory (NREL), funded by the U.S. Department of Energy, awarded a contract to Ohio State University (OSU) to conduct a wind tunnel test program. Under this program, OSU tested a series of popular wind turbine airfoils. A standard test matrix was developed to assure that each airfoil was tested under the same conditions. The test matrix was developed in partnership with industry and is intended to include all of the operating conditions experienced by wind turbines. These conditions include airfoil performance at high angles of attack, rough leading edge (bug simulation), steady and unsteady angles of attack.

Special care has been taken to report as much of the test conditions and raw data as practical so that designers can make their own comparisons and focus on details of the data relevant to their design goals. Some of the airfoil coordinates are proprietary to NREL or an industry partner. To protect the information which defines the exact shape of the airfoil, the coordinates have not been included in the report. Instructions on how to obtain these coordinates may be obtained by contacting C.P. (Sandy) Butterfield at NREL.

C. P. (Sandy) Butterfield
Wind Technology Division
National Renewable Energy Laboratory
1617 Cole Boulevard
Golden, Colorado 80401 USA
Internet Address: Sandy_Butterfield@NREL.GOV
Phone: 303-384-6902
FAX: 303-384-6901

Preface

The Ohio State University Aeronautical and Astronautical Research Laboratory is conducting a series of steady state and unsteady wind tunnel tests on a set of airfoils that have been or will be used for horizontal-axis wind turbines. The purpose is to investigate the effect of angle of attack oscillations and leading edge grit roughness on airfoil performance. The type of unsteady behavior for which the current tests are being conducted can help describe those of a horizontal-axis wind turbine in yaw. The results of these tests will aid in the development of new airfoil performance codes which account for unsteady behavior and aid in the design of new airfoils for wind turbines. The application of leading edge grit roughness simulates surface irregularities that occur on wind turbines. These irregularities on the blades are due to the accumulation of insect debris or ice or due to the aging process and can significantly reduce the output of the horizontal-axis wind turbines. The experimental results from the application of leading edge grit roughness will help in developing airfoils that are insensitive to this kind of roughness.

Summary

The LS(1)-0421MOD airfoil was tested in The Ohio State University Aeronautical and Astronautical Research Laboratory 3x5 subsonic wind tunnel under steady state and unsteady conditions. The purpose of the test was to describe baseline conditions for steady state angles of attack from -10° to +40° and to examine the unsteady behavior by oscillating the model in angle of attack for three mean angles and three frequencies. Three Reynolds numbers, 0.75, 1, and 1.25 million were used for all the cases. Some model oscillating cases were also performed at 1.5 million Reynolds number. In addition, all the above conditions were repeated after the application of leading edge grit roughness (LEGR) to determine its effects on the airfoil performance.

Steady state results of the LS(1)-0421MOD testing at Reynolds number of 1.25 million showed a maximum lift coefficient up to 1.27 at 12.7° angle of attack. The application of LEGR reduced the maximum lift coefficient by up to 27% and nearly doubled the minimum drag coefficient. The zero lift pitching moment showed a reduction in magnitude from -0.077 with model clean to -0.058 with LEGR.

Data were also obtained for two pitch oscillations, ±5.5° and ±10°. The larger amplitude consistently gave a higher maximum lift coefficient than the smaller amplitude, and both were greater than the steady state results. Stall is delayed on the airfoil while the model angle of attack increases, and this causes an increase in maximum lift coefficient. A hysteresis behavior was exhibited for all the unsteady wind tunnel data. The hysteresis loops were larger for the higher reduced frequencies and for the larger amplitude oscillations. As in the steady state case, the LEGR in the unsteady case reduced the lift coefficient at high angles of attack. In addition, the hysteresis behavior persisted into lower angles of attack with LEGR than with the clean case.

In general, the maximum unsteady lift coefficient was from 10% to 50% higher than the steady state maximum lift coefficient. Variation in the quarter chord pitching moment coefficient was nearly two times greater than steady state values at high angles of attack. These findings indicate the importance of considering the unsteady flow behavior occurring in wind turbine operation for accurate load estimates.

Contents

List of Figures

List of Tables

List of Symbols

AOA	Angle of attack
A/C, a.c.	Alternating current
c	Model chord length
C_d	Drag coefficient
C_{dmin}	Minimum drag coefficient
C_{dp}	Pressure drag coefficient
C_{dw}	Wake drag coefficient
C_{du}	Uncorrected drag coefficient
C_l	Lift coefficient
C_{lmax}	Maximum lift coefficient
C_{ldec}	Lift coefficient at angle of maximum lift, but with angle of attack decreasing
C_{lu}	Uncorrected lift coefficient
C_m, $C_{m\frac{1}{4}}$	Pitching moment coefficient about the quarter chord
C_{mdec}	Pitching moment coefficient at angle of maximum lift, but with angle of attack decreasing
C_{mo}	Pitching moment coefficient about the quarter chord, at zero lift
$C_{m\frac{1}{4}u}$	Uncorrected pitching moment coefficient about the quarter chord
C_p	Pressure coefficient, $(p - p_\infty)/q_\infty$
C_{pmin}	Minimum pressure coefficient
f	Frequency
h	Wind tunnel test section height
hp, Hp, HP	Horsepower
Hz	Hertz
k	Grit particle size
p	Pressure
q	Dynamic pressure
q_u	Uncorrected dynamic pressure
q_w	Dynamic pressure through the model wake
q_∞	Free stream dynamic pressure
Re	Reynolds number
Re_u	Uncorrected Reynolds number
t	Time
U_∞	Corrected free stream velocity
V	Velocity
V_u	Uncorrected velocity
x	Axis parallel to model reference line
y	Axis perpendicular to model reference line
α	Angle of attack
α_{dec}	Decreasing angle of attack
α_{inc}	Increasing angle of attack

α_m	Median angle of attack
α_{mean}	Mean angle of attack
α_u	Uncorrected angle of attack
ϵ	Tunnel solid wall correction scalar
ϵ_{sb}	Solid blockage correction scalar
ϵ_{wb}	Wake blockage correction scalar
Λ	Body-shape factor
π	3.1416
σ	Tunnel solid wall correction parameter
ω_{red}, $\omega_{reduced}$	Reduced frequency, $\pi fc/U_\infty$

Introduction

Horizontal-axis wind turbine rotors experience unsteady aerodynamics when the rotor is yawed, when rotor blades pass through the support tower wake, and when the wind is gusting. An understanding of this unsteady behavior is necessary to assist in the calculation of rotor performance and loads and the design of new rotor airfoils. The rotors also experience performance degradation due to surface roughness. These surface irregularities are due to the accumulation of insect debris or ice or the aging process. Wind tunnel studies that examine the unsteady behavior of airfoils can help define the flow phenomena, and the resultant data can also be used to validate analytical computer codes.

An LS(1)-0421MOD airfoil model was tested in The Ohio State University Aeronautical and Astronautical Research Laboratory (OSU/AARL) 3x5 subsonic wind tunnel (3x5) under steady flow and stationary model conditions, and also with the model undergoing pitch oscillations. In order to study the possible extent of performance loss due to surface roughness, a leading edge grit roughness (LEGR) pattern was developed to simulate leading edge contamination. After baseline cases were completed, the LEGR was applied for both steady state and model pitch oscillation cases. The Reynolds numbers for steady state conditions were 0.75, 1, and 1.25 million, while the angle of attack ranged from -10° to +40°. With the model undergoing pitch oscillations, data was acquired at Reynolds numbers of 0.75, 1, 1.25, and 1.5 million, at frequencies of 0.6, 1.2, and 1.8 Hz. Two sine wave forcing functions were used; ±5.5° and ±10°, at mean angles of attack of 8°, 14°, and 20°. For this report, unsteady conditions refer to the model in pitch oscillation.

Experimental Facility

Wind Tunnel

The OSU/AARL 3×5 subsonic wind tunnel (3x5) was used to conduct tests on the LS(1)-0421MOD airfoil section. Schematics of the top and side views are shown in figures 1 and 2. This open-circuit tunnel has a velocity range of 0 to 50 m/s (180 ft/sec) produced by a 2.4 m (8 ft) diameter, six-bladed fan. The fan is belt driven by a 93.2-kw (125-hp), three phase alternating current (AC) motor connected to a variable frequency motor controller. Nominal test section dimensions are 1.0-m (39-inches) high by 1.4-m (55-inches) wide with a 2.4-m (96-inches) length. The 457-mm (18-inch) chord airfoil model was mounted vertically in the test section. A steel tube through the quarter chord of the model was used to attach the model to the tunnel during testing. An angle of attack potentiometer was fastened to the model at the top of the tunnel as shown in figure 2. The steady state angle of attack was adjusted with a worm gear drive attached to the model strut below the tunnel floor.
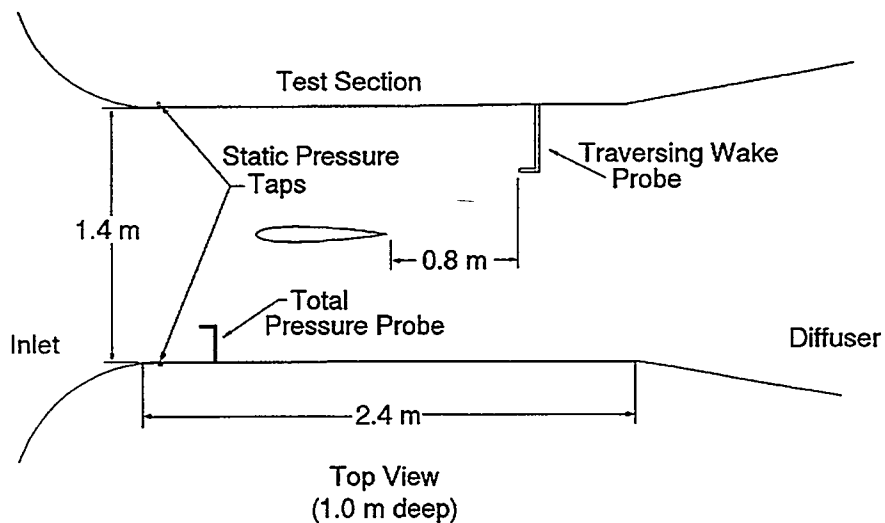

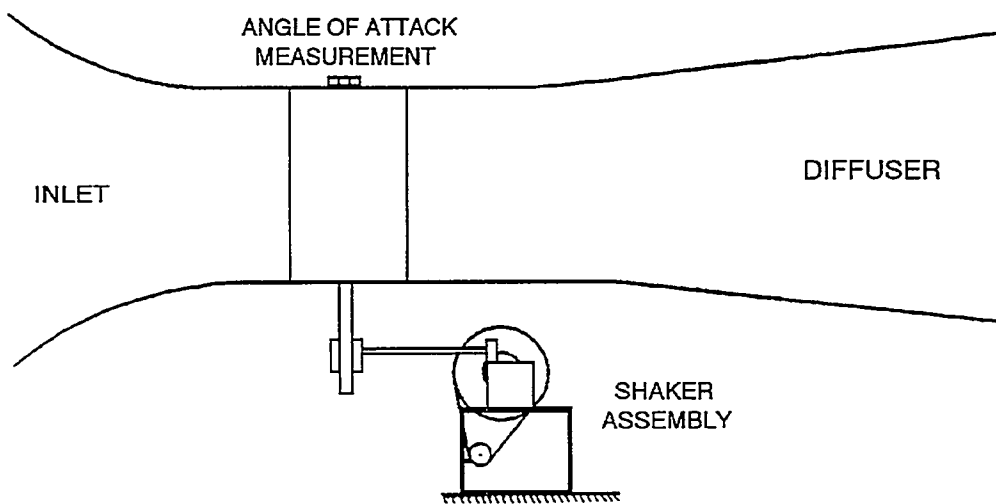Figure 1. 3x5 subsonic wind tunnel, top view

Figure 2. 3x5 subsonic wind tunnel, side view

Oscillation System

Portions of the airfoil model testing required the use of a reliable pitch oscillation system. The OSU/AARL "shaker" system incorporated a face cam and follower arm attached to the model support tube below the wind tunnel floor, as shown in figure 3. The choice of cam governed the type and amplitude of the wave form produced. Sine wave forms with amplitudes of $\pm 5.5^\circ$ and $\pm 10^\circ$ were used for these tests, the wave form being defined by the equation

$$\alpha = \alpha_m + A\sin(2\pi f t)$$

where A is the respective amplitude. The shaker system was powered by a 5-hp AC motor with a variable line frequency controller. The useable oscillating frequency range was 0.1 to 2.0 Hz, with three frequencies used for this test: 0.6, 1.2, and 1.8 Hz.
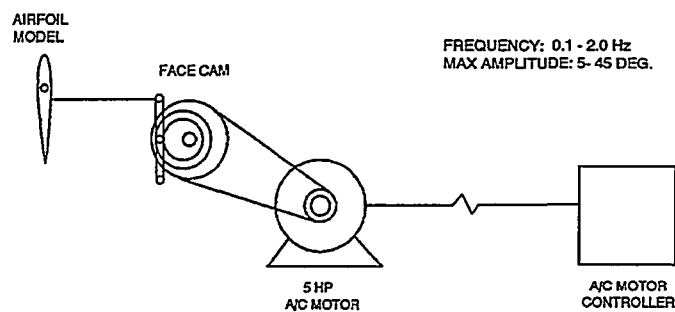
Figure 3. 3x5 wind tunnel oscillation system

Model Details

A 457-mm (18-inch) constant chord LS(1)-0421MOD airfoil model was designed by OSU/AARL personnel and manufactured by others. Figure 4 shows the airfoil section; the model measured coordinates are given in Appendix A. The model was made of a carbon composite skin over ribs. The main load bearing member was a 38-mm (1.5-inch) diameter steel tube that passed through the model quarter chord station. Ribs and end plates were used to transfer loads from the composite skin to the steel tube. The final surface was hand worked using templates to attain given coordinates within a tolerance of ± 0.25 mm (± 0.01 inches). The completed model was measured using a Sheffield-Cordax coordinate measurement machine. Measurements were made in english units and later converted to metric. Figure 5 shows the results of comparing measured-to-desired coordinates by calculating differences normal to the profiled surface.
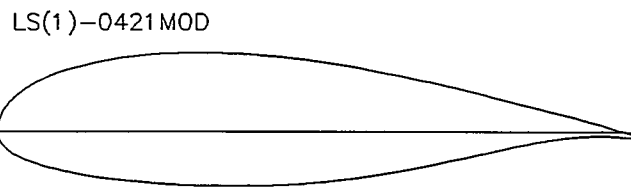
LS(1)−0421MOD

Figure 4. LS(1)-0421MOD airfoil section
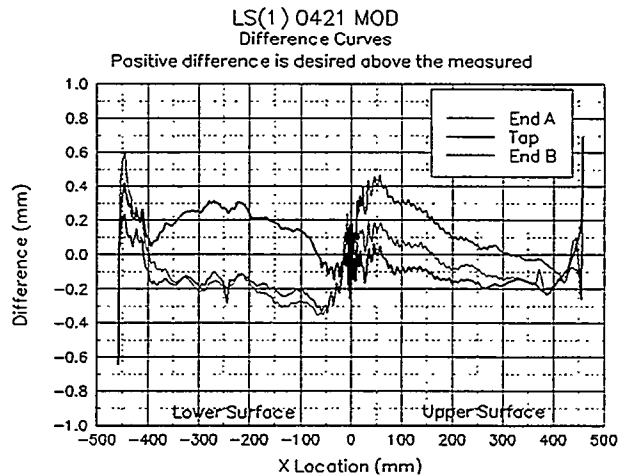
Figure 5. Measured-to-desired model coordinates difference curves.

To minimize pressure response times, which is important for the unsteady testing, the lengths of surface pressure tap lead-out lines had to be as short as possible. Therefore, a compartment was built into the model to hold pressure scanning modules. This compartment was accessed through a panel door fitted flush with the model contour on the lower (pressure) surface.

For test cases involving roughness, a standard, repeatable pattern with grit as roughness elements was desired. OSU/AARL and KENETECH Windpower personnel jointly developed a roughness pattern using a molded insect pattern taken from a wind turbine in the field by personnel at the University of Texas, Permian Basin. The resultant particle density was 5 particles per cm^2 (32 particles per square inch) in the middle of the pattern, thinning to 1.25 particles per cm^2 (8 particles per square inch) at the edge of the pattern. Figure 6 shows the resultant pattern. To make a usable template, the pattern was repeatedly cut into a steel sheet 102 mm (4 inches) wide and 91 cm (3 ft) long with holes just large enough for one

4

piece of grit. Based on average particle size from the field specimen, standard #40 lapidary grit was chosen for the roughness elements, giving k/c=0.0019 for a 457-mm (18-inch) chord model.
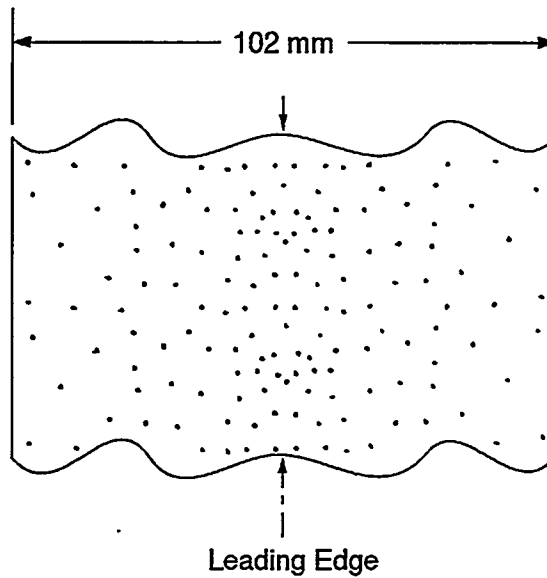
Figure 6. Roughness pattern

To use the template, 102-mm (4-inch) wide double-tack tape was applied to one side of the template and grit was poured and brushed from the opposite side. The tape was then removed from the template and transferred to the model. This method allowed the same roughness pattern to be replicated for any test.

Test Equipment and Procedures

Data Acquisition

Data were acquired and processed from 60 surface pressure taps, four individual tunnel pressure transducers, an angle of attack potentiometer, a wake probe position potentiometer, and a tunnel thermocouple. The data acquisition system included an IBM PC compatible 80486-based computer connected to a Pressure Systems Incorporated (PSI) data scanning system. The PSI system included a 780B Data Acquisition and Control Unit (DACU), 780B Pressure Calibration Unit (PCU), 81-IFC scanning module interface, two 2.5-psid pressure scanning modules (ESPs), one 20-inch water column range pressure scanning module, and a 30-channel Remotely Addressed Millivolt Module (RAMM-30). figure 7 shows the data acquisition system schematic.
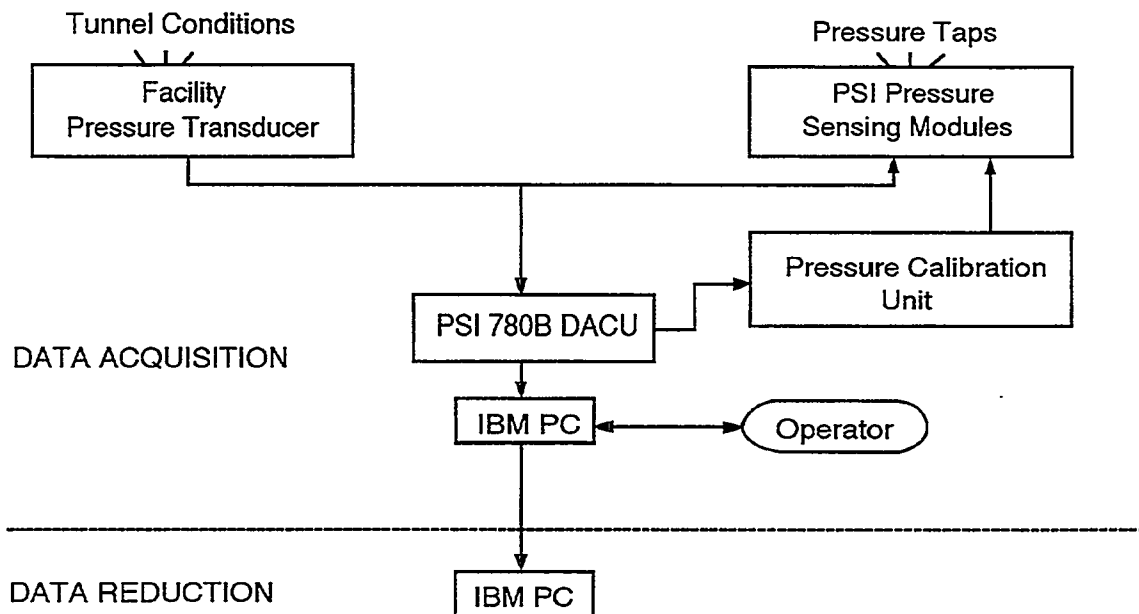
Figure 7. Data acquisition schematic

Four individual pressure transducers read tunnel total pressure, tunnel north static pressure, tunnel south static pressure, and wake dynamic pressure. Before the test began, these transducers were bench calibrated using a water manometer to determine their sensitivities and offsets. Related values were entered into the data acquisition and reduction program so the transducers could be shunt resistor calibrated before each series of wind tunnel runs.

The rotary angle of attack potentiometer of 0.5% linearity was regularly calibrated during the tunnel pressure transducers shunt calibration. The angle of attack calibration was accomplished by taking voltage readings at known values of set angle of attack. This calibration method gave angle of attack readings within $\pm 0.25°$ over the entire angle range. The wake probe position potentiometer was also a linear potentiometer and was also regularly calibrated during the shunt calibration of the tunnel pressure transducers.

Calibration of the three ESPs was done simultaneously using the DACU and PCU. At operator request, the DACU commanded the PCU to apply known regulated pressures to the ESPs and read the output voltages from each integrated pressure sensor. From these values, the DACU calculated the calibration

6

coefficients and stored them internally until the coefficients were requested by the controlling computer. This calibration was done several times during a run set because the ESPs were installed inside the model and their outputs tended to drift with temperature changes during a test sequence. Frequent on-line calibrations minimized the effect.

For steady state cases, the model was set to angle of attack and the tunnel conditions were adjusted. At operator request, pressure measurements from the airfoil surface taps and all other channels of information were acquired and stored by the DACU and subsequently passed to the controlling computer for final processing. The angles of attack were always set in the same progression from negative to positive values.

For model oscillating cases, the tunnel conditions were set while the model was stationary at the desired mean angle of attack. After the "shaker" was started, a timed wait of approximately 10 seconds was imposed before data was acquired.

Data Reduction

The data reduction routine was included as a section of the data acquisition program. The combined data acquisition and reduction routines allowed data to be reduced on line during a test. By quickly reducing selected runs, integrity checks could be made to ensure the equipment was working properly and to enable timely decisions about the test matrix.

The ambient pressure was manually input into the computer and was updated regularly. This value, as well as the measurements from the tunnel pressure transducers and the tunnel thermocouple, were used to calculate tunnel airspeed. As a continuous check of readings, the tunnel total and static pressures were read by both the tunnel individual pressure transducers and the 20-inch water column ESP.

A typical steady state data point was derived by acquiring 10 data scans of all channels over a 10-second window at each angle of attack and tunnel condition. The reduction portion of the program processed each data scan to coefficient forms C_p, C_l, $C_{m¼}$, and C_{dp} using the measured surface pressure voltages, calibration coefficients, tap locations and wind tunnel conditions. All scan sets for a given condition were then ensemble averaged to provide one data set; that data set was corrected for the effects of solid tunnel walls. All data was saved in electronic form and selected final data was printed to paper.

Corrections due to solid tunnel sidewalls were applied to the wind tunnel data as found in the text by Pope and Harper (1966). Tunnel conditions are described by the following equations:

$$q=q_u(1+2\epsilon)$$

$$V=V_u(1+\epsilon)$$

$$R_e=R_{e_u}(1+\epsilon)$$

Airfoil aerodynamic characteristics are corrected by:

$$\alpha=\alpha_u+\frac{57.3\sigma}{2\pi}(C_{l_u}+4C_{m\frac{1}{4}_u})$$

$$C_l=C_{l_u}(1-\sigma-2\epsilon)$$

$$C_d=C_{d_u}(1-3\epsilon_{sb}-2\epsilon_{wb})$$

7

$$C_{m_{\frac{1}{4}}} = C_{m_{\frac{1}{4}}{}_u} (1-2\epsilon) + \frac{\sigma C_l}{4}$$

where

$$\sigma = \frac{\pi^2}{48} (\frac{c}{h})^2$$

$$\epsilon = \epsilon_{sb} + \epsilon_{wb}$$

$$\epsilon_{sb} = \Lambda\sigma$$

$$\epsilon_{wb} = \frac{c}{h4} C_{d_u}$$

Model wake data was taken for steady state cases when the wake could be completely traversed. Pressures were acquired from a pitot-static probe that was connected to measure incompressible dynamic pressure through the wake. These pressure measurements were used to calculate drag coefficient using a form of the Jones equation derived from Schlichting (1979):

$$C_{dw} = \frac{2}{c} \int_0^c \sqrt{\frac{q_w}{q_\infty}} \left(1 - \sqrt{\frac{q_w}{q_\infty}}\right) dy$$

This assumes static pressure at the measurement site is the free-stream value. The integration was done automatically, except that the computer operator chose the end points of the integration from a plot of the wake survey displayed on the computer screen.

Test Matrix

The test was designed to study steady state and unsteady pitch oscillation data. Steady state data were acquired at Reynolds numbers of 0.75, 1, and 1.25 million with and without LEGR. The tabular data in Appendix B contains the actual Reynolds number for each angle of attack for the steady state data. The angle of attack increment was 2 degrees when $-10° < \alpha < +10°$ or $+20° < \alpha < +40°$, and one degree when $+10° < \alpha < +20°$. Wake surveys were conducted to find total airfoil drag over an approximate angle of attack range of $-10°$ to $+10°$. Unsteady data was taken for Reynolds numbers of 0.75, 1, 1.25, and 1.5 million. Sine wave cams with amplitudes of $\pm5.5°$ and $\pm10°$ were used for pitch oscillations, and the mean angles for both these amplitudes were $8°$, $14°$, and $20°$. For all conditions, the frequencies were varied to 0.6, 1.2 and 1.8 Hz. All data points for the unsteady cases were acquired for both clean and LEGR cases.

Results and Discussion

The LS(1)-0421MOD was tested under steady state and pitch oscillation conditions. A brief analysis of the results follows, beginning with a comparison of experimental data with computational predictions.

Comparisons with Theory

Steady state wind tunnel data was compared to computed predictions of the North Carolina State Airfoil Analysis Code. This analysis code has proven to be accurate for moderate angles of attack. Analytical run specifications were set to allow for free transition from laminar to turbulent flow, and the pressure distribution comparisons were matched to the angle of attack of the wind tunnel test data.
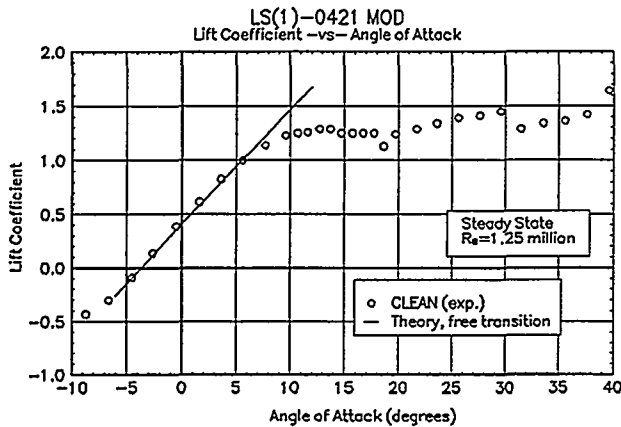
Figure 8. Comparison with theory, C_l vs α
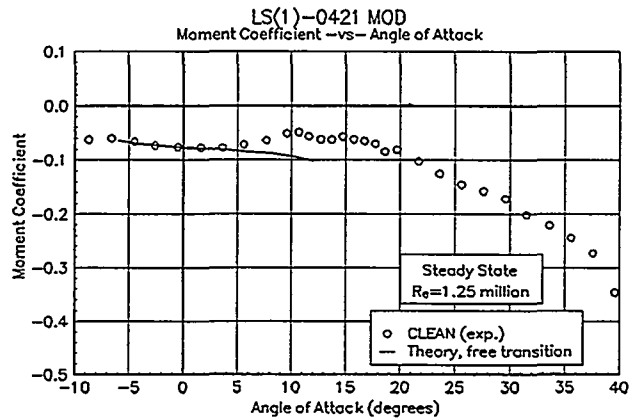
Figure 9. Comparison with theory, C_m vs α
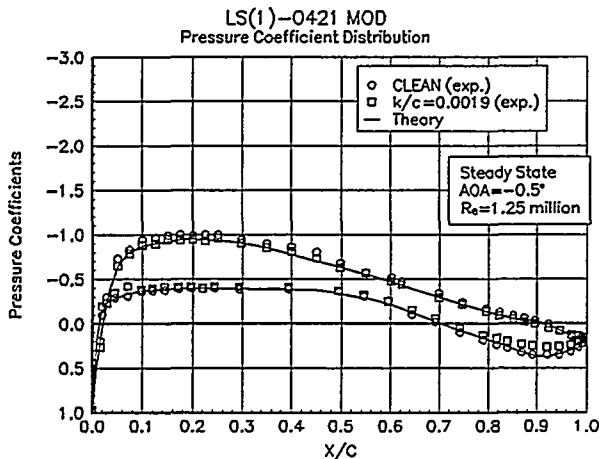
Figure 10. Comparison with theory, C_p vs x/c, $\alpha = -0.5°$
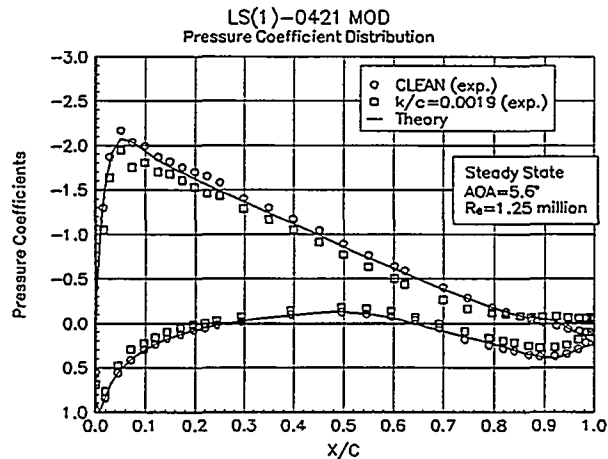
Figure 11. Comparison with theory, C_p vs x/c, $\alpha = 5.6°$

Figure 8 shows the lift coefficient versus angle of attack for the 1.25 million Reynolds number case. For moderate angles of attack, where the analysis code is valid, the comparison shows good agreement. The pitching moment about the quarter chord, figure 9, also shows good agreement for moderate angles of attack, -5° to +5°. The pressure distributions shown in figures 10 and 11 show angles of attack of -0.5° and +5.6°, with both clean and LEGR data shown with the predicted pressure distributions. The -0.5° comparison shows excellent correlation between the clean experimental data and predicted data on the lower surface. The upper surface shows agreement in the trailing edge, but the magnitude of the

experimental pressure coefficient is slightly higher through the forward portion of the upper surface. The 5.6° pressure distribution case shows only small discrepancies near the pressure peak where the experimental data is slightly higher than the predicted. In general, the agreement between the experimental and predicted data is good.

Steady-State Data

The LS(1)-0421MOD airfoil model was tested at three Reynolds numbers at nominal angles of attack from -10° to +40°. Figures 12 and 13 show lift coefficient for all the test Reynolds numbers, both for the clean model and with LEGR applied, respectively. The maximum positive lift coefficient for the clean cases is about 1.26; the LEGR data has a C_{lmax} of about 0.98, a 22% reduction. The stall characteristic is similar for both clean and LEGR cases; both have a gradual stall behavior. Finally, the average lift curve slope for these data is about 0.11 for the clean case and slightly lower at 0.10 for the LEGR case; consequently, C_l at zero angle of attack is lower for the LEGR case.
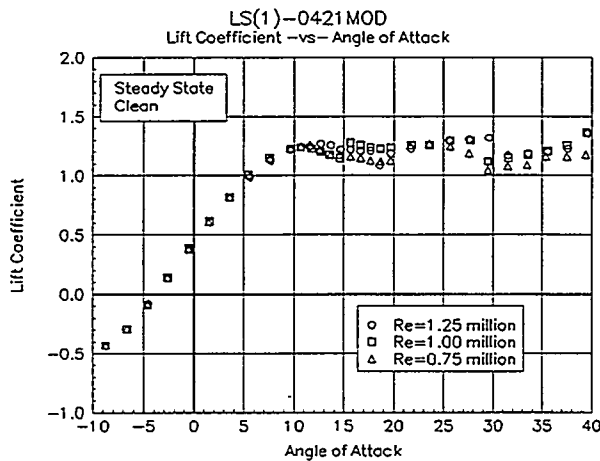
Figure 12. C_l vs α, clean
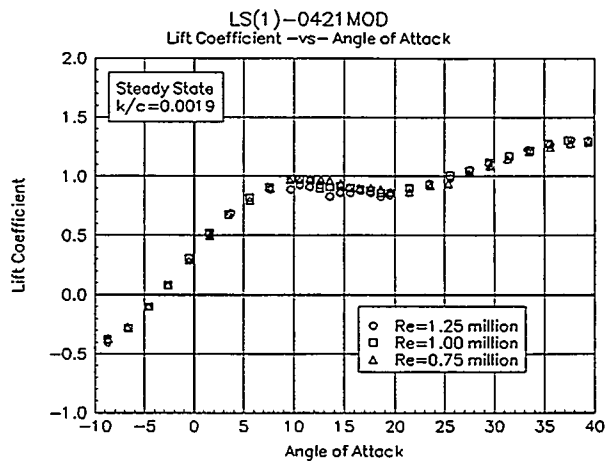
Figure 13. C_l vs α, LEGR, k/c=0.0019
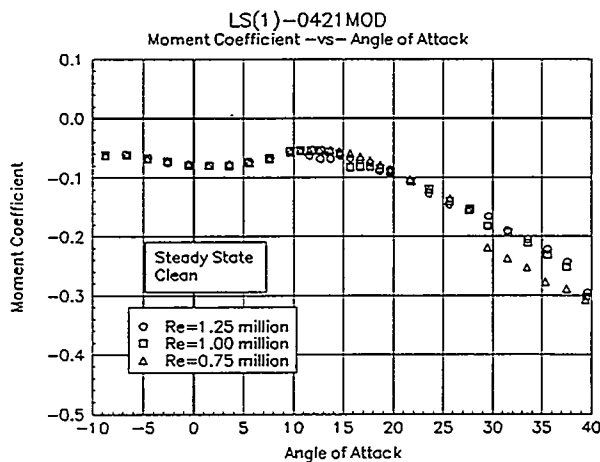
Figure 14. C_m vs α, clean
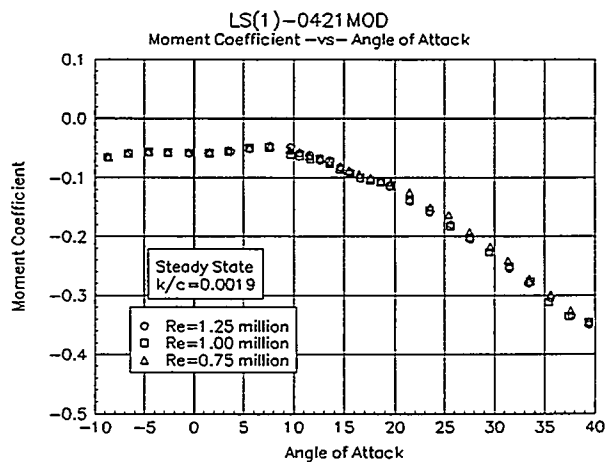
Figure 15. C_m vs α, LEGR, k/c=0.0019

Figure 14 shows the pitching moment about the quarter chord for the clean cases, and figure 15 shows the LEGR cases. The LEGR data show a more positive pitching moment near zero lift, but beyond stall, the pitching moment magnitude increases faster for the LEGR model than for the clean model. The C_{mo} about the quarter chord for the 1 million Reynolds number, for the clean case is -0.0666 and -0.0566 for the LEGR case.

10

Total wake drag data was obtained for both the clean and LEGR cases over a nominal angle of attack range of -10° to +10°. A pitot-static probe was used to describe the wake profile; this method is only reliable for low wake-flow turbulence and when the wake can be completely traversed. At angles higher or lower than the nominal range, calculated pressure drag was used. Pressure drag values are shown in the drag polar figures as small symbols. The clean model drag data are shown in figure 16 and the LEGR data are shown in figure 17. Minimum drag coefficient was measured as 0.0100 for the clean data and 0.0163 for LEGR, a 63% increase.
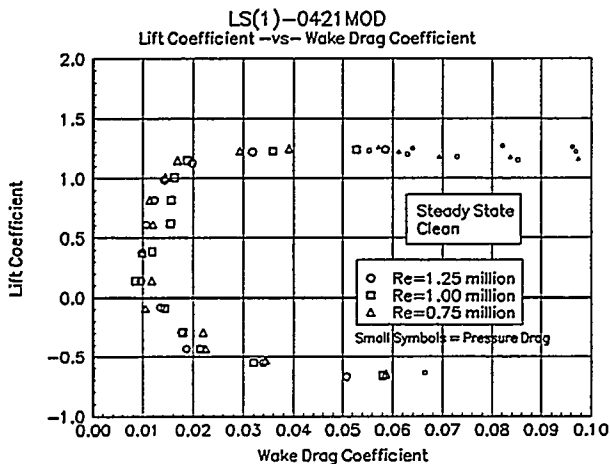
Figure 16. Drag polar, clean
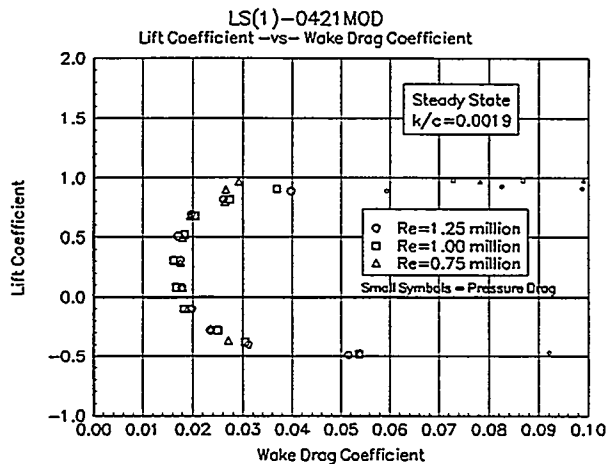
Figure 17. Drag polar, LEGR
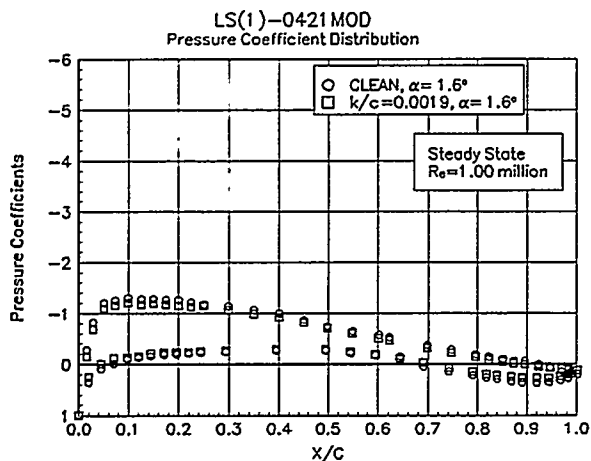
Figure 18. Pressure distribution, $\alpha = 2°$
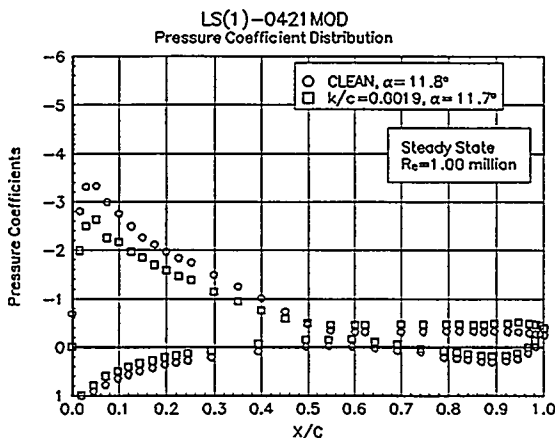
Figure 19. Pressure distribution, $\alpha = 12°$

Two examples of the surface pressure distributions are shown in figures 18 and 19 for 1.6° and 11.7°, respectively, at 1 million Reynolds number. The effect of LEGR is not as detectable at the lower angle of attack as at the higher angle. The effect of LEGR is at least manifested in the lift coefficient which is 0.52 for the LEGR case and 0.62 for the clean case. This is due to the decambering effect from the greater momentum thickness of the boundary layer in the LEGR cases. For the higher angle of attack shown in figure 19, LEGR also reduces the magnitude of the pressure peak from -3.4 to -2.6, which corresponds to a reduction in lift coefficient from 1.23 to 0.97, a 21% decrease. As can be seen in the pressure distribution for the higher angle of attack, the flow separates over the last 40% of the upper surface. The pitching moment also is affected and becomes -0.0676 for the LEGR case in comparison to the clean case of -0.0538. These kinds of magnitude changes are very relevant when looking at the performance of the wind turbine blades.

11

Unsteady Data

Unsteady experimental data were obtained for the model undergoing a sinusoidal pitch variation. No attempt was made to calibrate the wind tunnel for the unsteady oscillating model conditions; the steady state tunnel calibration was used. A comprehensive set of test conditions were used to describe unsteady behavior of the airfoil, including two angle of attack amplitudes, $\pm 5.5°$ and $\pm 10°$; four Reynolds numbers, 0.75, 1, 1.25, and 1.5 million; three mean frequencies, 0.6, 1.2, and 1.8 Hz; and three mean angles of attack, 8°, 14°, and 20°. Flow conditions were set with the model stationary at the mean angle setting.

Figure 20 shows the lift coefficient versus angle of attack for the $\pm 5.5°$ amplitude clean case at reduced frequency 0.027 and 1 million Reynolds number. Note that all three mean angles of attack are plotted on the same figure. The maximum pre-stall lift coefficient for this case is near 1.44 and occurs when the airfoil is traveling with angle of attack increasing. In contrast, when the model is traveling through decreasing angles of attack, the stall recovery is delayed and a hysteresis behavior is exhibited which can be seen throughout all the unsteady data. The lift coefficient on the return portion of the curve, at the angle of maximum lift coefficient, can be used in order to obtain some measure of this hysteresis behavior. For the first case the "hysteresis" lift coefficient is 1.17, which is a 19% decrease. In comparison, the steady state maximum lift coefficient is 1.24. This difference in steady state characteristics and the unsteady hysteresis behavior is one reason that unsteady testing is required for airfoils used for wind turbine applications. At higher reduced frequency, the hysteresis behavior is more pronounced as seen in figure 21. In addition, the maximum lift coefficient increases to nearly 1.67, which is a 33% increase over the steady state behavior. The corresponding "hysteresis" lift coefficient is 1.20.
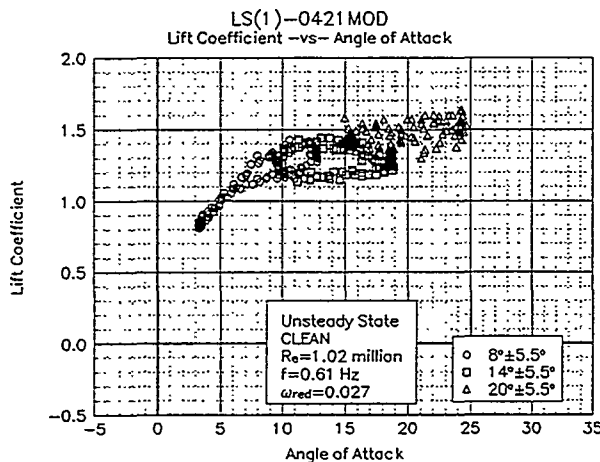
Figure 20. Clean, C_l vs α, $\omega_{red}=0.027$, $\pm 5.5°$ Figure 21. Clean, C_l vs α, $\omega_{red}=0.082$, $\pm 5.5°$
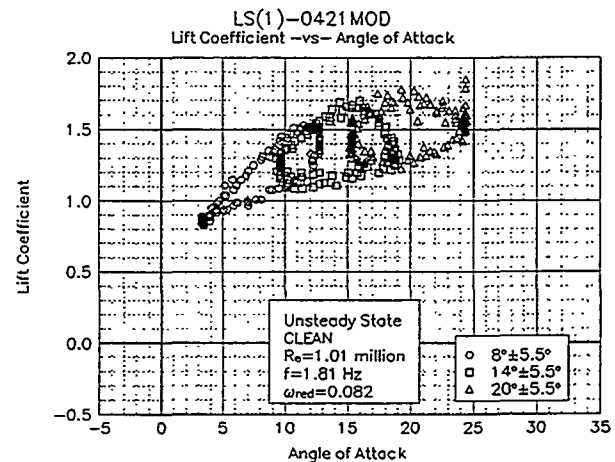
The pitching moments in figures 24 and 25 correspond to the same test conditions as the two lift coefficient plots just discussed. The figures indicate that the hysteresis behavior is present. However, it is not as apparent in these plots as in the lift coefficient plots. The higher reduced frequency data show hysteresis more than the lower reduced frequency case. The steady state maximum lift of this airfoil occurs near 12° angle of attack and the steady state pitching moment at this maximum lift point is -0.0536. At the lower frequency, the pitching moment varies from -0.0375 to -0.0709, at the maximum lift coefficient angle of attack, a 30% reduction and a 32% increase, respectively, from the steady state values. Note that the angle of attack where the maximum lift coefficient occurs is not the place were the hysteresis is the greatest.

12

LS(1)—0421 MOD
Lift Coefficient —vs— Angle of Attack

Unsteady State
K/C=0.0019
Re=1.00 million
f=0.61 Hz
ωred=0.027

o 8°±5.5°
□ 14°±5.5°
△ 20°±5.5°

Lift Coefficient
Angle of Attack

LS(1)—0421 MOD
Lift Coefficient —vs— Angle of Attack

Unsteady State
K/C=0.0019
Re=1.00 million
f=1.85 Hz
ωred=0.083

o 8°±5.5°
□ 14°±5.5°
△ 20°±5.5°

Lift Coefficient
Angle of Attack
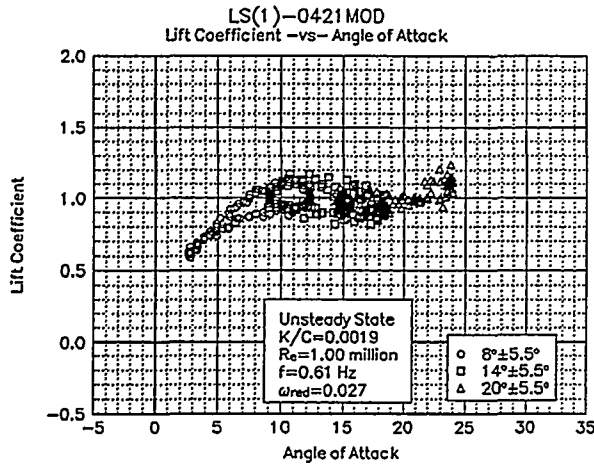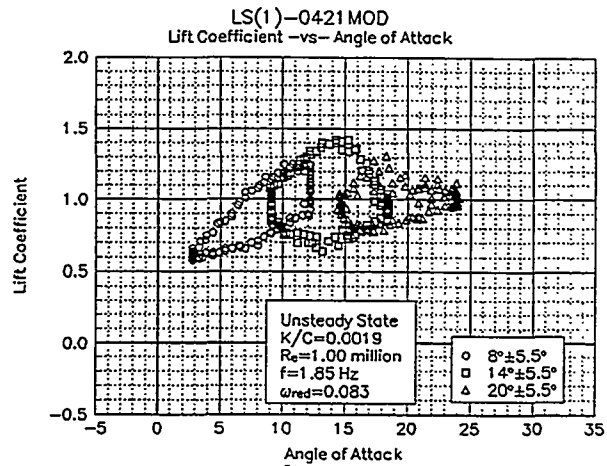
Figure 22. LEGR, C_l vs α, ω_{red}=0.027, ±5.5°   Figure 23. LEGR, C_l vs α, ω_{red}=0.083, ±5.5°

In comparison to the clean data, the application of LEGR reduces the maximum lift coefficient in the unsteady cases. The 0.027 reduced frequency case of LEGR effect on lift coefficient is shown in figure 22, the 0.083 reduced frequency case is in figure 23. For the lower reduced frequency, the maximum lift coefficient is 1.13, a 24% decrease from the unsteady maximum from the corresponding clean case of 1.43. Hysteresis behavior is apparent at this frequency and is of similar order to the clean case. The corresponding decreasing angle of attack lift coefficient is 0.93 when LEGR is applied, which is the same magnitude reduction as the clean case. In contrast, the higher frequency LEGR case has a maximum lift coefficient of 1.40 while the model is increasing in angle of attack; the corresponding decreasing angle of attack lift coefficient is 0.68. In this case, the application of LEGR results in a greater hysteresis loop behavior than the clean case.

LS(1)—0421 MOD
Moment Coefficient —vs— Angle of Attack

Unsteady State
CLEAN
Re=1.02 million
f=0.61 Hz
ωred=0.027

o 8°±5.5°
□ 14°±5.5°
△ 20°±5.5°

Moment Coefficient
Angle of Attack

LS(1)—0421 MOD
Moment Coefficient —vs— Angle of Attack

Unsteady State
CLEAN
Re=1.01 million
f=1.81 Hz
ωred=0.082

o 8°±5.5°
□ 14°±5.5°
△ 20°±5.5°

Moment Coefficient
Angle of Attack
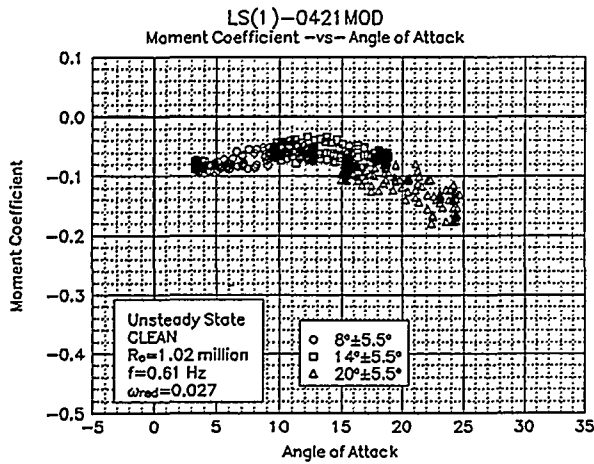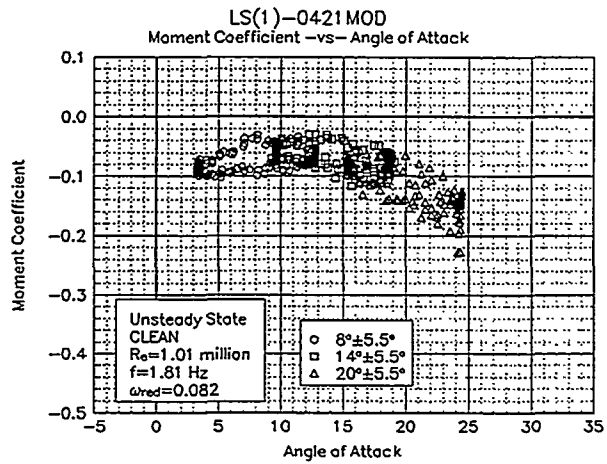
Figure 24. Clean, C_m vs α, ω_{red}=0.027, ±5.5°   Figure 25. Clean, C_m vs α, ω_{red}=0.082, ±5.5°

The pitching moment coefficient shown in figure 26 is for 0.027 reduced frequency and LEGR, which corresponds to the low frequency cases discussed previously. When comparing the clean and LEGR cases, the trend of these curves is slightly different and the hysteresis is slightly less apparent for the LEGR case than the clean case. The airfoil stalls sooner with the LEGR than it does clean, which accounts for the different trends in the figures 24 and 26. At the location of unsteady maximum lift, the pitching moment ranges from -0.0661 to -0.0967, where as the steady state LEGR pitching moment is -0.0619 at the steady state stall angle of attack. The higher frequency of 0.083 with LEGR application is shown in figure 27. Hysteresis is more apparent at the higher reduced frequency than the corresponding clean case in figure 25. Unsteady maximum lift angle of attack for this reduced frequency

13

is at 14.3°, and the pitching moment ranges from -0.1503 to -0.0455. These magnitudes are much greater than the -0.0531 shown by wind tunnel steady state, clean airfoil pitching moment at maximum lift. This can have a significant impact on the fatigue life predictions of a wind turbine system.
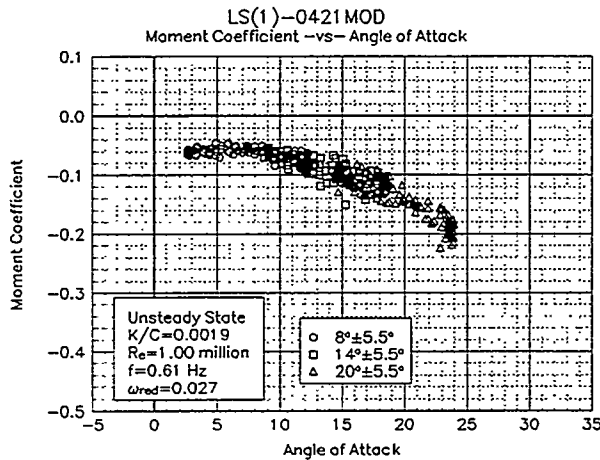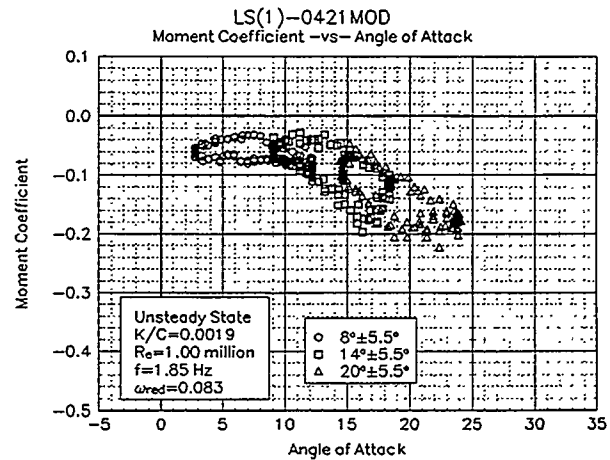
Figure 26. LEGR, C_m vs α, $\omega_{red}=0.027$, ±5.5°   Figure 27. LEGR, C_m vs α, $\omega_{red}=0.083$, ±5.5°

In addition to the ±5.5° unsteady experimental data, ±10° unsteady data were obtained with and without LEGR. The first data examined for this larger amplitude are the baseline, clean data. All the data discussed are for 1 million Reynolds number. Although a larger angle of attack range was spanned for each mean angle, the same mean angles were used as for the smaller amplitude cases.
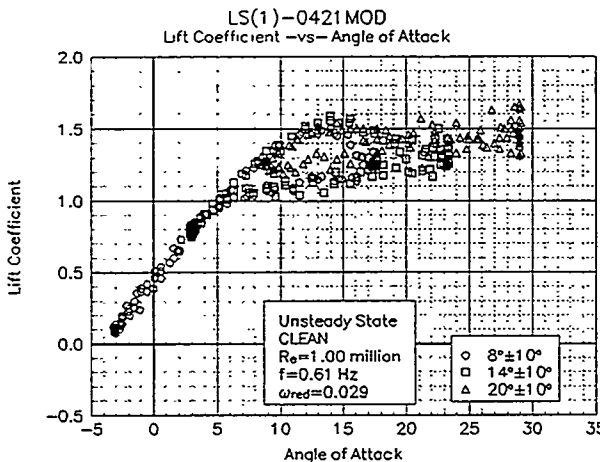
Figure 28. Clean, C_l vs α, $\omega_{red}=0.029$, ±10°   Figure 29. Clean, C_l vs α, $\omega_{red}=0.085$, ±10°
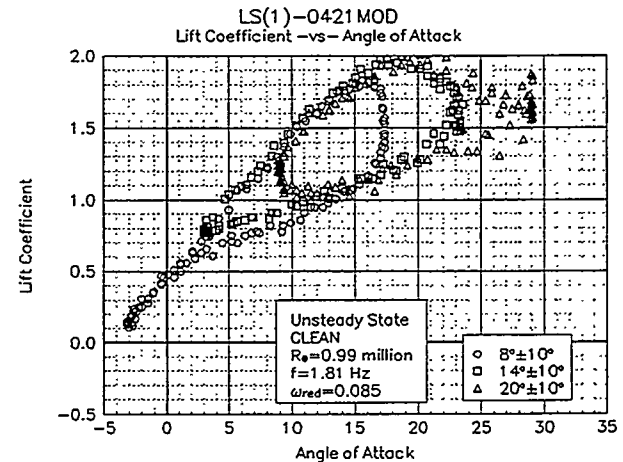
Figures 28 and 29 show the ±10°, unsteady, clean, lift coefficient for the reduced frequencies of 0.029 and 0.085, respectively. The maximum lift coefficient for the lower frequency is 1.59 and occurs at 14°, as the airfoil is traveling with increasing angle of attack. The lift coefficient is 1.20 at the same angle of attack (14°) for the airfoil in decreasing angle of attack. At the higher reduced frequency, the maximum lift coefficient, 1.94, occurs at a higher angle of attack, 18°. The corresponding decreasing lift coefficient is 1.21. This indicates a much larger hysteresis loop than experienced for the lower reduced frequency. The steady state, clean, maximum lift coefficient is 1.24; therefore, the unsteady behavior created a lift coefficient up to 57% higher than the steady state.

The quarter chord pitching moment with the same reduced frequencies as the clean lift coefficient cases previously discussed are shown in figure 30, reduced frequency of 0.029, and figure 31, reduced

14

frequency of 0.085. The hysteresis behavior observed in the lift coefficient plots is reflected in these pitching moment data. Near the maximum lift angle of 14° for the lower frequency, the pitching moment coefficient ranges from -0.0856 to -0.0435. The 0.085 reduced frequency case has a maximum lift near 18° and a pitching moment ranging from -0.0501 to -0.1239. The higher reduced frequency, again, shows large hysteresis loops for all three mean angles of attack. In comparison, the steady state pitching moment is -0.0531 near the steady state maximum lift coefficient angle of attack of 11°.
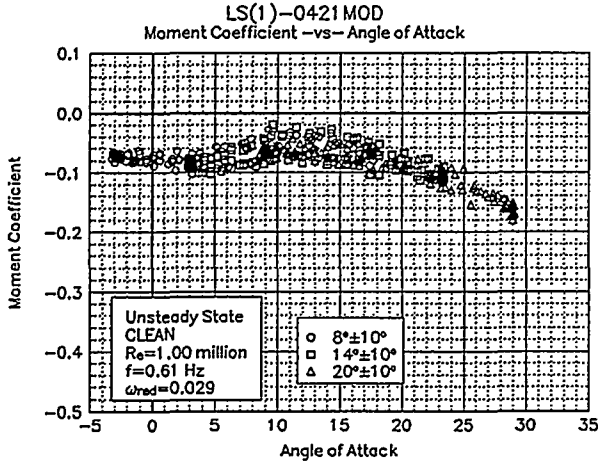
Figure 30. Clean, C_m vs α, ω_{red}=0.029, $\pm 10°$ Figure 31. Clean, C_m vs α, ω_{red}=0.085, $\pm 10°$
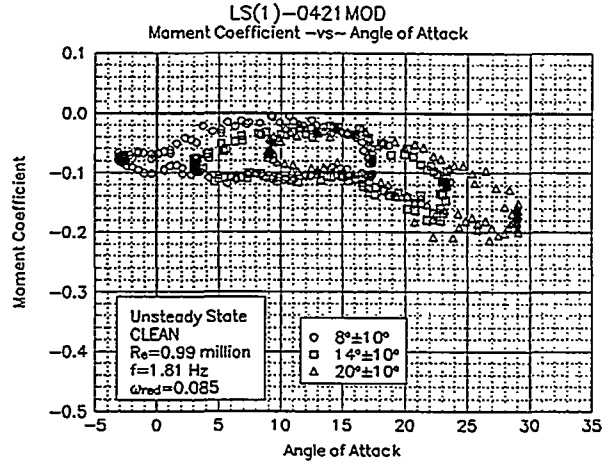
The application of LEGR degrades the lift performance of the airfoil, as would be expected from the results discussed previously. The LEGR lift coefficient data for reduced frequencies of 0.026 and 0.079 are shown in figures 32 and 33, respectively. For the low frequency case, the maximum lift coefficient is reduced to 1.23 from 1.59 clean. Although there is a reduction, this value is still significantly higher than the LEGR steady state case, which has a maximum lift coefficient of 0.98 at 10.6° angle of attack. The higher reduced frequency has a maximum lift coefficient of 1.65, which occurs near 18° angle of attack. Corresponding lift coefficient at 18° for the airfoil traveling through decreasing angle of attack is 0.66, which is a 60% reduction from the increasing angle of attack case. This case shows much larger hysteresis loops than have previously been observed in this data.
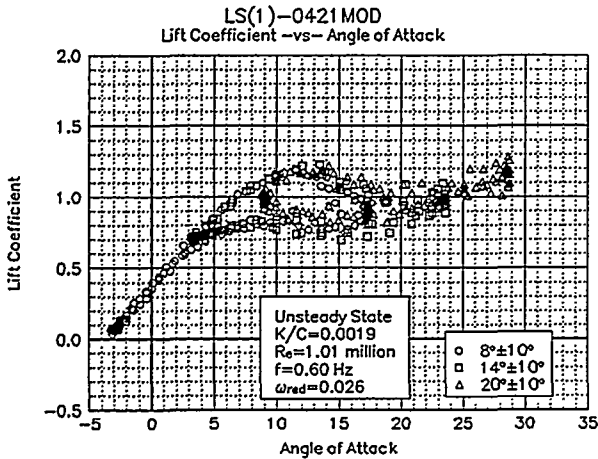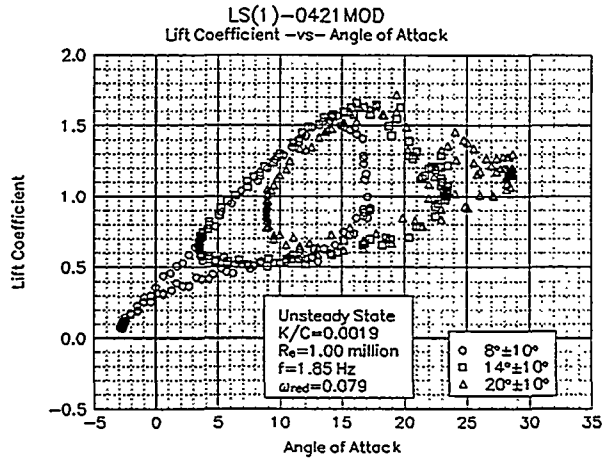
Figure 32. LEGR, C_l vs α, ω_{red}=0.026, $\pm 10°$ Figure 33. LEGR, C_l vs α, ω_{red}=0.079, $\pm 10°$

Figures 34 and 35 show the corresponding pitching moment coefficients for the reduced frequencies of 0.026 and 0.079, respectively. For the 0.026 case, the pitching moment varies from -0.0503 to -0.1042 at 13° (where the maximum lift occurs). Again, the hysteresis behavior is more pronounced for the

15

higher frequency case where the range of pitching moments at the maximum lift location of 18° is from -0.2123 to -0.0757. These values can be compared to the steady state LEGR case at the maximum lift location pitching moment coefficient of -0.0619. In addition to the changes in magnitude, the trends of the pitching moment curves differ from the clean to LEGR cases. Comparing figures 30 and 34, the magnitude of the pitching moment is more constant for the LEGR case prior to airfoil stall than it is for the clean case. Beyond stall the magnitude of the LEGR case increases at a higher rate than the clean case.
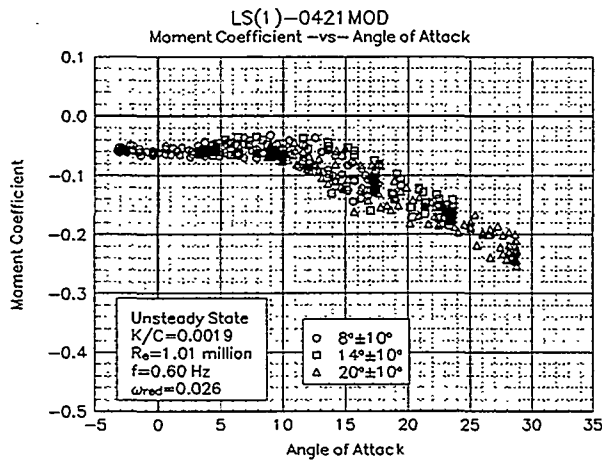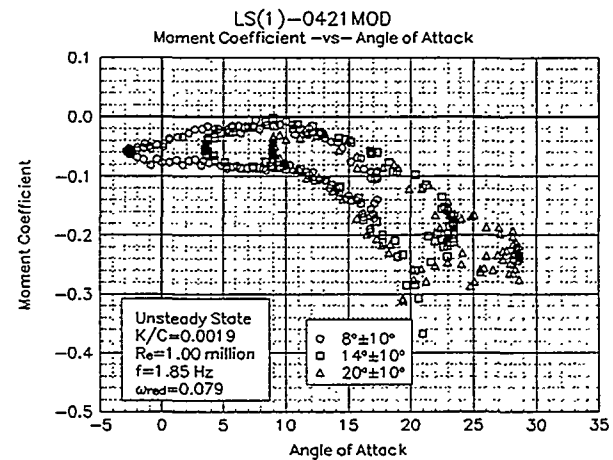
Figure 34. LEGR, C_m vs α, ω_{red}=0.026, ±10°   Figure 35. LEGR, C_m vs α, ω_{red}=0.079, ±10°

Although all the unsteady data have not been discussed here, the this section provides a good example of the wind tunnel data obtained. The remaining data are included in Appendix C.

The following three unsteady pressure distributions show three examples of the data used to calculate the lift, pressure drag, and the pitching moment coefficients. Figure 37 shows the distribution for the clean case, 0.028 reduced frequency, 8° mean angle of attack, and ±10° pitch oscillation. The upper surface leading edge is depicted on the right of the surface plot; the trailing edge for the upper and lower surface is at the centerline of the x-axis; and side the lower surface leading edge is plotted to the left. The upper surface pressure peaks correspond to the maximum angles of attack in the sweeps. Under these conditions, a portion of the airfoil stalled when the maximum angles of attack were obtained, and the maximum lift coefficients occurred just prior to most of the upper surface flow separating. The reflex area of the lower surface trailing edge can easily be selected from the data because of a characteristic change in the magnitude of the pressure coefficient in this area. Also note the "odd" pressure fluctuation near the lower surface reflex area. This anomaly "moves" with the angle of attack. Figure 38 shows the LEGR case for the same test conditions as the previous figure. The pressure peaks were not as high as for the clean case; however, the stall behavior was the same. In addition, the pressure disturbance apparent near the lower surface reflex for the clean case was not evident in this case. This could suggest that the pressure disturbance was a boundary layer phenomenon because the LEGR tripped the laminar boundary layer to turbulent near the leading edge and the turbulent boundary layer was different enough to "mask" the anomaly at the trailing edge.

Figure 36 shows the smaller mean angle for the clean case at the same conditions indicated above. The structure is similar to the previous, although less of the upper surface flow separated because the maximum angle of attack was lower for this case. Again, the lower surface showed some pressure anomaly near the beginning of the reflex in the model contour. This disturbance could be observed in most of the clean unsteady wind tunnel data; however, it was less apparent at higher mean angles of attack. The application of LEGR tended to dissipate this pressure anomaly.

16
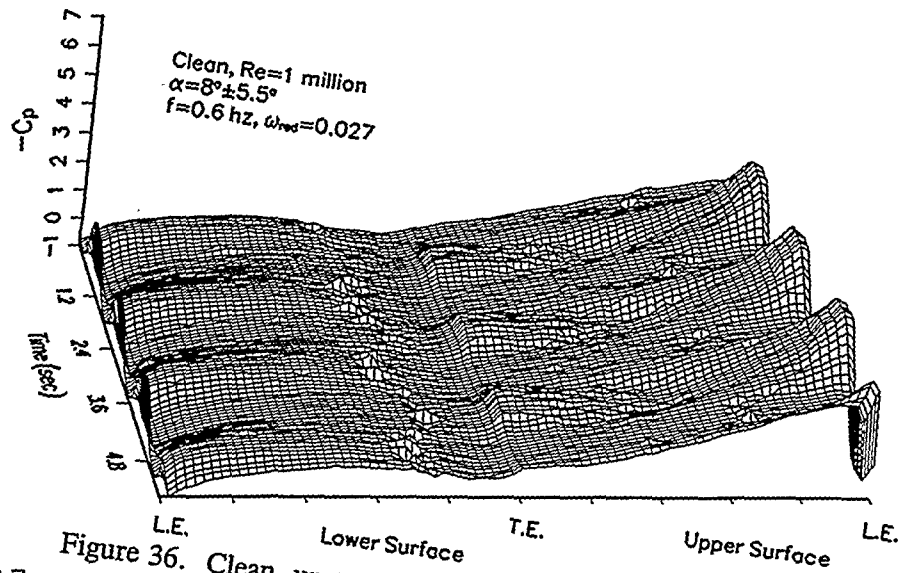
Figure 36. Clean, unsteady pressure distribution, ±5.5°
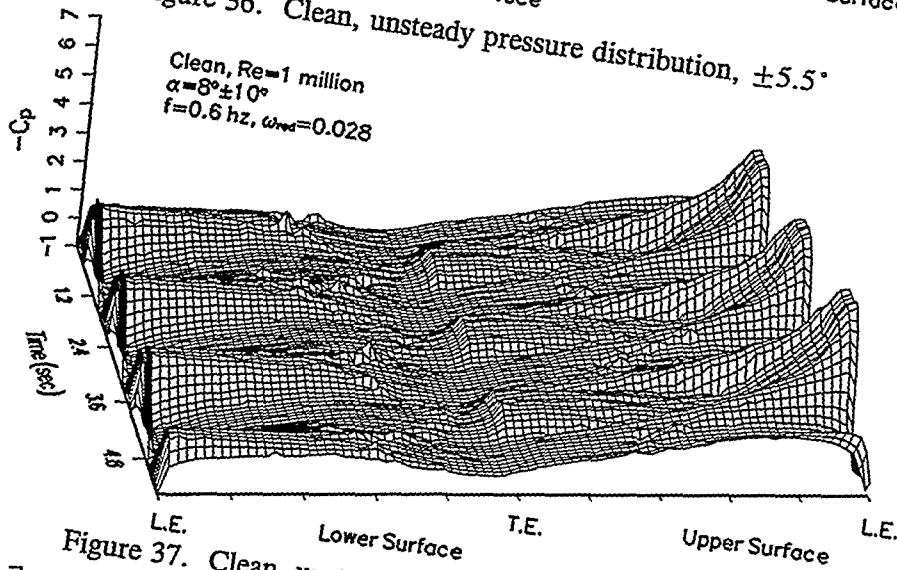
Figure 37. Clean, unsteady pressure distribution, ±10°
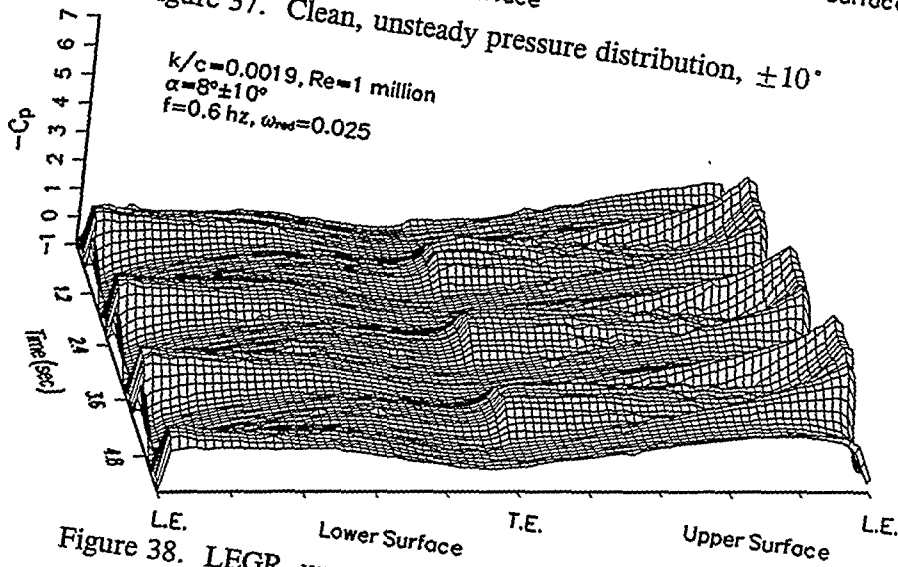
Figure 38. LEGR, unsteady pressure distribution, ±10°

17

Summary of Results

The LS(1)-0421MOD airfoil was tested under steady and unsteady wind tunnel conditions. Baseline tests were made while the model was clean and corresponding tests were conducted after LEGR was applied.

A summary of the steady state aerodynamic parameters is shown in Table 1. As observed, the application of LEGR reduced the maximum lift of the airfoil by up to 27% and the minimum drag coefficient nearly doubled. The zero-lift pitching moment coefficient also is affected by the application of LEGR reducing the magnitude by an average of 25%.

Table 1. LS(1)-0421MOD Aerodynamic Parameters Summary, Steady State

Grit Pattern	Re	C_{lmax}	C_{dmin}	C_{mo}
Clean	0.75×10^6	1.26 @ 11.6°	0.0099	-0.075
k/c=0.0019	0.75×10^6	0.98 @ 11.6°	0.0176	-0.057
Clean	1.0×10^6	1.24 @ 10.7°	0.0086	-0.078
k/c=0.0019	1.0×10^6	0.98 @ 10.6°	0.0163	-0.057
Clean	1.25×10^6	1.27 @ 12.7°	0.0096	-0.077
k/c=0.0019	1.25×10^6	0.93 @ 12.6°	0.0171	-0.058

The unsteady wind tunnel data can be divided into two groups, the $\pm 5°$ amplitude and $\pm 10°$ amplitude angle of attack oscillations, which show similar trends. For both $\pm 5°$ and $\pm 10°$, the unsteady test conditions and the maximum lift coefficients are shown in Tables 2, 3, 4, and 5. Looking at the reduced frequency, which takes oscillation and tunnel speed into account, and comparing data as this value is increased, it is apparent that the maximum lift coefficient increases. In addition, the hysteresis behavior becomes increasingly apparent with increased reduced frequency.

Table 2. Parameter Summary, Clean, $\pm 5.5°$

ω_{red}	Re x10^{-6}	f	C_{lmax}	α_{Clmax}	C_{ldec}	C_m	C_{mdec}
0.036	0.78	0.61	1.54	18.5	1.45	-0.0945	-0.0835
0.070	0.78	1.19	1.60	16.0	1.21	-0.0876	-0.0421
0.108	0.78	1.85	1.78	16.4	1.19	-0.1130	-0.0494
0.027	1.02	0.61	1.44	13.8	1.17	-0.0709	-0.0375
0.054	1.01	1.19	1.55	13.8	1.09	-0.0902	-0.0254
0.082	1.01	1.81	1.66	14.9	1.20	-0.0884	-0.0400
0.022	1.27	0.61	1.42	14.3	1.18	-0.0613	-0.0506
0.043	1.26	1.21	1.47	13.0	1.19	-0.0696	-0.0504
0.065	1.27	1.83	1.54	14.1	1.11	-0.0873	-0.0459
0.018	1.51	0.60	1.40	13.4	1.15	-0.0732	-0.0580
0.037	1.51	1.22	1.43	13.3	1.14	-0.0790	-0.0576
0.055	1.52	1.85	1.51	13.8	1.07	-0.0873	-0.0316

Table 3. Parameter Summary, LEGR, ±5.5°

ω_{red}	Re x10^{-6}	f	C_{lmax}	α_{Clmax}	C_{ldec}	C_m	C_{mdec}
0.037	0.75	0.61	1.26	13.2	0.92	-0.1234	-0.0605
0.073	0.75	1.22	1.32	12.7	0.76	-0.1076	-0.0494
0.110	0.75	1.83	1.53	14.9	0.67	-0.1433	-0.0424
0.027	1.00	0.61	1.13	12.7	0.93	-0.0967	-0.0661
0.054	1.00	1.21	1.32	13.7	0.80	-0.1246	-0.0607
0.083	1.00	1.85	1.40	14.3	0.68	-0.1503	-0.0455
0.022	1.26	0.61	1.13	11.7	0.98	-0.0881	-0.0761
0.044	1.26	1.22	1.22	12.6	0.81	-0.1159	-0.0436
0.066	1.26	1.85	1.32	12.7	0.79	-0.1057	-0.0528
0.018	1.50	0.60	1.12	11.7	0.92	-0.0836	-0.0771
0.035	1.50	1.19	1.17	13.3	0.91	-0.1166	-0.0704
0.054	1.50	1.83	1.18	12.7	0.82	-0.0944	-0.0501

As expected, the application of LEGR reduces the aerodynamic performance of the airfoil. The maximum lift coefficient is reduced by an average of 20% for all reduced frequencies. In addition to following the same trends as the clean unsteady data discussed previously, the LEGR causes the hysteresis behavior to persist into lower angles of attack than does the clean cases. Overall, the unsteady wind tunnel data shows hysteresis behavior that becomes more apparent with increased reduced frequency. The maximum unsteady lift coefficient can be from 10% to 50% higher than the steady state maximum lift coefficient. Variation in the quarter chord pitching moment coefficient can be two times greater than steady state values. These findings indicate the importance of considering the unsteady loading that occurs in wind turbine operation because steady state results can greatly underestimate the loads.

Table 4. Parameter Summary, Clean, ±10°

ω_{red}	Re x10^{-6}	f	C_{lmax}	α_{Clmax}	C_{ldec}	C_m	C_{mdec}
0.036	0.78	0.61	1.60	15.6	1.13	-0.0967	-0.0311
0.072	0.78	1.19	2.07	15.9	1.18	-0.1315	-0.0392
0.110	0.78	1.85	2.16	19.8	1.18	-0.1585	-0.0646
0.029	1.00	0.61	1.59	14.0	1.20	-0.0865	-0.0435
0.055	1.00	1.19	1.75	16.1	1.16	-0.0947	-0.0554
0.085	0.99	1.81	1.94	17.7	1.21	-0.1239	-0.0501
0.022	1.26	0.60	1.49	12.8	1.11	-0.0757	-0.0324
0.045	1.24	1.19	1.73	15.6	1.05	-0.1053	-0.0345
0.068	1.25	1.85	1.84	15.7	0.94	-0.0999	-0.0268
0.018	1.51	0.60	1.48	14.4	1.20	-0.0757	-0.0524
0.037	1.50	1.19	1.64	15.6	1.05	-0.0898	-0.0443
0.057	1.49	1.85	1.76	16.3	0.99	-0.0990	-0.0375

Table 5. Parameter Summary, LEGR, ±10°

ω_{red}	Re x10^{-6}	f	C_{lmax}	α_{Clmax}	C_{ldec}	C_m	C_{mdec}
0.033	0.77	0.60	1.34	14.6	0.78	-0.1328	-0.0621
0.067	0.77	1.19	1.50	16.3	0.62	-0.1697	-0.0566
0.103	0.77	1.83	1.75	18.8	0.72	-0.2268	-0.0968
0.026	1.01	0.60	1.23	13.5	0.75	-0.1042	-0.0503
0.051	1.00	1.19	1.51	14.7	0.69	-0.1539	-0.0437
0.079	1.00	1.85	1.65	17.8	0.66	-0.2123	-0.0757
0.021	1.25	0.61	1.19	12.6	0.82	-0.0942	-0.0629
0.040	1.24	1.18	1.32	12.2	0.70	-0.0940	-0.0304
0.063	1.24	1.83	1.54	15.7	0.67	-0.1561	-0.0531
0.019	1.50	0.60	1.16	11.9	0.74	-0.0853	-0.0335
0.038	1.49	1.19	1.30	13.1	0.67	-0.1008	-0.0370
0.058	1.49	1.83	1.51	14.2	0.58	-0.1263	-0.0409

References

Pope, A.; Harper, J.J. (1966). *Low Speed Wind Tunnel Testing*. New York, NY: John Wiley & Sons, Inc.

Schlichting, H. (1979). *Boundary Layer Theory*. New York, NY: McGraw-Hill Inc.

Appendix A: Model and Surface Pressure Tap Coordinates

Table A1. LS(1)-0421MOD Measured Model Coordinates 18-inch desired chord			
Chord Station (in)	Upper Ordinate (in)	Chord Station (in)	Lower Ordinate (in)
0.000	0.042	0.000	-0.003
0.003	0.081	0.001	-0.024
0.008	0.130	0.003	-0.056
0.018	0.186	0.006	-0.082
0.034	0.257	0.011	-0.116
0.049	0.312	0.018	-0.148
0.077	0.395	0.019	-0.153
0.091	0.429	0.030	-0.188
0.107	0.465	0.042	-0.221
0.134	0.523	0.055	-0.251
0.178	0.601	0.071	-0.282
0.212	0.656	0.093	-0.318
0.283	0.758	0.135	-0.376
0.320	0.804	0.168	-0.415
0.355	0.848	0.224	-0.472
0.429	0.931	0.277	-0.518
0.477	0.980	0.387	-0.596
0.511	1.012	0.482	-0.651
0.606	1.098	0.529	-0.676
0.657	1.139	0.639	-0.728
0.702	1.174	0.752	-0.775
0.825	1.260	0.801	-0.795
0.883	1.297	1.122	-0.908
0.907	1.311	1.173	-0.924
1.039	1.386	1.328	-0.971
1.125	1.431	1.457	-1.007
1.192	1.464	1.588	-1.041
1.340	1.533	1.714	-1.072

Table A1. LS(1)-0421MOD Measured Model Coordinates 18-inch desired chord				
Chord Station (in)	Upper Ordinate (in)		Chord Station (in)	Lower Ordinate (in)
1.430	1.571		1.828	-1.098
1.535	1.613		1.913	-1.116
1.727	1.683		1.966	-1.127
1.955	1.757		2.109	-1.156
2.244	1.840		2.281	-1.189
2.541	1.914		2.474	-1.223
2.657	1.941		2.919	-1.292
2.944	2.001		3.278	-1.339
3.236	2.054		3.471	-1.362
3.415	2.082		3.621	-1.379
3.522	2.098		4.021	-1.418
3.881	2.143		4.393	-1.447
4.013	2.157		4.818	-1.473
4.203	2.176		5.748	-1.512
4.360	2.189		6.307	-1.520
4.699	2.212		6.844	-1.520
4.928	2.224		7.093	-1.517
5.165	2.233		7.276	-1.513
5.597	2.240		7.507	-1.508
5.833	2.240		7.926	-1.493
6.096	2.236		8.345	-1.471
6.525	2.222		8.937	-1.428
6.734	2.213		9.364	-1.388
6.973	2.199		9.564	-1.361
7.415	2.168		9.825	-1.334
7.669	2.146		10.072	-1.302
7.900	2.123		10.666	-1.215
8.331	2.075		11.104	-1.141
8.548	2.048		11.322	-1.101

Table A1. LS(1)-0421MOD Measured Model Coordinates 18-inch desired chord				
Chord Station (in)	Upper Ordinate (in)		Chord Station (in)	Lower Ordinate (in)
8.768	2.019		11.694	-1.030
9.170	1.962		12.080	-0.953
9.411	1.925		12.482	-0.869
9.641	1.889		12.632	-0.837
10.102	1.812		13.016	-0.754
10.343	1.769		13.268	-0.699
10.628	1.716		13.556	-0.636
10.979	1.647		13.670	-0.611
11.126	1.617		13.753	-0.593
11.311	1.580		14.132	-0.512
11.864	1.463		14.285	-0.480
12.164	1.396		14.433	-0.449
12.611	1.295		14.531	-0.429
12.815	1.247		14.617	-0.411
13.097	1.180		14.716	-0.391
13.643	1.047		14.860	-0.363
13.884	0.988		15.000	-0.336
14.086	0.937		15.186	-0.301
14.521	0.827		15.332	-0.275
14.732	0.773		15.496	-0.247
14.934	0.721		15.654	-0.223
15.315	0.625		15.789	-0.204
15.430	0.596		15.861	-0.195
15.598	0.553		16.013	-0.177
15.882	0.480		16.069	-0.171
16.035	0.441		16.167	-0.162
16.260	0.381		16.234	-0.156
16.616	0.286		16.388	-0.145
16.754	0.247		16.533	-0.137

Table A1. LS(1)-0421MOD Measured Model Coordinates 18-inch desired chord				
Chord Station (in)	Upper Ordinate (in)		Chord Station (in)	Lower Ordinate (in)
16.959	0.185		16.597	-0.134
17.338	0.069		16.636	-0.133
17.497	0.022		16.729	-0.130
17.642	-0.019		16.817	-0.129
17.755	-0.049		16.890	-0.127
17.877	-0.079		17.033	-0.128
17.937	-0.096		17.065	-0.128
18.004	-0.125		17.197	-0.132
18.017	-0.136		17.252	-0.134
			17.365	-0.140
			17.579	-0.155
			17.625	-0.159
			17.693	-0.165
			17.887	-0.181
			17.954	-0.183
			18.015	-0.162
End of Table A1				

Table A2. LS(1)-0421MOD Surface Pressure Taps Non-Dimensional Coordinates		
Tap Number	Chord Station	Ordinate
1	1.0021	-0.0088
2	0.9833	-0.0097
3	0.9677	-0.0084
4	0.9451	-0.0076
5	0.9206	-0.0080
6	0.8905	-0.0102 -
7	0.8687	-0.0130
8	0.8404	-0.0178
9	0.8177	-0.0221
10	0.7900	-0.0279
11	0.7415	-0.0383
12	0.6915	-0.0490
13	0.6437	-0.0586
14	0.5946	-0.0673
15	0.5446	-0.0744
16	0.4946	-0.0795
17	0.3937	-0.0841
18	0.2936	-0.0828
19	0.2444	-0.0800
20	0.2198	-0.0781
21	0.1968	-0.0757
22	0.1710	-0.0725
23	0.1439	-0.0685
24	0.1197	-0.0642
25	0.0976	-0.0595
26	0.0714	-0.0526
27	0.0449	-0.0436
28	0.0196	-0.0309
29	0.0001	0.0104

Table A2. LS(1)-0421MOD Surface Pressure Taps Non-Dimensional Coordinates		
Tap Number	Chord Station	Ordinate
30	0.0163	0.0423
31	0.0292	0.0567
32	0.0510	0.0730
33	0.0744	0.0851
34	0.1001	0.0949
35	0.1258	0.1025
36	0.1499	0.1084
37	0.1754	0.1134
38	0.1997	0.1172
39	0.2254	0.1201
40	0.2508	0.1223
41	0.2993	0.1244
42	0.3501	0.1239
43	0.3996	0.1213
44	0.4515	0.1165
45	0.4987	0.1104
46	0.5492	0.1025
47	0.6016	0.0930
48	0.6235	0.0885
49	0.6988	0.0720
50	0.7473	0.0604
51	0.7964	0.0481
52	0.8228	0.0413
53	0.8518	0.0340
54	0.8744	0.0282
55	0.8958	0.0226
56	0.9236	0.0151
57	0.9467	0.0082
58	0.9697	0.0012

Table A2. LS(1)-0421MOD Surface Pressure Taps Non-Dimensional Coordinates		
Tap Number	Chord Station	Ordinate
59	0.9838	-0.0024
60	0.9935	-0.0049
End of Table A2		

Appendix B: Steady-State Data

Integrated Coefficients and Pressure Distributions

List of Tables

Page

List of Figures   Page

Table B1. LS(1)-0421MOD, Clean, Re = 0.75×10^6						
Run	AOA	C_l	C_{dp}	$C_{m¼}$	Re x 10^{-6}	C_{dw}
200	-10.7	-0.53	-0.0065	-0.0675	0.76	0.0344
201	-8.7	-0.43	-0.0114	-0.0625	0.76	0.0225
202	-6.6	-0.29	-0.0134	-0.0609	0.75	0.0220
203	-4.6	-0.09	-0.0114	-0.0674	0.75	0.0105
204	-2.6	0.14	-0.0076	-0.0710	0.75	0.0118
205	-0.5	0.38	-0.0033	-0.0760	0.75	0.0099
206	1.5	0.61	0.0033	-0.0791	0.75	0.0120
207	3.6	0.82	0.0113	-0.0768	0.76	0.0114
208	5.6	1.01	0.0161	-0.0743	0.75	0.0145
209	7.6	1.15	0.0297	-0.0679	0.75	0.0170
210	9.7	1.23	0.0438	-0.0566	0.76	0.0293
211	10.7	1.25	0.0497	-0.0545	0.75	0.0391
212	11.6	1.26	0.0571	-0.0550	0.75	--
213	12.6	1.22	0.0612	-0.0534	0.76	--
214	13.7	1.18	0.0693	-0.0532	0.76	--
215	14.6	1.18	0.0837	-0.0558	0.76	--
216	15.7	1.16	0.0974	-0.0593	0.77	--
217	16.7	1.15	0.1125	-0.0644	0.76	--
218	17.7	1.13	0.1304	-0.0708	0.75	--
219	18.7	1.12	0.1518	-0.0784	0.76	--
220	19.7	1.13	0.1757	-0.0885	0.77	--
221	21.7	1.26	0.2275	-0.1026	0.77	--
222	23.6	1.27	0.2791	-0.1198	0.77	--
223	25.7	1.25	0.3254	-0.1352	0.78	--
224	27.6	1.19	0.3858	-0.1547	0.77	--
225	29.5	1.05	0.6505	-0.2185	0.81	--
226	31.5	1.08	0.7194	-0.2367	0.80	--

Table B1. LS(1)-0421MOD, Clean, Re = 0.75×10^6						
Run	AOA	C_l	C_{dp}	$C_{m\frac{1}{4}}$	Re x 10^{-6}	C_{dw}
227	33.5	1.09	0.7712	-0.2529	0.81	--
228	35.4	1.16	0.8789	-0.2769	0.81	--
229	37.5	1.16	0.9480	-0.2893	0.84	--
230	39.4	1.18	1.0315	-0.3071	0.84	--
End of Table B1						

Table B2. LS(1)-0421MOD, Clean, Re = 1.00 x 10^6						
Run	AOA	C_l	C_{dp}	$C_{m\frac{1}{4}}$	Re x 10^{-6}	C_{dw}
163	-10.7	-0.55	-0.0115	-0.0670	0.98	0.0321
164	-8.7	-0.43	-0.0109	-0.0615	1.01	0.0214
165	-6.6	-0.29	-0.0126	-0.0606	0.99	0.0180
166	-4.6	-0.09	-0.0112	-0.0666	1.01	0.0144
167	-2.6	0.14	-0.0082	-0.0723	0.99	0.0086
168	-0.5	0.39	-0.0039	-0.0782	1.00	0.0119
169	1.6	0.62	0.0021	-0.0788	1.01	0.0156
170	3.6	0.82	0.0105	-0.0795	1.01	0.0157
171	5.5	1.01	0.0141	-0.0728	1.01	0.0164
172	7.6	1.15	0.0253	-0.0661	1.02	0.0189
173	9.7	1.23	0.0372	-0.0543	1.02	0.0359
174	10.7	1.24	0.0453	-0.0531	1.01	0.0528
175	11.8	1.23	0.0554	-0.0536	1.01	--
176	12.7	1.20	0.0629	-0.0538	1.01	--
177	13.6	1.18	0.0729	-0.0560	1.01	--
178	14.6	1.15	0.0852	-0.0593	1.00	--
179	15.7	1.28	0.1376	-0.0816	1.01	--
180	16.7	1.26	0.1458	-0.0805	1.02	--
181	17.7	1.24	0.1595	-0.0809	1.02	--
182	18.7	1.23	0.1718	-0.0840	1.03	--
183	19.7	1.24	0.1918	-0.0907	1.04	--
184	21.8	1.26	0.2388	-0.1060	1.02	--
185	23.6	1.26	0.2800	-0.1191	1.03	--
186	25.7	1.30	0.3385	-0.1393	1.03	--
187	27.7	1.30	0.3854	-0.1523	1.04	--
188	29.5	1.12	0.4566	-0.1809	1.03	--
189	31.6	1.15	0.5053	-0.1929	1.06	--

Table B2. LS(1)-0421MOD, Clean, Re = 1.00×10^6						
Run	AOA	C_l	C_{dp}	$C_{m\frac{1}{4}}$	Re x 10^{-6}	C_{dw}
190	33.6	1.18	0.5687	-0.2105	1.05	—
191	35.6	1.21	0.6375	-0.2303	1.06	—
192	37.5	1.26	0.7074	-0.2516	1.08	—
193	39.5	1.37	0.8409	-0.3015	1.09	—
End of Table B2						

Table B3. LS(1)-0421MOD, Clean, Re = 1.25×10^6						
Run	AOA	C_l	C_{dp}	$C_{m\frac{1}{4}}$	Re x 10^{-6}	C_{dw}
125	-10.6	-0.55	-0.0102	-0.0648	1.26	0.0340
126	-8.7	-0.43	-0.0114	-0.0622	1.26	0.0187
127	-6.7	-0.29	-0.0126	-0.0599	1.26	0.0178
128	-4.5	-0.08	-0.0114	-0.0668	1.26	0.0136
129	-2.6	0.14	-0.0077	-0.0741	1.26	0.0096
130	-0.5	0.38	-0.0032	-0.0776	1.26	0.0099
131	1.6	0.61	0.0037	-0.0784	1.26	0.0106
132	3.6	0.82	0.0098	-0.0787	1.25	0.0123
133	5.6	0.99	0.0187	-0.0731	1.25	0.0143
134	7.7	1.13	0.0327	-0.0670	1.26	0.0198
135	9.6	1.22	0.0381	-0.0550	1.26	0.0318
136	10.7	1.24	0.0463	-0.0534	1.26	0.0586
137	11.6	1.25	0.0640	-0.0620	1.26	--
138	12.7	1.27	0.0821	-0.0678	1.27	--
139	13.7	1.26	0.0962	-0.0676	1.27	--
140	14.7	1.22	0.0969	-0.0626	1.26	--
141	15.7	1.22	0.1145	-0.0670	1.27	--
142	16.7	1.21	0.1301	-0.0702	1.27	--
143	17.7	1.21	0.1464	-0.0748	1.27	--
144	18.6	1.09	0.1686	-0.0884	1.28	--
145	19.7	1.19	0.1792	-0.0856	1.29	--
146	21.7	1.23	0.2380	-0.1049	1.29	--
147	23.6	1.26	0.2934	-0.1258	1.29	--
148	25.6	1.30	0.3537	-0.1443	1.29	--
149	27.6	1.31	0.3959	-0.1544	1.30	--
150	29.6	1.32	0.4364	-0.1653	1.32	--
151	31.5	1.17	0.5023	-0.1894	1.32	--

Table B3. LS(1)-0421MOD, Clean, Re = 1.25×10^6						
Run	AOA	C_l	C_{dp}	$C_{m\frac{1}{4}}$	Re x 10^{-6}	C_{dw}
152	33.6	1.19	0.5639	-0.2042	1.32	--
153	35.6	1.20	0.6302	-0.2222	1.33	--
154	37.6	1.23	0.6982	-0.2431	1.34	--
155	39.6	1.36	0.8377	-0.2950	1.36	--
End of Table B3						

Table B4. LS(1)-0421MOD, k/c = 0.0019, Re = 0.75 x 10^6						
Run	AOA	C_l	C_{dp}	$C_{m\frac{1}{4}}$	Re x 10^{-6}	C_{dw}
310	-10.6	-0.47	-0.0054	-0.0668	0.77	0.0539
311	-8.6	-0.37	-0.0103	-0.0645	0.76	0.0271
312	-6.7	-0.27	-0.0123	-0.0586	0.76	0.0236
313	-4.6	-0.10	-0.0118	-0.0558	0.76	0.0190
314	-2.6	0.08	-0.0082	-0.0564	0.76	0.0180
315	-0.5	0.29	-0.0032	-0.0569	0.75	0.0176
316	1.6	0.50	0.0037	-0.0564	0.76	0.0180
317	3.5	0.68	0.0096	-0.0533	0.76	0.0197
318	5.6	0.80	0.0214	-0.0494	0.76	0.0264
319	7.7	0.90	0.0377	-0.0461	0.76	0.0266
320	9.6	0.97	0.0610	-0.0522	0.75	0.0292
321	10.6	0.97	0.0782	-0.0566	0.76	--
322	11.6	0.98	0.0990	-0.0635	0.76	--
323	12.7	0.97	0.1168	-0.0667	0.77	--
324	13.6	0.96	0.1376	-0.0750	0.77	--
325	14.7	0.94	0.1601	-0.0806	0.76	--
326	15.5	0.91	0.1789	-0.0871	0.76	--
327	16.5	0.90	0.2055	-0.0943	0.77	--
328	17.6	0.90	0.2271	-0.1005	0.76	--
329	18.6	0.89	0.2496	-0.1045	0.78	--
330	19.6	0.87	0.2644	-0.1074	0.77	--
331	21.5	0.87	0.3208	-0.1242	0.78	--
332	23.6	0.92	0.3958	-0.1502	0.79	--
333	25.4	0.94	0.4468	-0.1626	0.79	--
334	27.5	1.03	0.5334	-0.1923	0.79	--
335	29.6	1.09	0.6134	-0.2176	0.80	--
336	31.4	1.15	0.6926	-0.2409	0.81	--

Table B4. LS(1)-0421MOD, k/c = 0.0019, Re = 0.75 x 10^6						
Run	AOA	C_l	C_{dp}	$C_{m\frac{1}{4}}$	Re x 10^{-6}	C_{dw}
337	33.5	1.21	0.7894	-0.2720	0.81	--
338	35.6	1.25	0.8814	-0.2984	0.82	--
339	37.6	1.28	0.9757	-0.3255	0.83	--
340	39.4	1.29	1.0530	-0.3443	0.84	--
End of Table B4						

Table B5. LS(1)-0421MOD, k/c = 0.0019, Re = 1.00 x 10^6						
Run	AOA	C_l	C_{dp}	$C_{m¼}$	Re x 10^{-6}	C_{dw}
273	-10.6	-0.48	-0.0051	-0.0671	1.01	0.0538
274	-8.7	-0.38	-0.0087	-0.0653	1.01	0.0305
275	-6.6	-0.28	-0.0102	-0.0589	1.01	0.0250
276	-4.5	-0.10	-0.0092	-0.0554	1.01	0.0184
277	-2.6	0.08	-0.0072	-0.0566	1.00	0.0169
278	-0.5	0.31	-0.0016	-0.0572	1.01	0.0163
279	1.6	0.52	0.0041	-0.0580	1.01	0.0185
280	3.5	0.68	0.0121	-0.0549	1.01	0.0205
281	5.6	0.82	0.0222	-0.0490	1.01	0.0273
282	7.6	0.91	0.0389	-0.0484	1.01	0.0369
283	9.7	0.98	0.0729	-0.0603	1.01	--
284	10.6	0.98	0.0868	-0.0619	1.02	--
285	11.7	0.97	0.1072	-0.0676	1.01	--
286	12.6	0.90	0.1151	-0.0678	1.02	--
287	13.6	0.91	0.1341	-0.0725	1.02	--
288	14.6	0.92	0.1656	-0.0849	1.02	--
289	15.6	0.90	0.1901	-0.0924	1.02	--
290	16.6	0.89	0.2143	-0.0992	1.03	--
291	17.6	0.88	0.2336	-0.1042	1.02	--
292	18.6	0.86	0.2521	-0.1069	1.03	--
293	19.6	0.86	0.2744	-0.1134	1.04	--
294	21.5	0.90	0.3409	-0.1367	1.04	--
295	23.5	0.93	0.4027	-0.1547	1.04	--
296	25.6	1.01	0.4859	-0.1823	1.05	--
297	27.5	1.05	0.5520	-0.2017	1.05	--
298	29.5	1.12	0.6323	-0.2267	1.07	--
299	31.5	1.17	0.7134	-0.2507	1.07	--

Table B5. LS(1)-0421MOD, $k/c = 0.0019$, Re = 1.00 x 10^6						
Run	AOA	C_l	C_{dp}	$C_{m\frac{1}{4}}$	Re x 10^{-6}	C_{dw}
300	33.6	1.22	0.7997	-0.2762	1.08	—
301	35.4	1.28	0.9052	-0.3112	1.09	—
302	37.4	1.31	0.9923	-0.3352	1.12	—
303	39.4	1.30	1.0593	-0.3452	1.12	—
End of Table B5						

Table B6. LS(1)-0421MOD, k/c = 0.0019, Re = 1.25 x 10^6						
Run	AOA	C_l	C_{dp}	$C_{m\frac{1}{4}}$	Re x 10^{-6}	C_{dw}
236	-10.6	-0.49	-0.0025	-0.0663	1.26	0.0515
237	-8.7	-0.40	-0.0087	-0.0650	1.27	0.0311
238	-6.6	-0.28	-0.0101	-0.0582	1.27	0.0235
239	-4.5	-0.10	-0.0092	-0.0562	1.26	0.0198
240	-2.6	0.08	-0.0064	-0.0568	1.26	0.0179
241	-0.5	0.31	-0.0016	-0.0583	1.26	0.0176
242	1.5	0.51	0.0048	-0.0581	1.26	0.0171
243	3.7	0.69	0.0145	-0.0553	1.26	0.0198
244	5.6	0.82	0.0229	-0.0502	1.26	0.0261
245	7.6	0.89	0.0392	-0.0464	1.26	0.0398
246	9.7	0.89	0.0594	-0.0478	1.27	--
247	10.6	0.93	0.0825	-0.0579	1.27	--
248	11.6	0.91	0.0987	-0.0615	1.28	--
249	12.6	0.93	0.1215	-0.0696	1.27	--
250	13.6	0.83	0.1314	-0.0707	1.27	--
251	14.6	0.86	0.1596	-0.0817	1.27	--
252	15.6	0.86	0.1853	-0.0905	1.27	--
253	16.6	0.88	0.2150	-0.1000	1.28	--
254	17.6	0.86	0.2338	-0.1042	1.28	--
255	18.6	0.83	0.2510	-0.1066	1.29	--
256	19.5	0.84	0.2737	-0.1136	1.29	--
257	21.5	0.90	0.3464	-0.1397	1.28	--
258	23.5	0.94	0.4113	-0.1586	1.30	--
259	25.6	0.99	0.4795	-0.1790	1.32	--
260	27.6	1.06	0.5603	-0.2044	1.34	--
261	29.5	1.11	0.6327	-0.2266	1.33	--
262	31.5	1.18	0.7207	-0.2540	1.35	--

Table B6. LS(1)-0421MOD, k/c = 0.0019, Re = 1.25 x 10^6						
Run	AOA	C_l	C_{dp}	$C_{m\frac{1}{4}}$	Re x 10^{-6}	C_{dw}
263	33.4	1.23	0.8034	-0.2798	1.35	--
264	35.6	1.27	0.8975	-0.3047	1.33	--
265	37.7	1.31	0.9991	-0.3347	1.31	--
266	39.4	1.31	1.0627	-0.3503	1.29	--
End of Table B6						

LS(1)-0421MOD

Pressure Distributions, Steady State, Re = 0.75 million
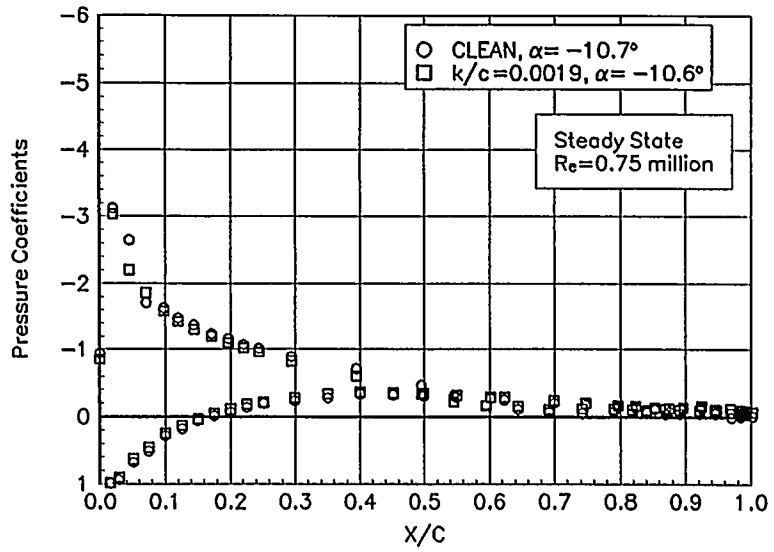
Figure B1. $\alpha = -10.7°$
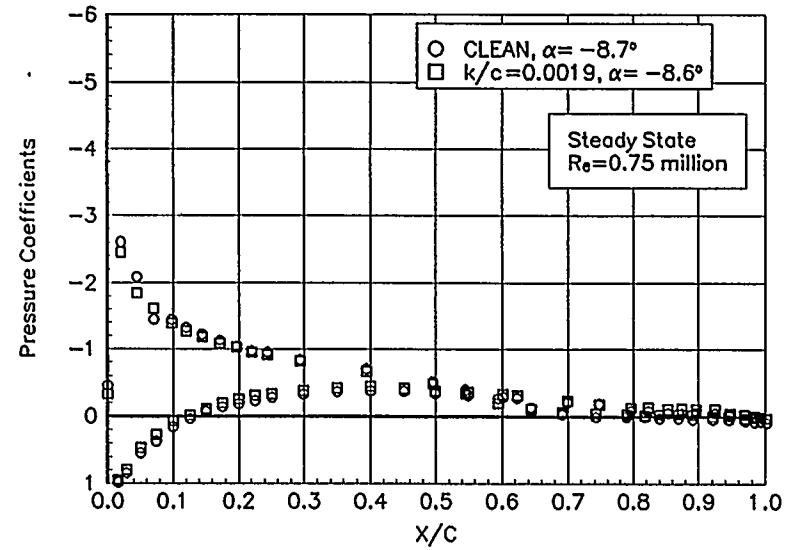
Figure B2. $\alpha = -8.7°$
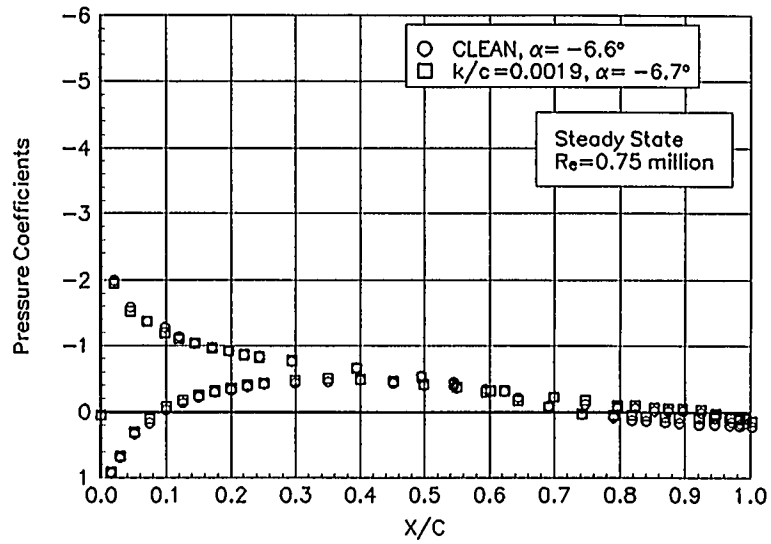
Figure B3. $\alpha = -6.6°$

Figure B4. $\alpha = -4.6°$

B-19
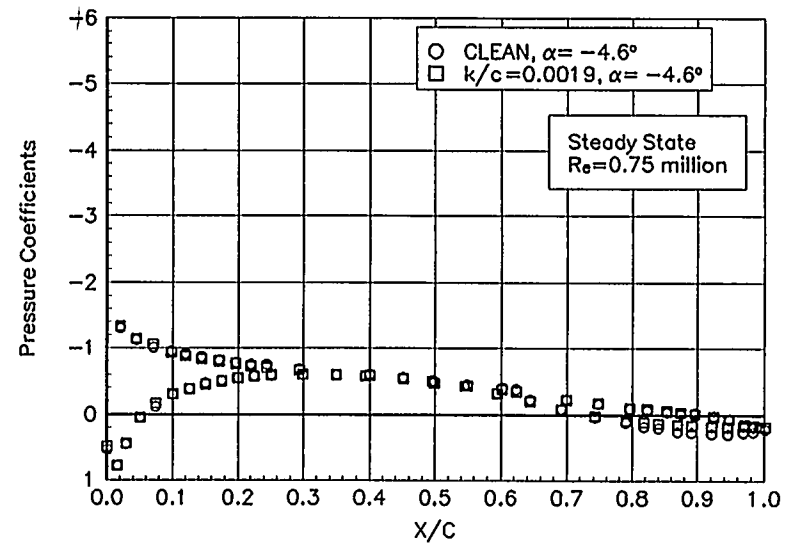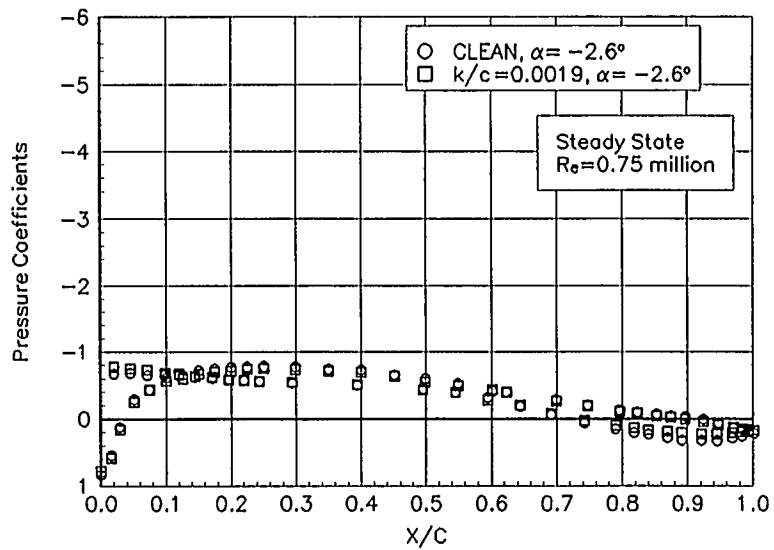
Figure B5. $\alpha = -2.6°$
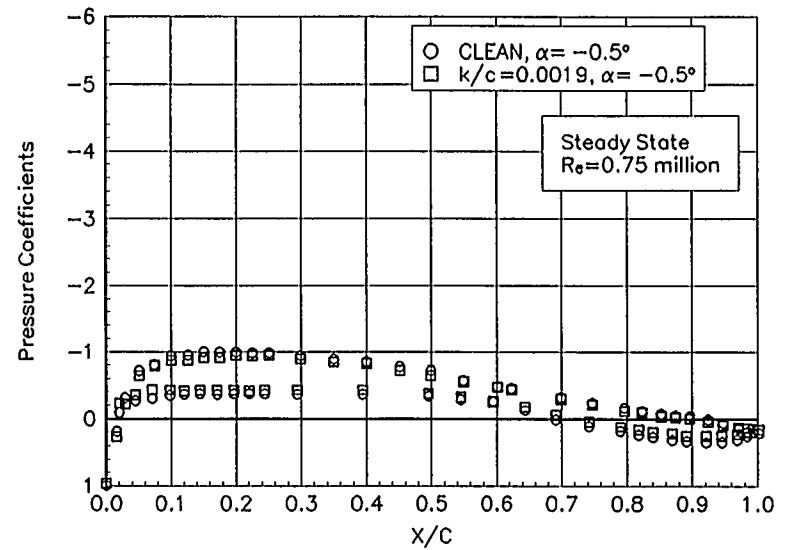
Figure B6. $\alpha = -0.5°$
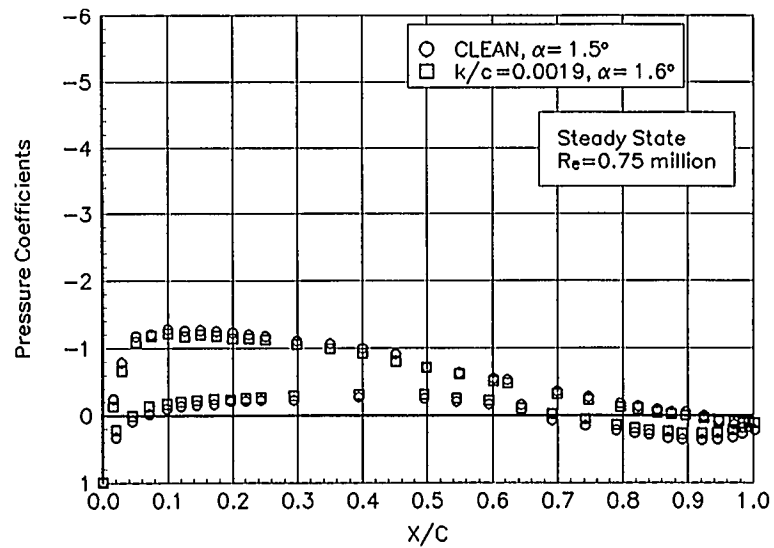
Figure B7. $\alpha = 1.5°$

Figure B8. $\alpha = 3.6°$

B-20
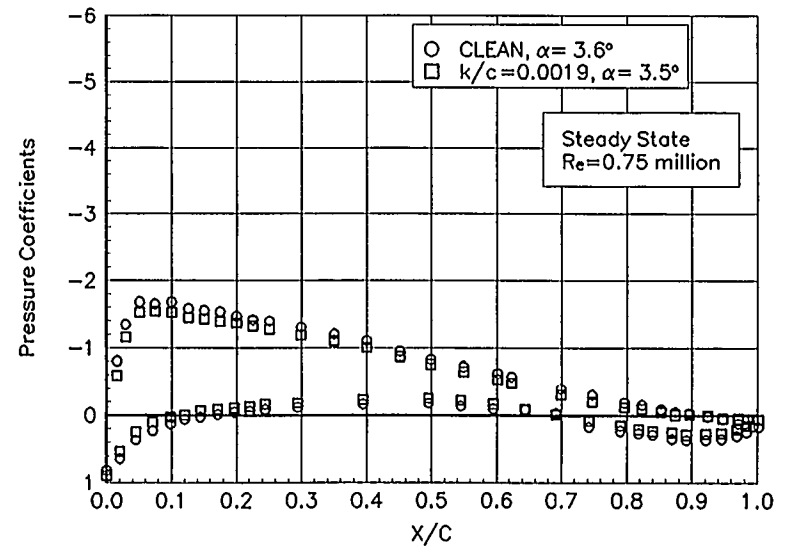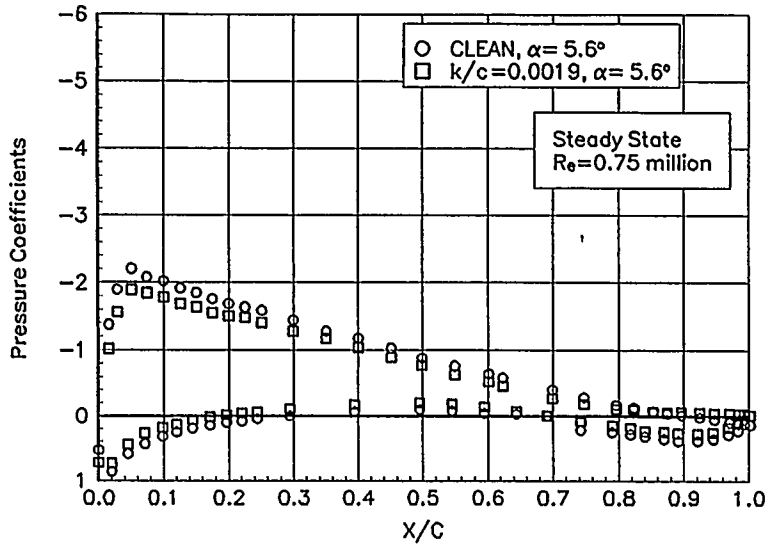
Figure B9. $\alpha = 5.6°$
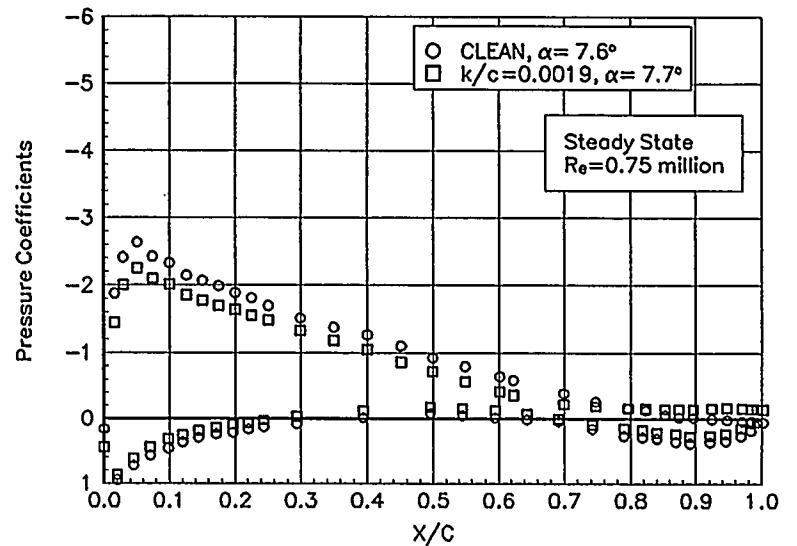
Figure B10. $\alpha = 7.6°$
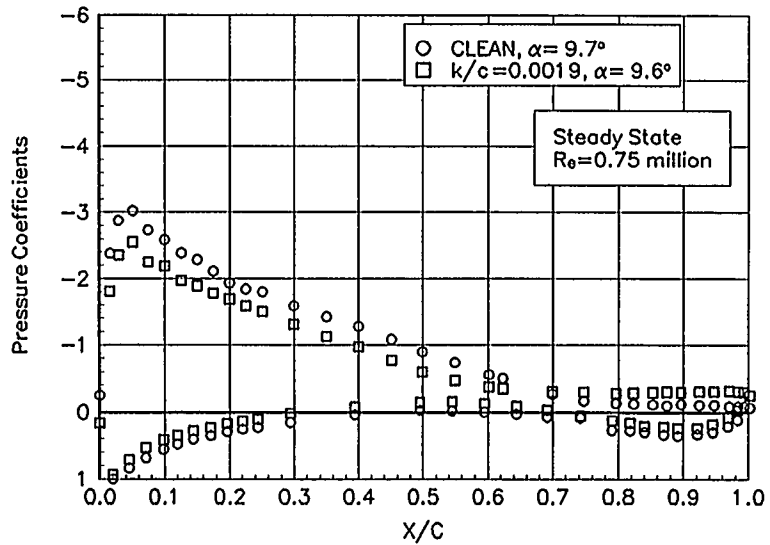
Figure B11. $\alpha = 9.7°$

Figure B12. $\alpha = 10.7°$

B-21
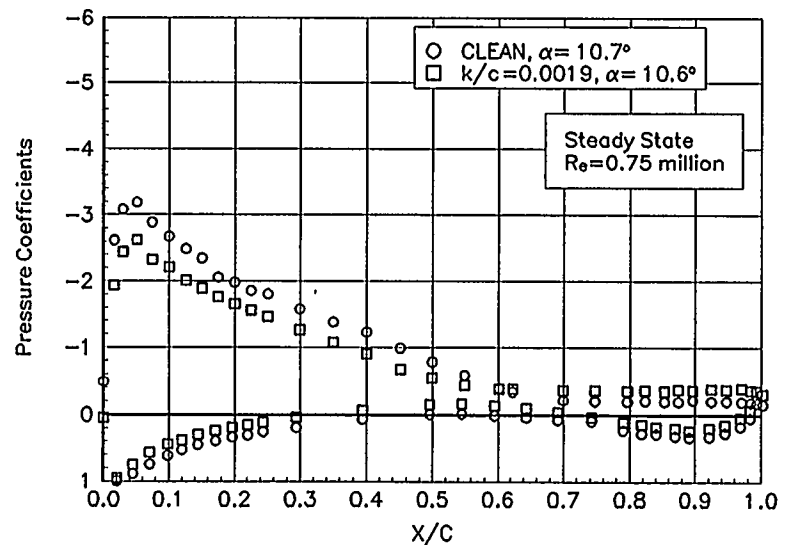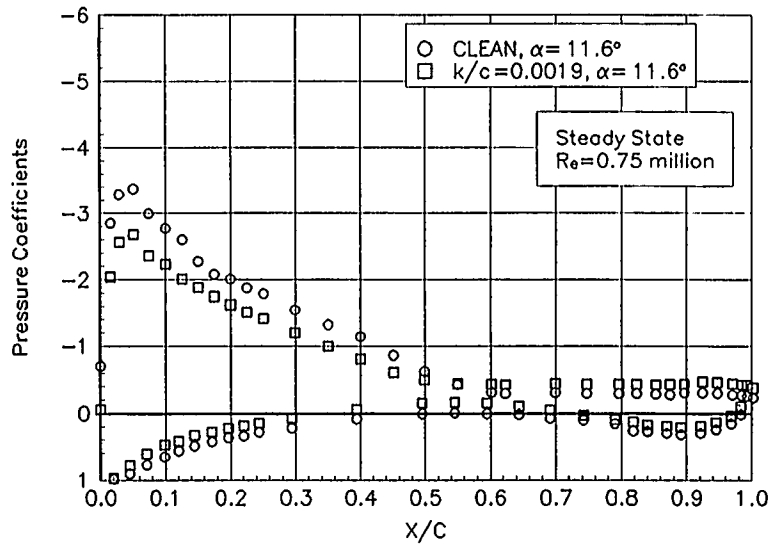
Figure B13. $\alpha = 11.6°$
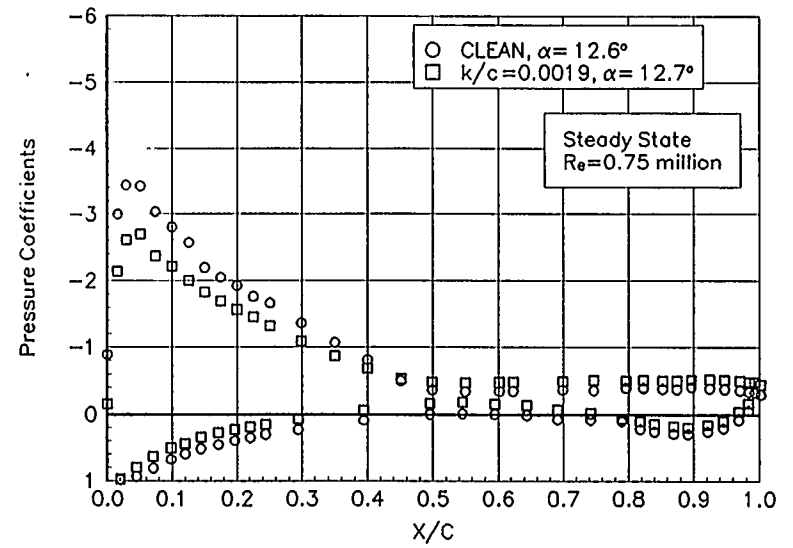
Figure B14. $\alpha = 12.6°$
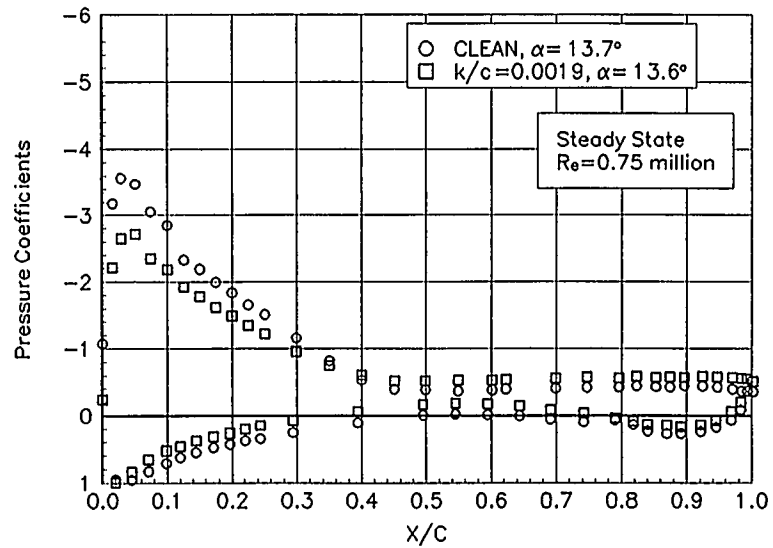
Figure B15. $\alpha = 13.7°$

Figure B16. $\alpha = 14.6°$

B-22
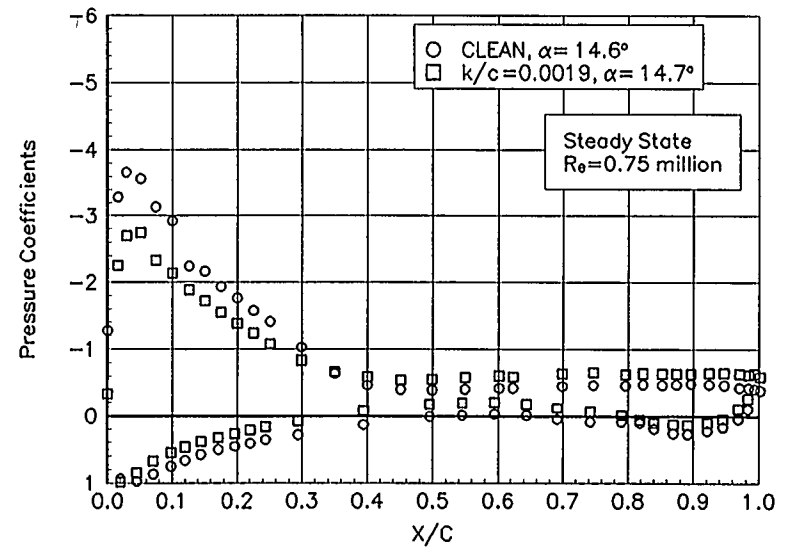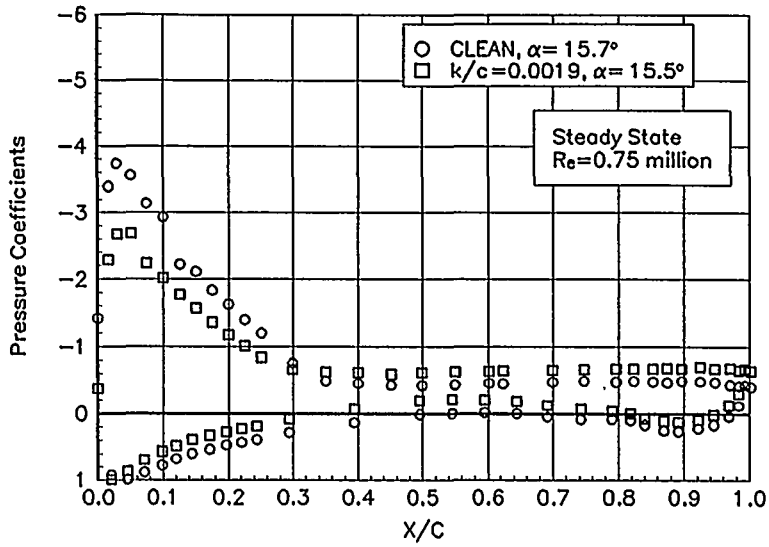
Figure B17. $\alpha = 15.7°$
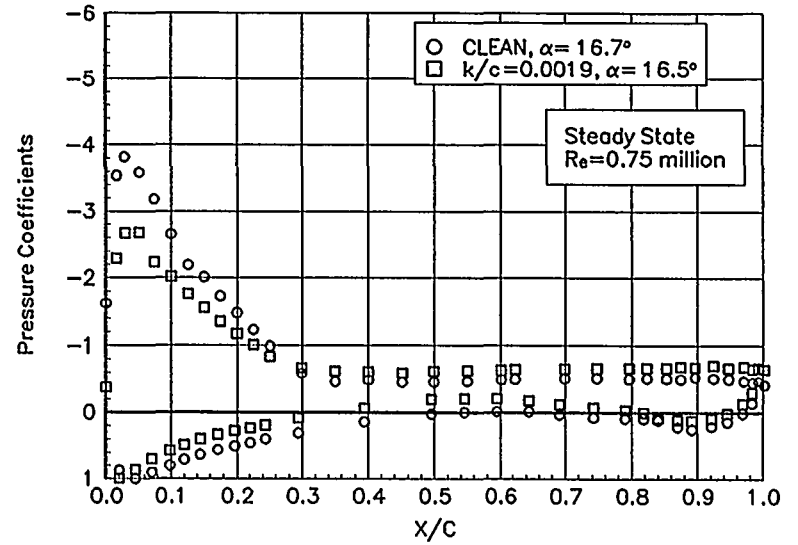
Figure B18. $\alpha = 16.7°$
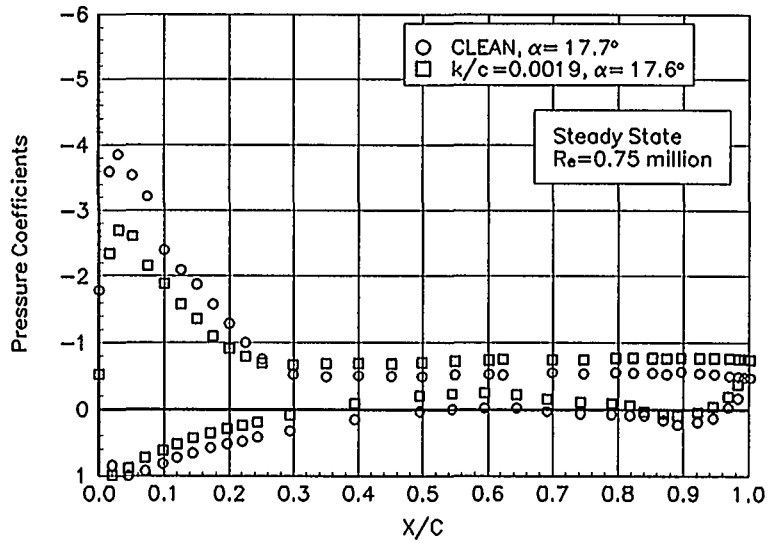
Figure B19. $\alpha = 17.7°$

Figure B20. $\alpha = 18.7°$

B-23
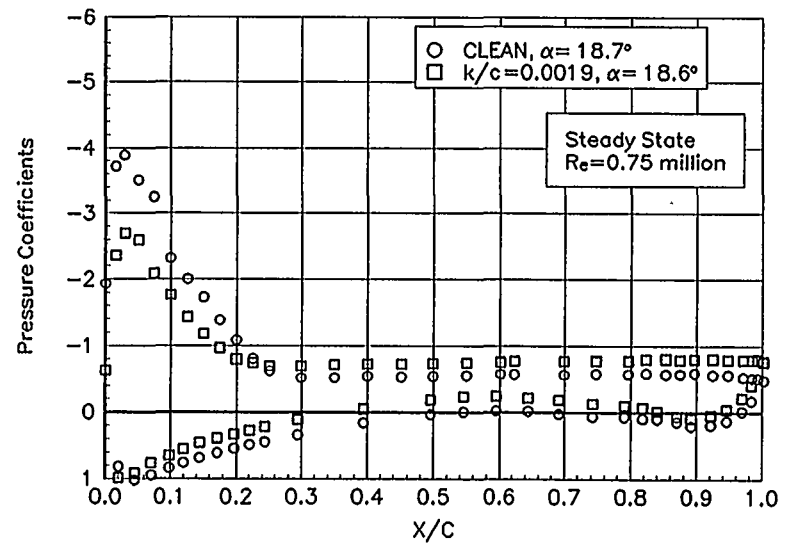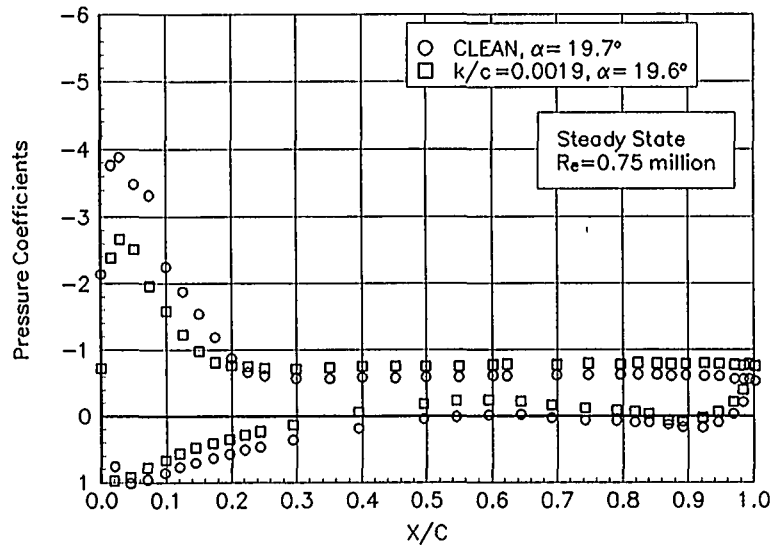
Figure B21. $\alpha = 19.7°$
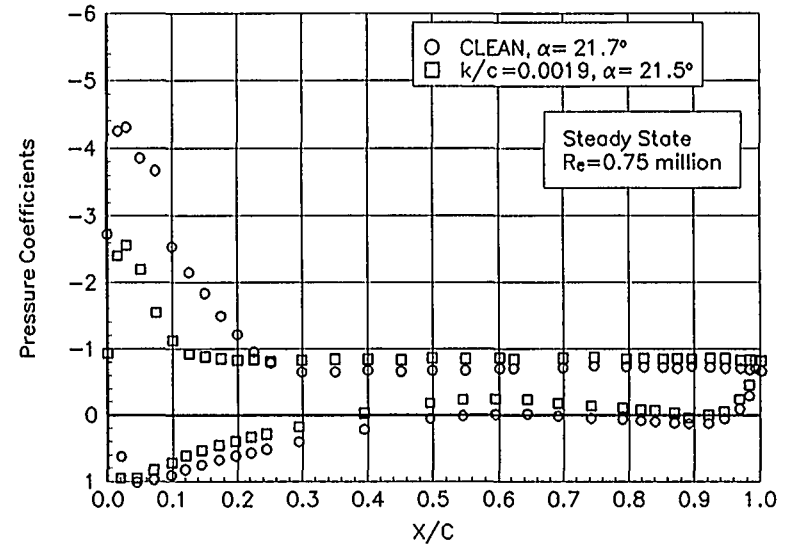
Figure B22. $\alpha = 21.7°$
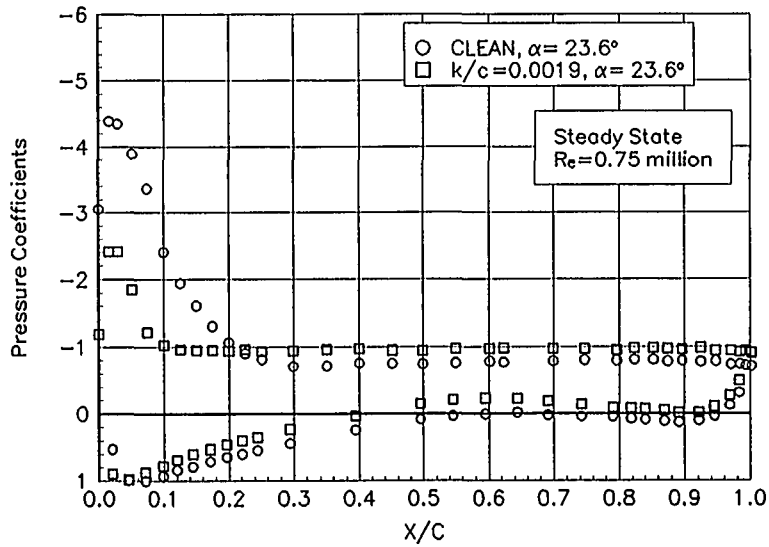
Figure B23. $\alpha = 23.6°$

Figure B24. $\alpha = 25.7°$

B-24
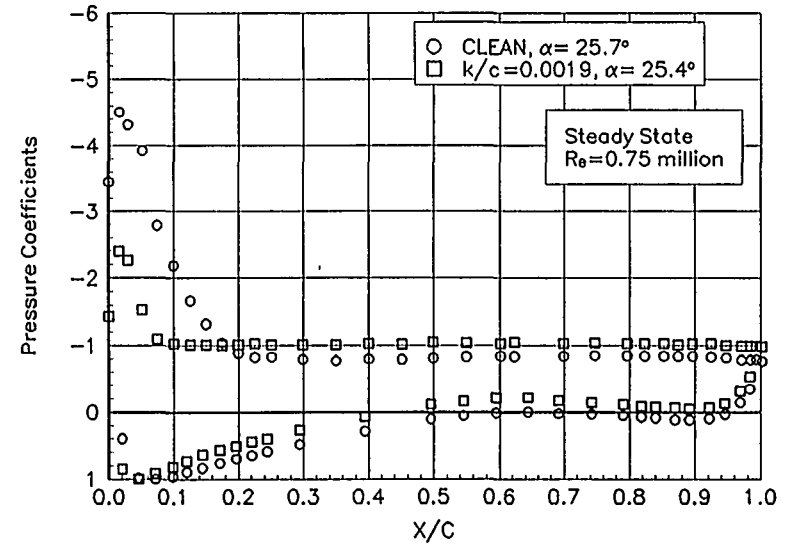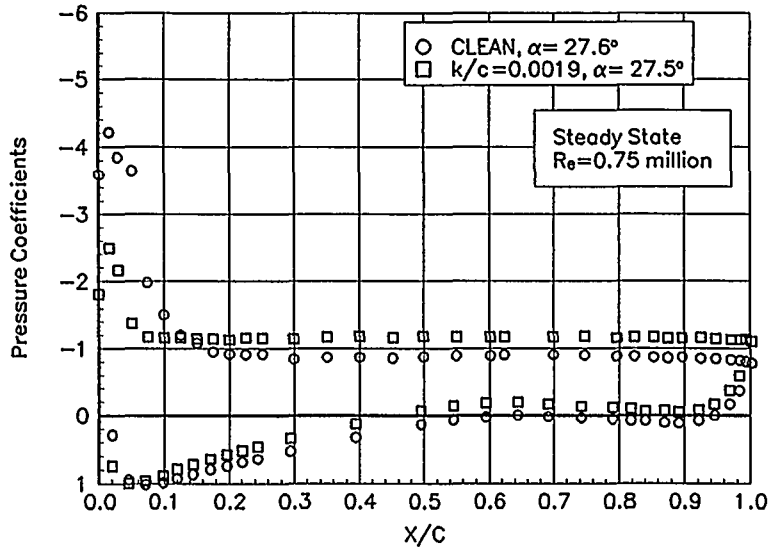
Figure B25. $\alpha = 27.6°$
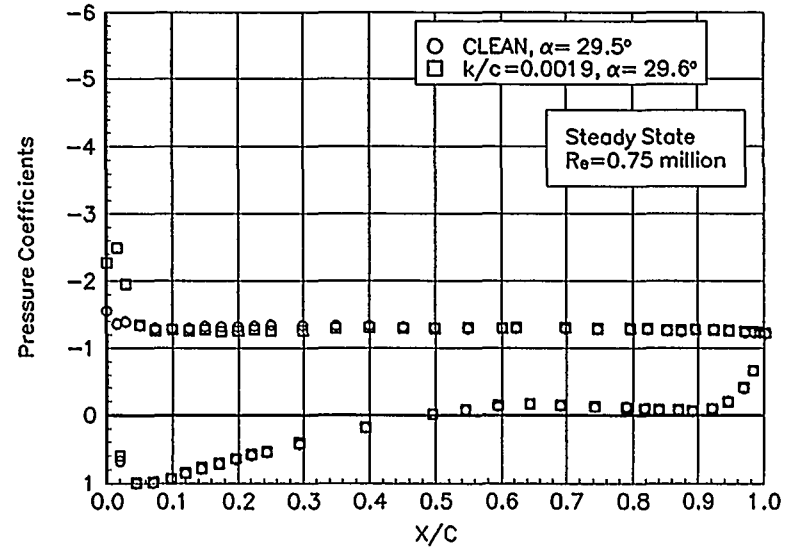
Figure B26. $\alpha = 39.5°$
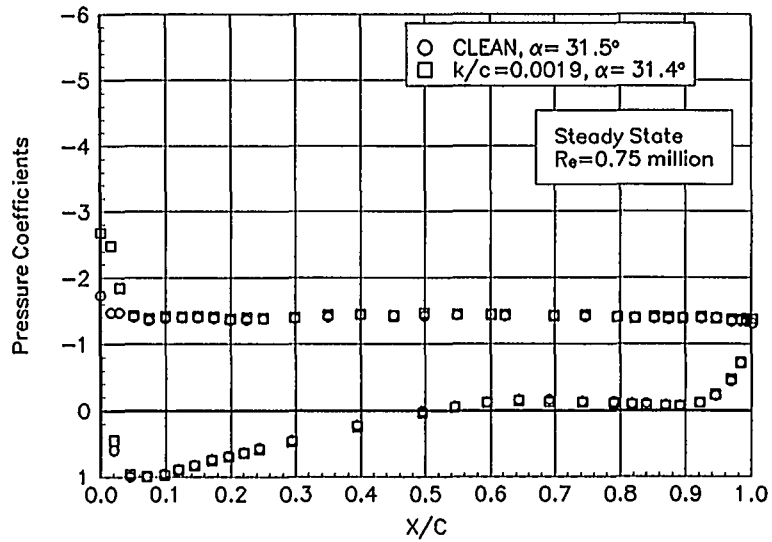
Figure B27. $\alpha = 31.5°$
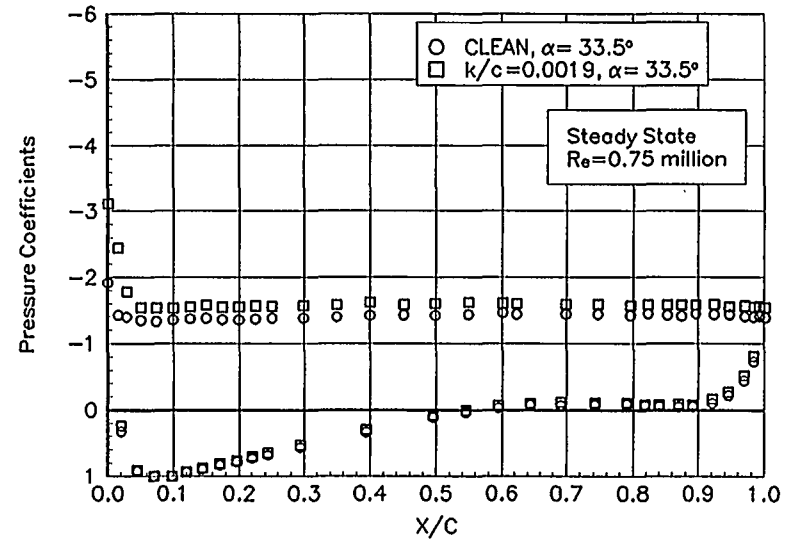
Figure B28. $\alpha = 33.5°$

B-25
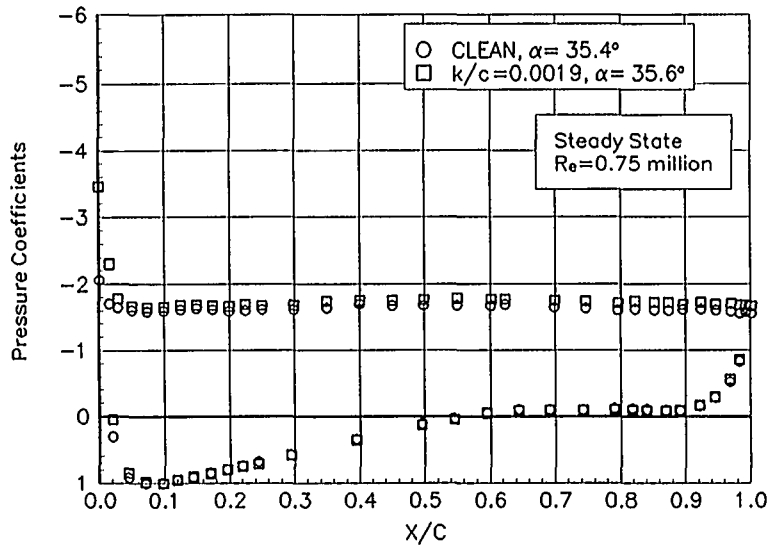
Figure B29. $\alpha = 35.4°$
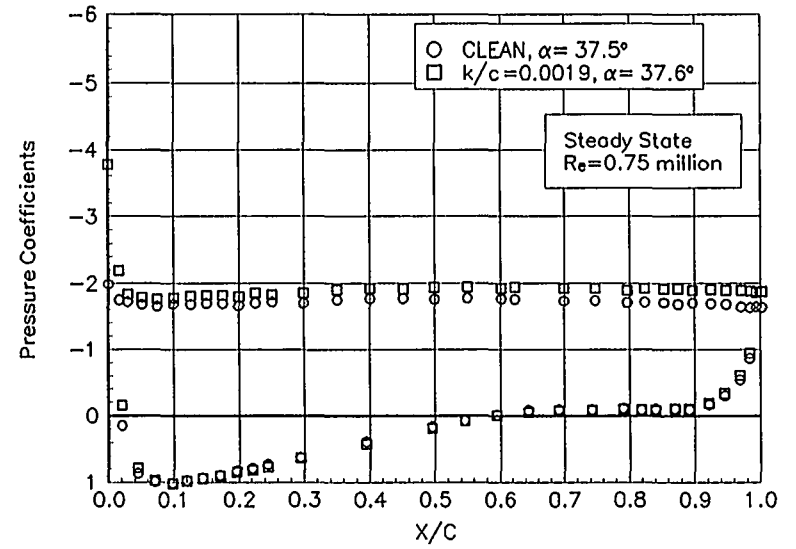
Figure B30. $\alpha = 37.5°$

Figure B31. $\alpha = 39.4°$

B-26
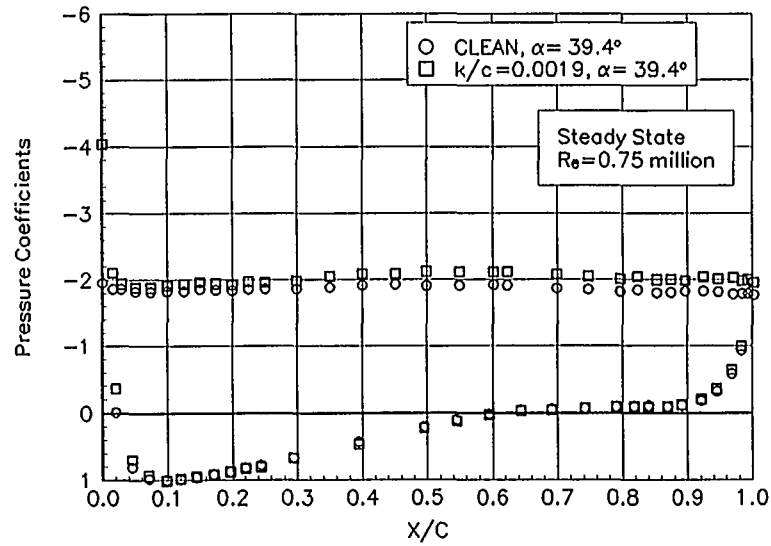
LS(1)-0421MOD

Pressure Distributions, Steady State, Re = 1 million
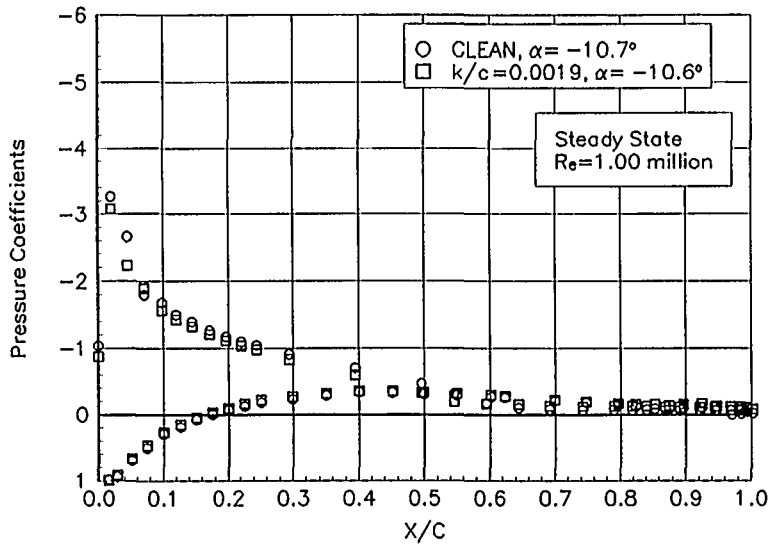
Figure B32. $\alpha = -10.7°$
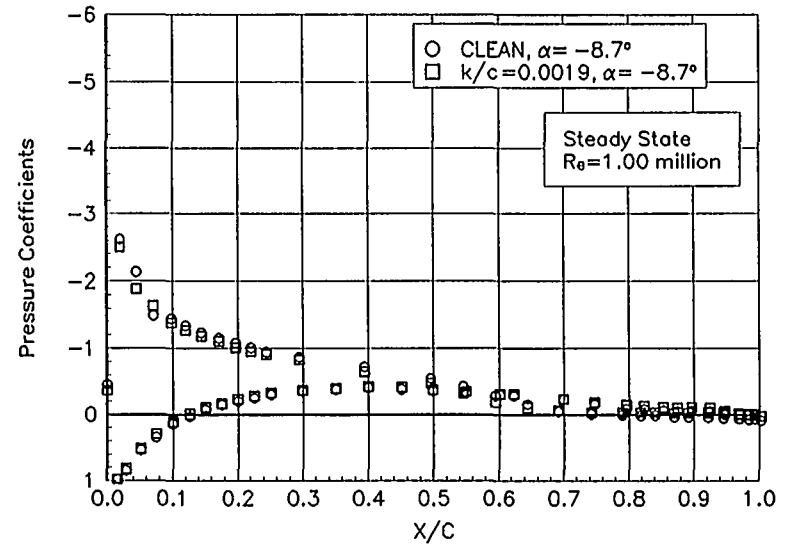
Figure B33. $\alpha = -8.7°$
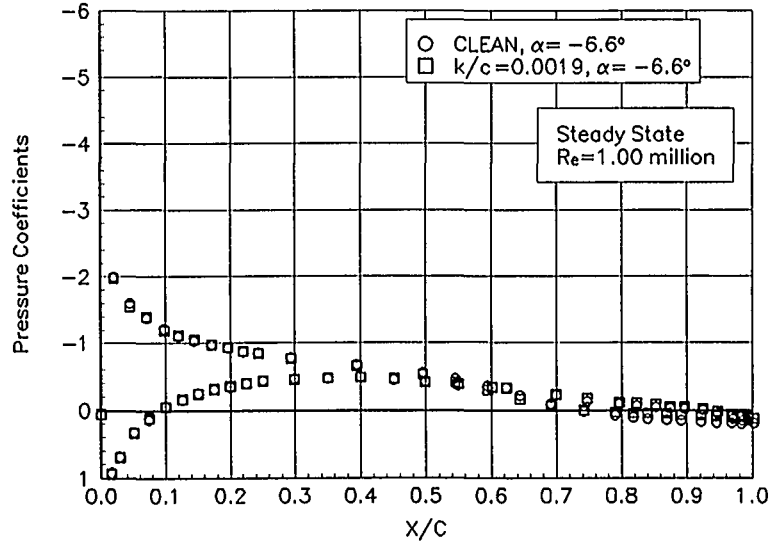
Figure B34. $\alpha = -6.6°$

Figure B35. $\alpha = -4.6°$

B-28

Figure B36. α = -2.6°

Figure B37. α = -0.5°

Figure B38. α = 1.6°

Figure B39. α = 3.6°

B-29
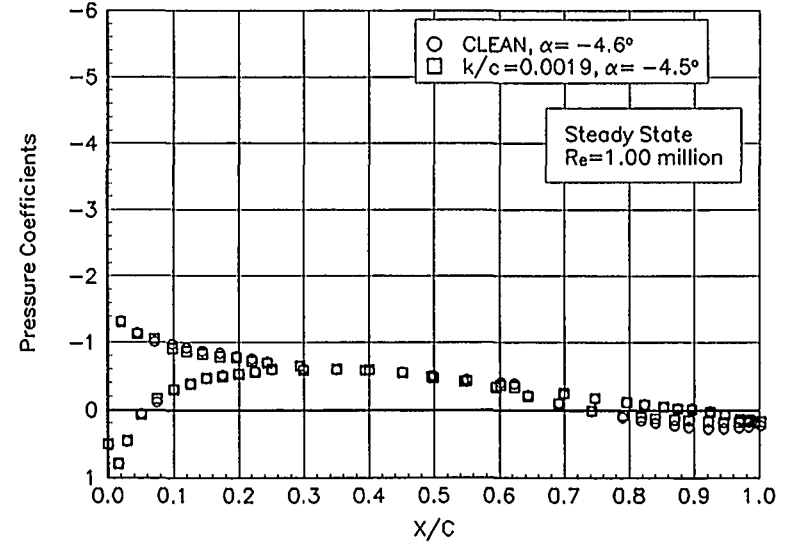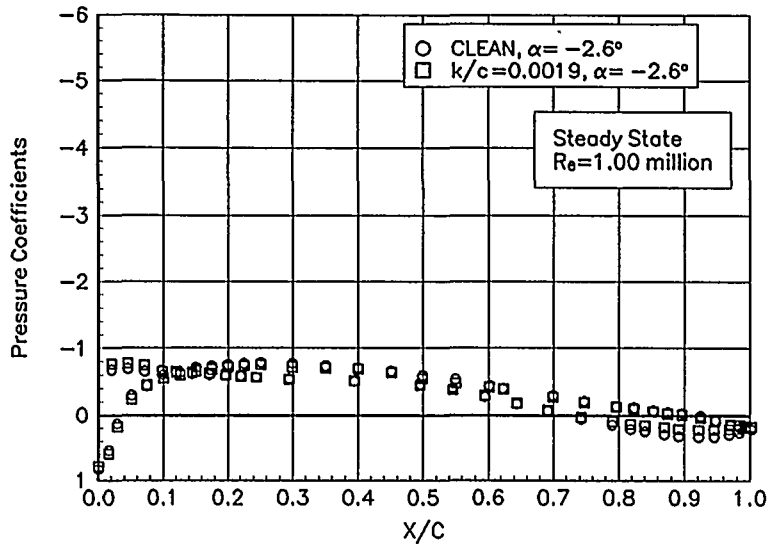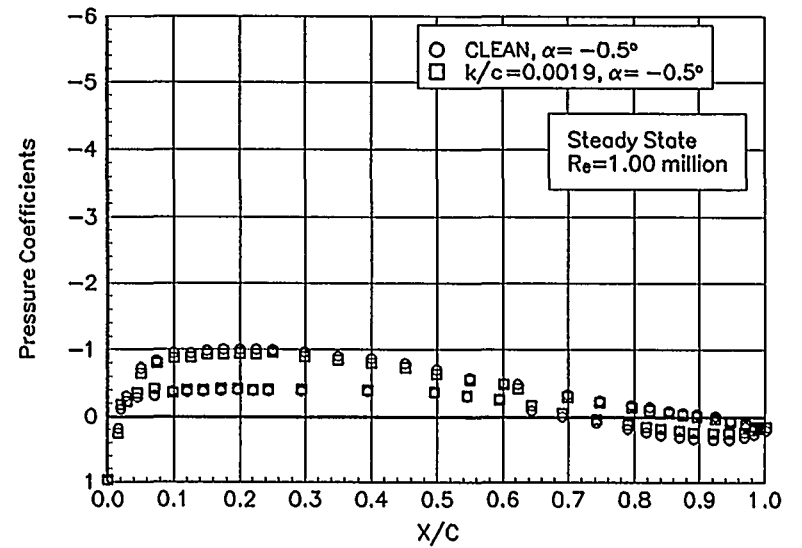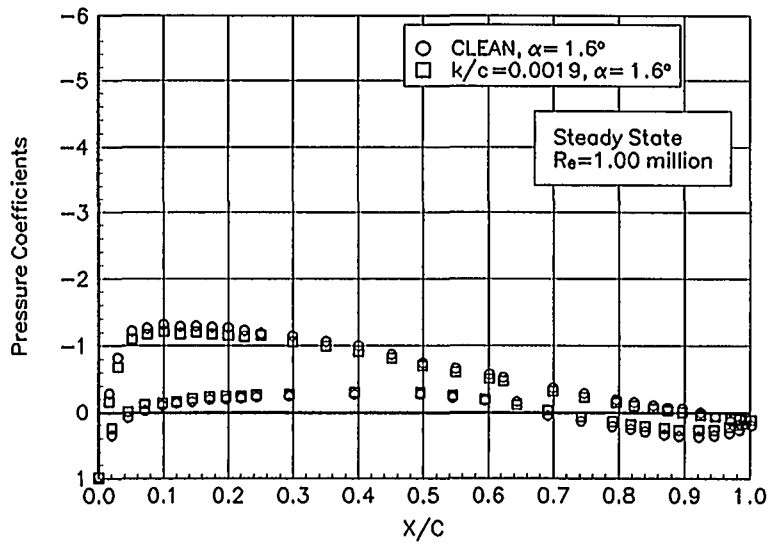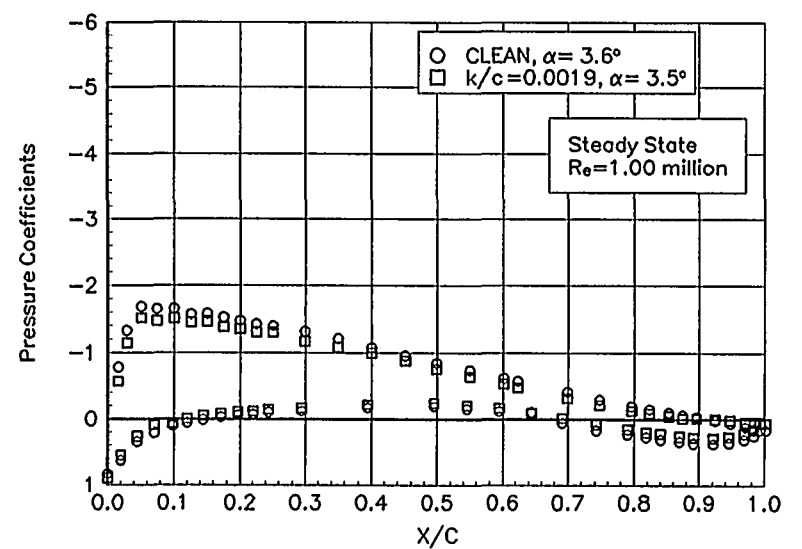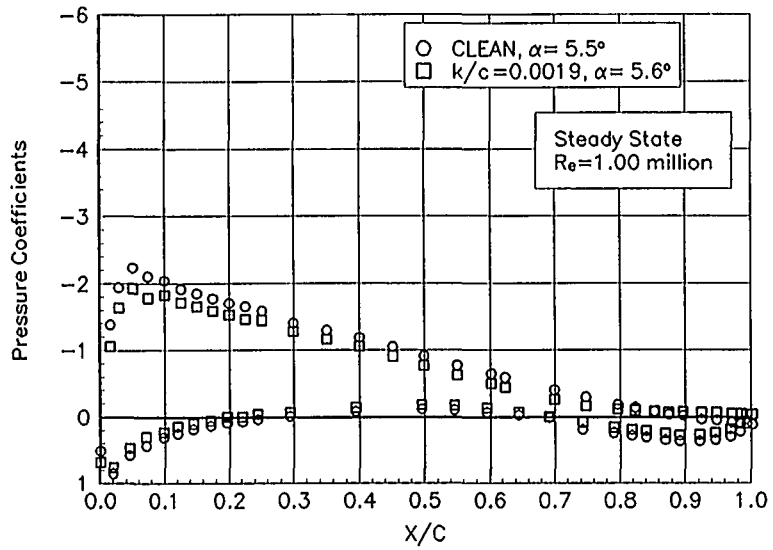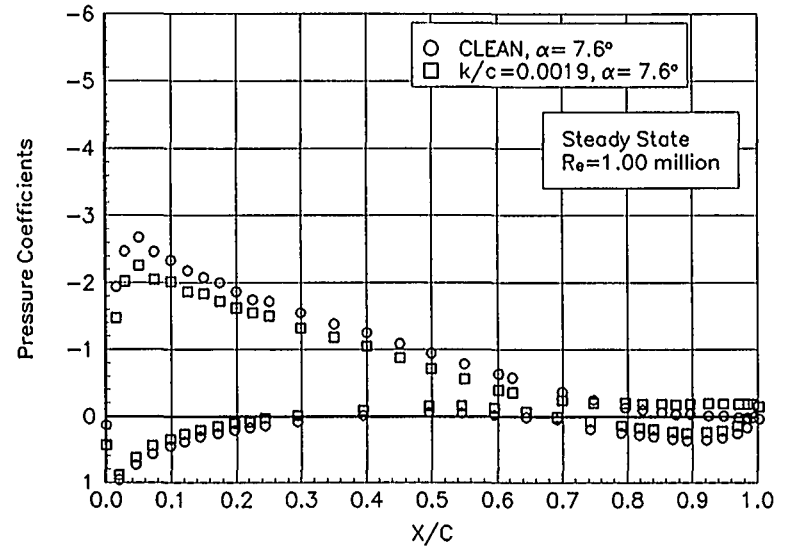
Figure B40. $\alpha = 5.5°$

Figure B41. $\alpha = 7.6°$
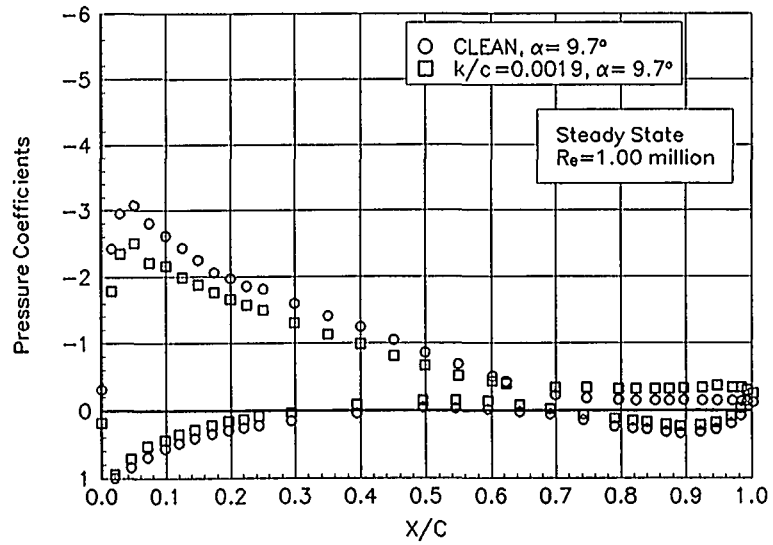
Figure B42. $\alpha = 9.7°$
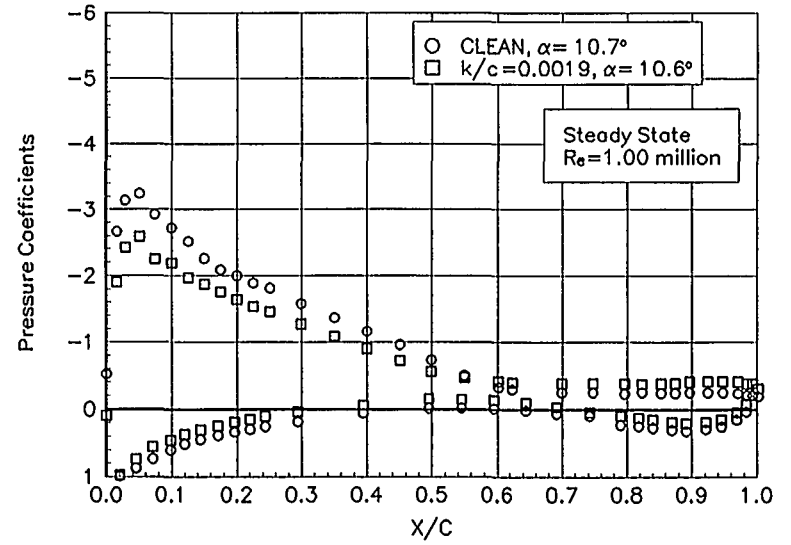
Figure B43. $\alpha = 10.7°$
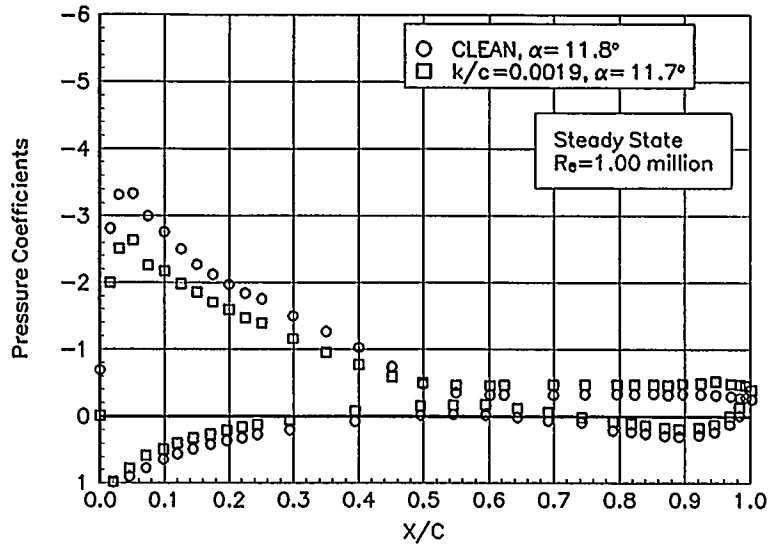
Figure B44. $\alpha = 11.8°$
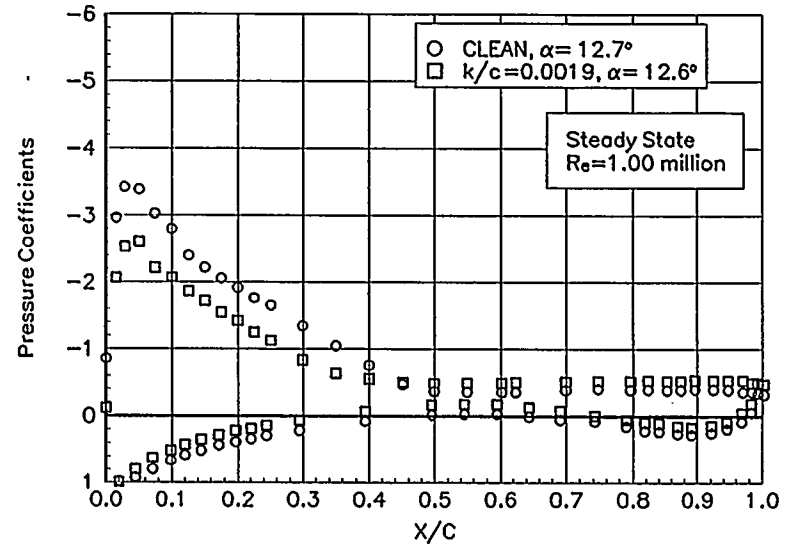
Figure B45. $\alpha = 12.7°$
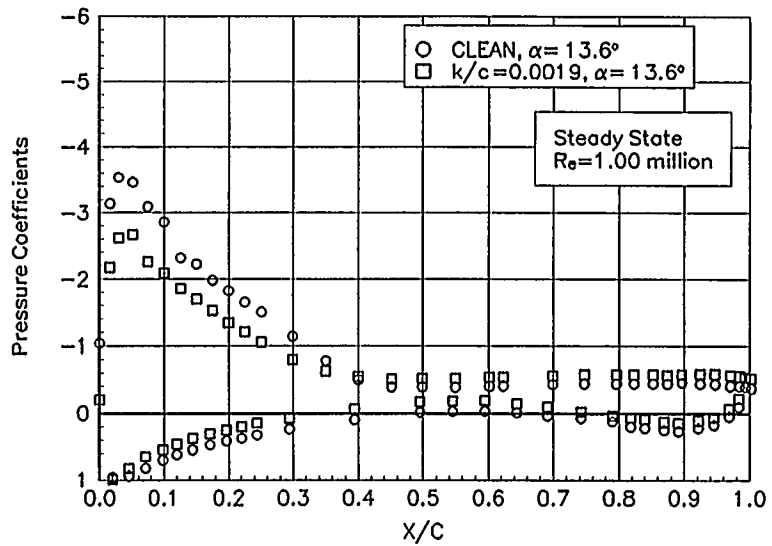
Figure B46. $\alpha = 13.6°$

Figure B47. $\alpha = 14.6°$

B-31
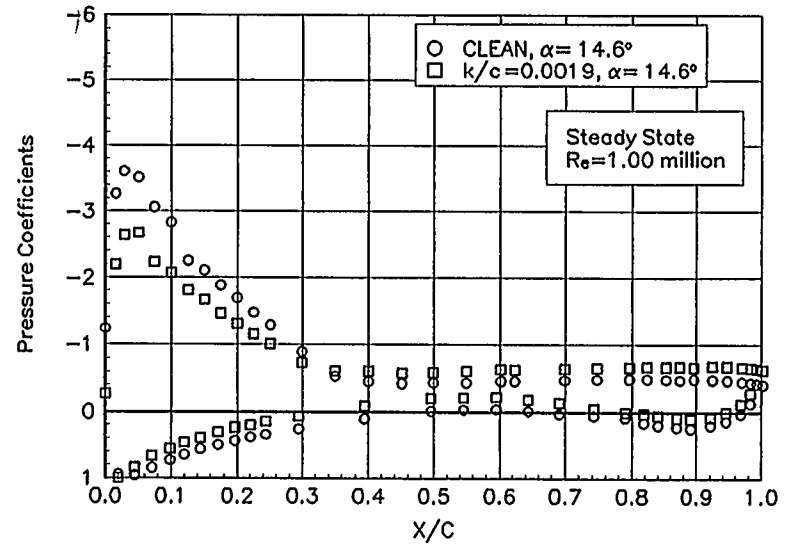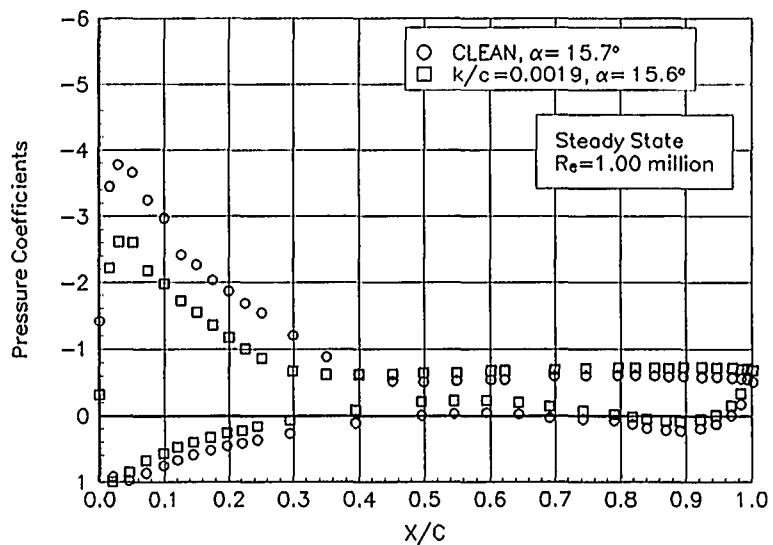
Figure B48. $\alpha = 15.7°$
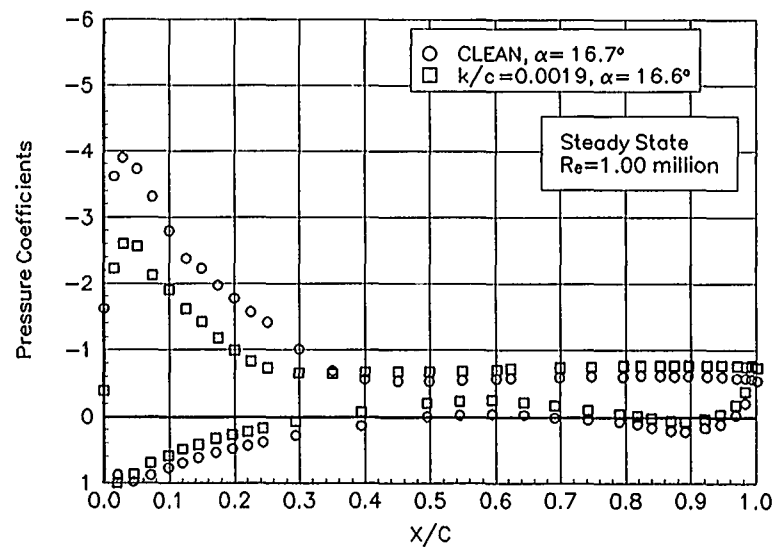
Figure B49. $\alpha = 16.7°$
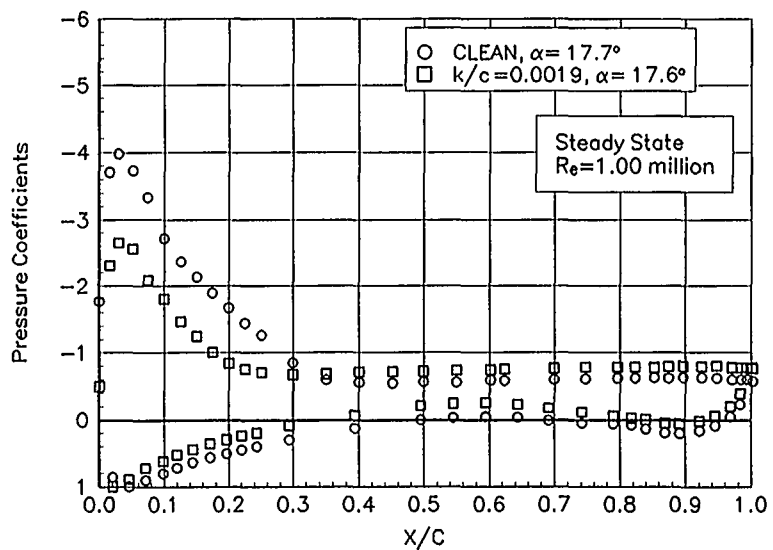
Figure B50. $\alpha = 17.7°$
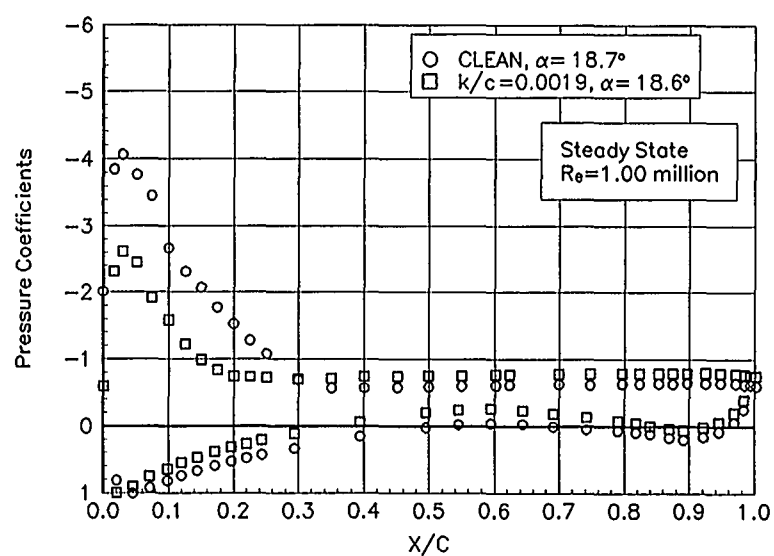
Figure B51. $\alpha = 18.7°$
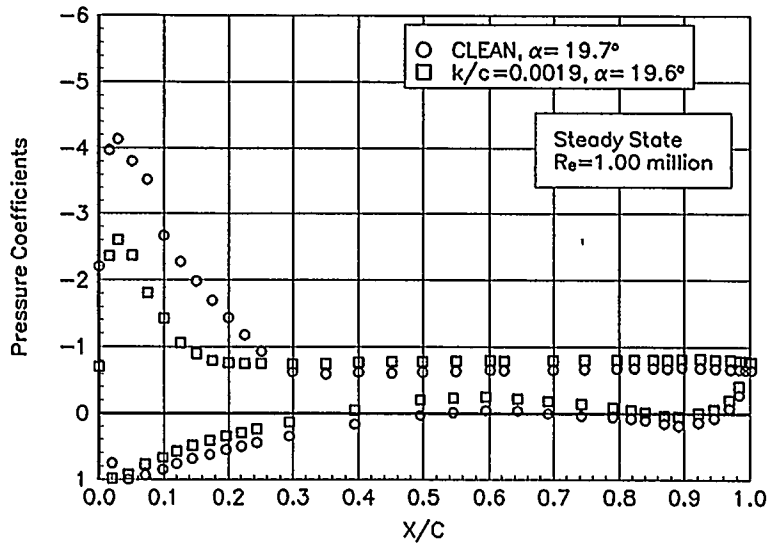
Figure B52. $\alpha = 19.7°$
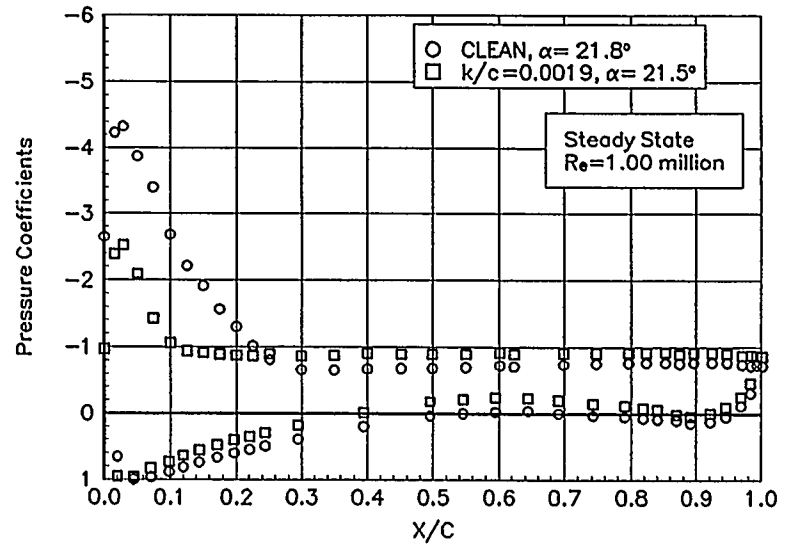
Figure B53. $\alpha = 21.8°$
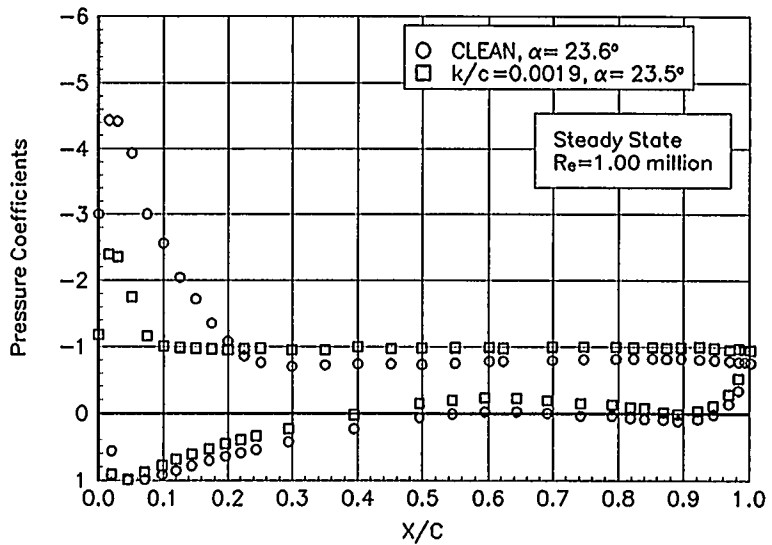
Figure B54. $\alpha = 23.6°$

Figure B55. $\alpha = 25.7°$

B-33
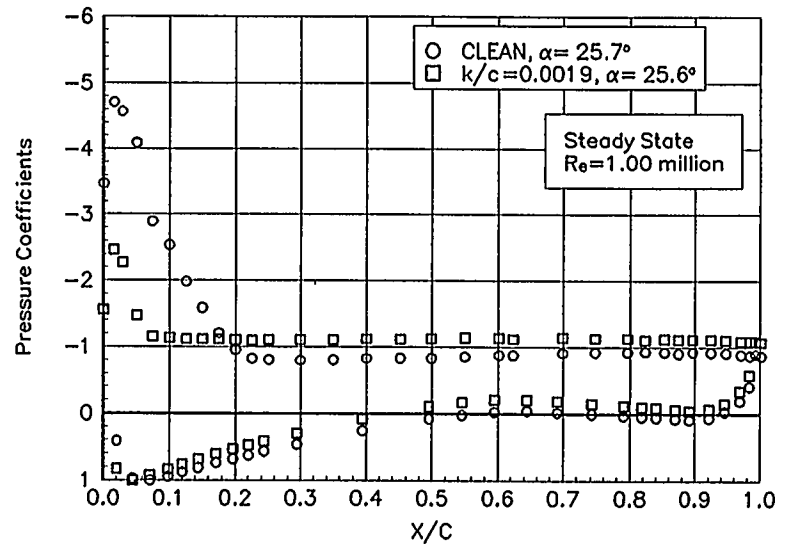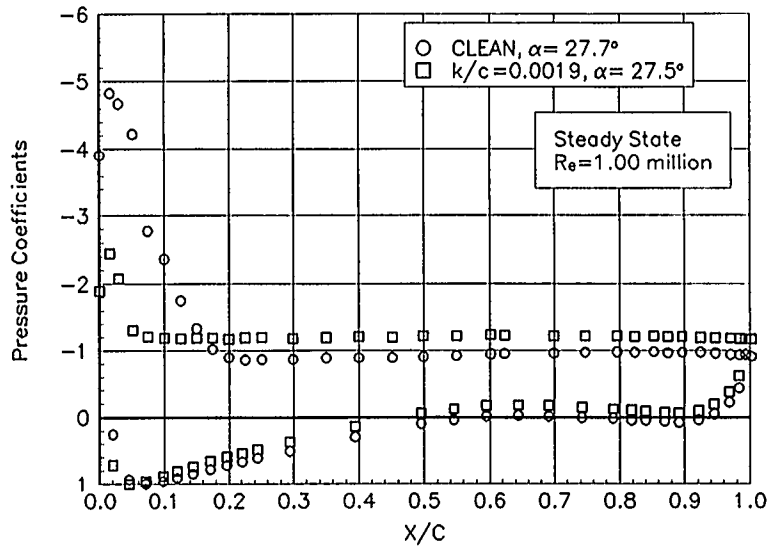
Figure B56. $\alpha = 27.7°$
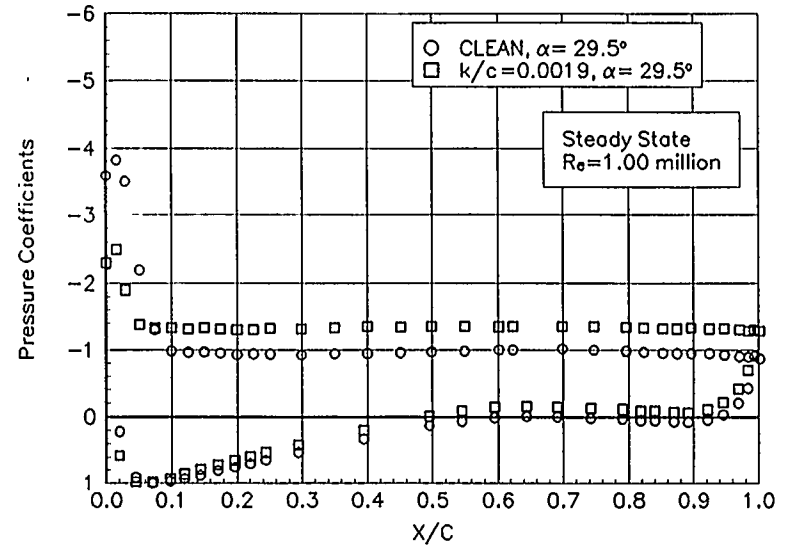
Figure B57. $\alpha = 29.5°$
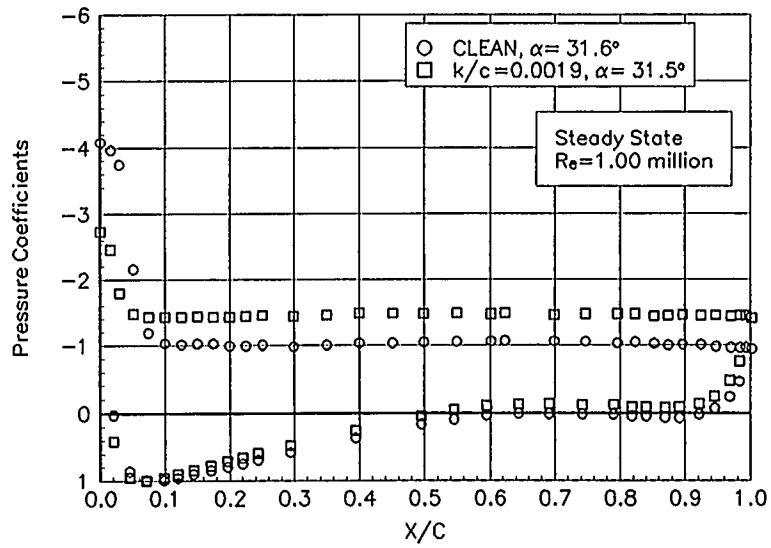
Figure B58. $\alpha = 31.6°$

Figure B59. $\alpha = 33.6°$

B-34

Figure B60. $\alpha = 35.6°$

Figure B61. $\alpha = 37.5°$

Figure B62. $\alpha = 39.5°$

B-35
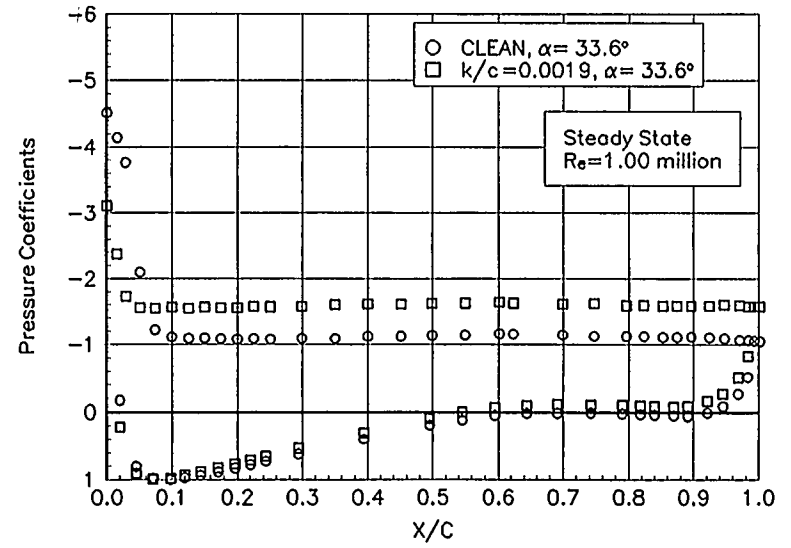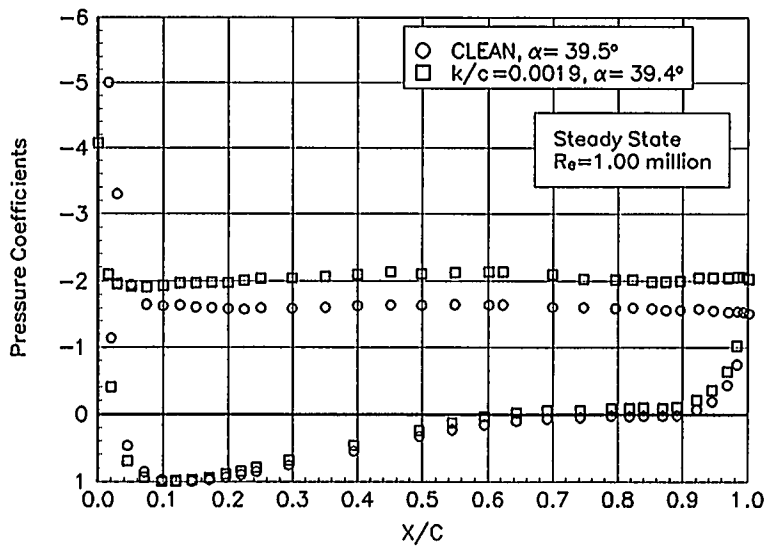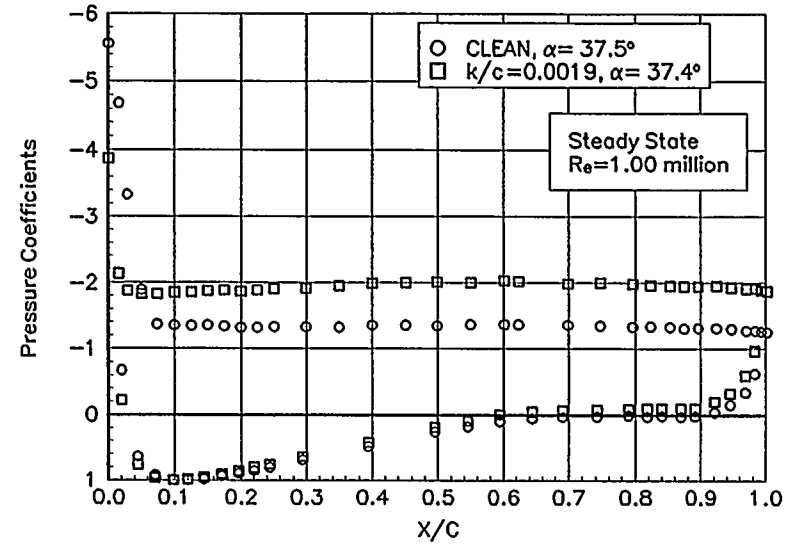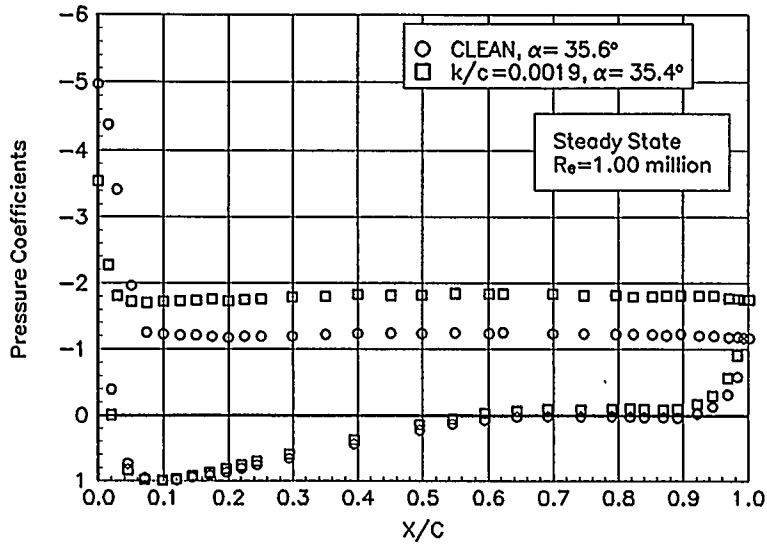
LS(1)-0421MOD

Pressure Distributions, Steady State, Re = 1.25 million
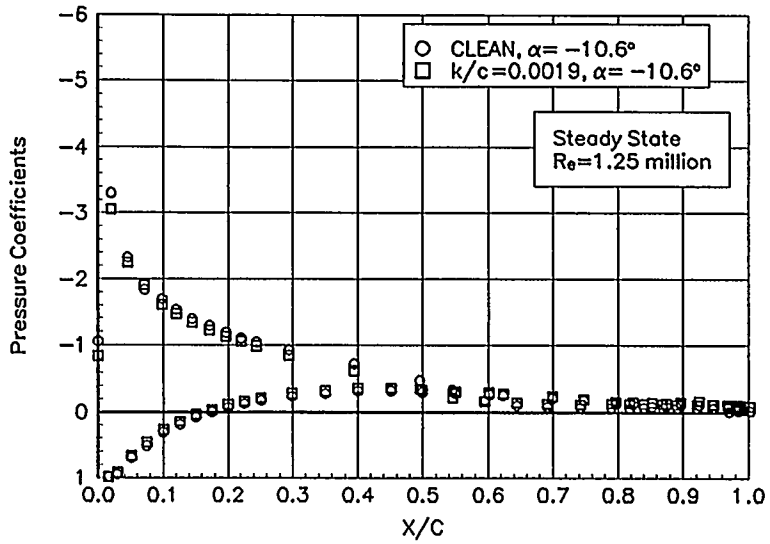
Figure B63. $\alpha = -10.6°$
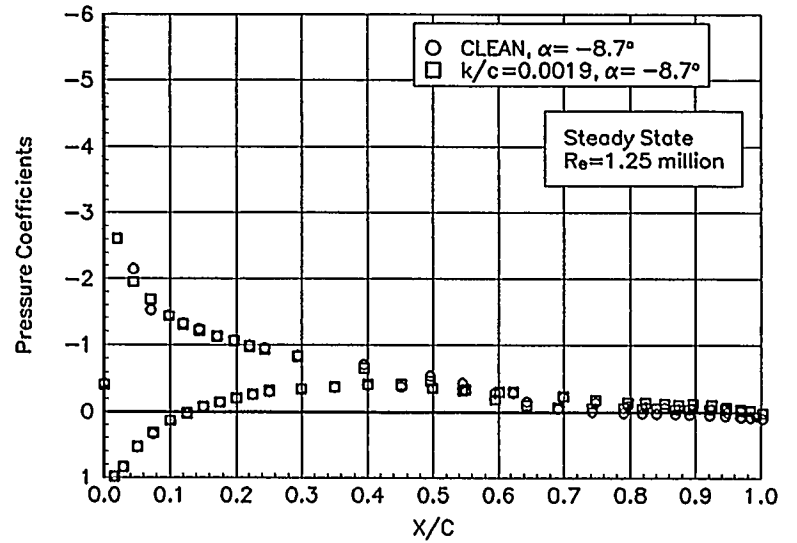
Figure B64. $\alpha = -8.7°$
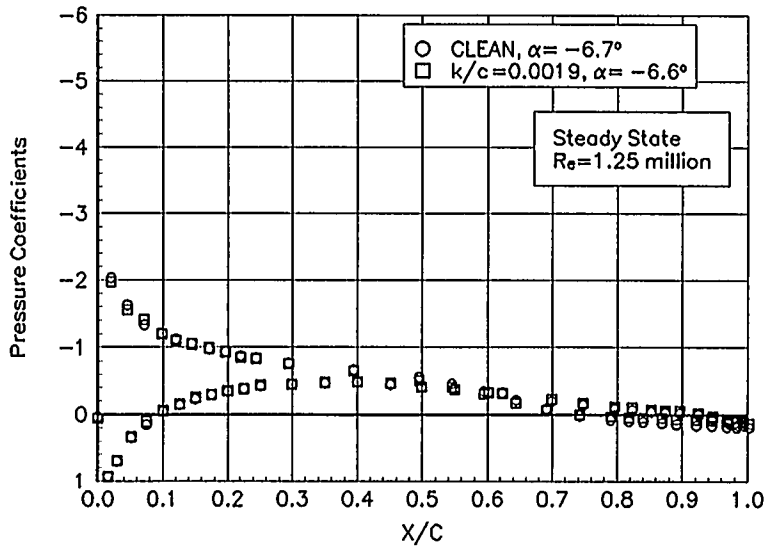
Figure B65. $\alpha = -6.7°$

Figure B66. $\alpha = -4.5°$

B-37
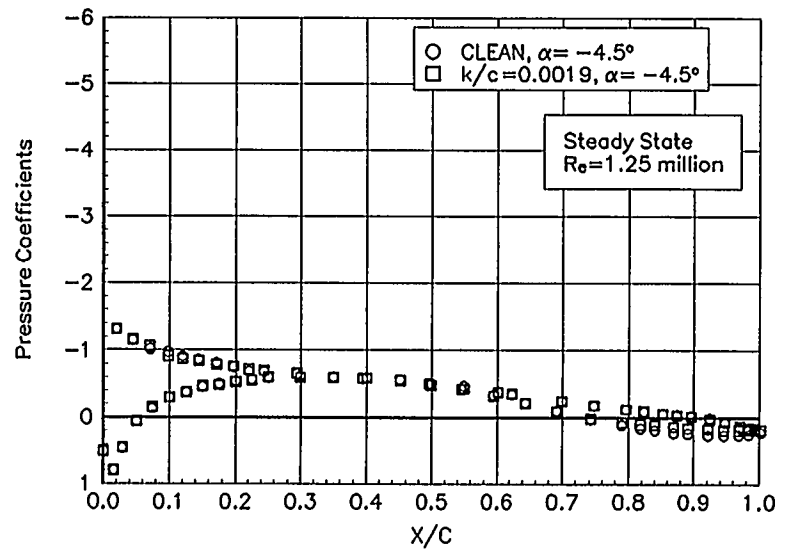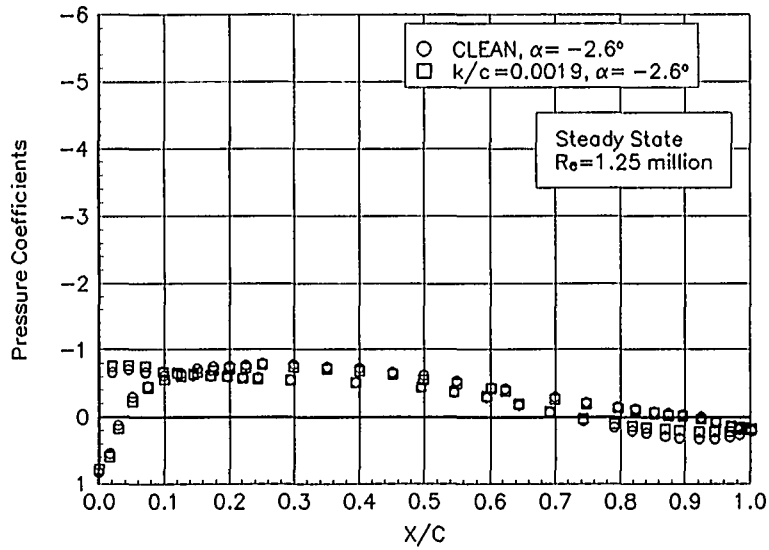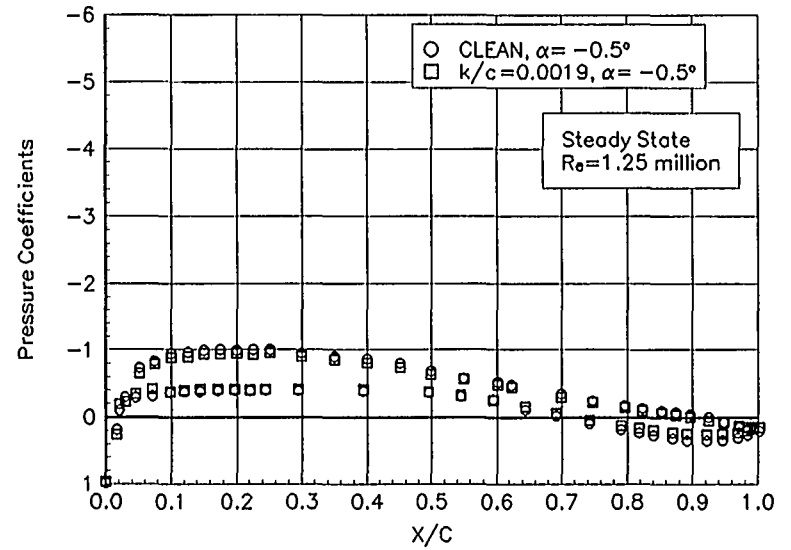
Figure B67. $\alpha = -2.6°$

Figure B68. $\alpha = -0.5°$
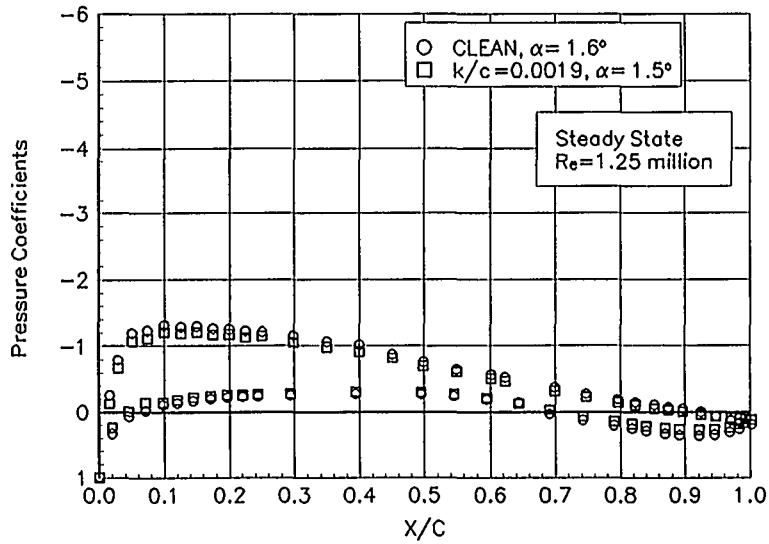
Figure B69. $\alpha = 1.6°$

Figure B70. $\alpha = 3.6°$

B-38
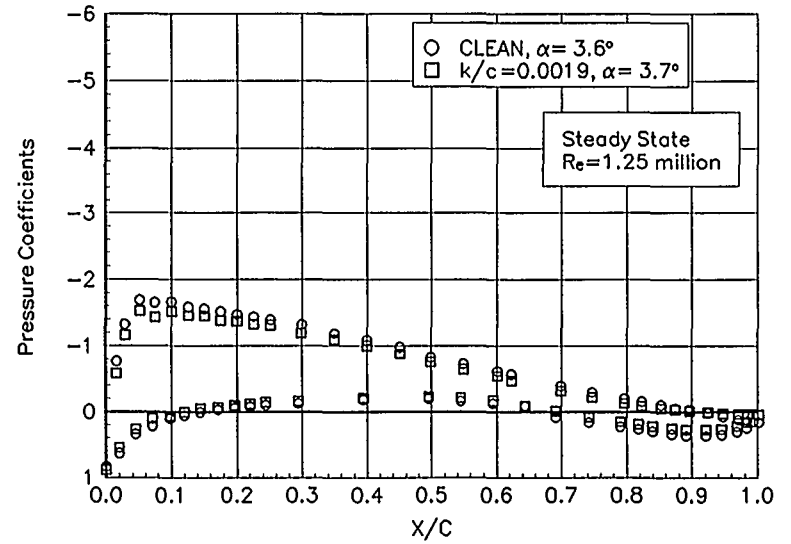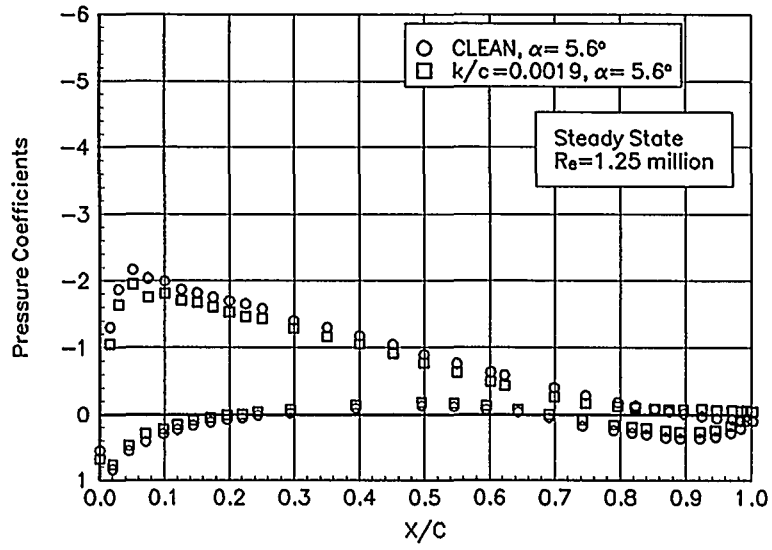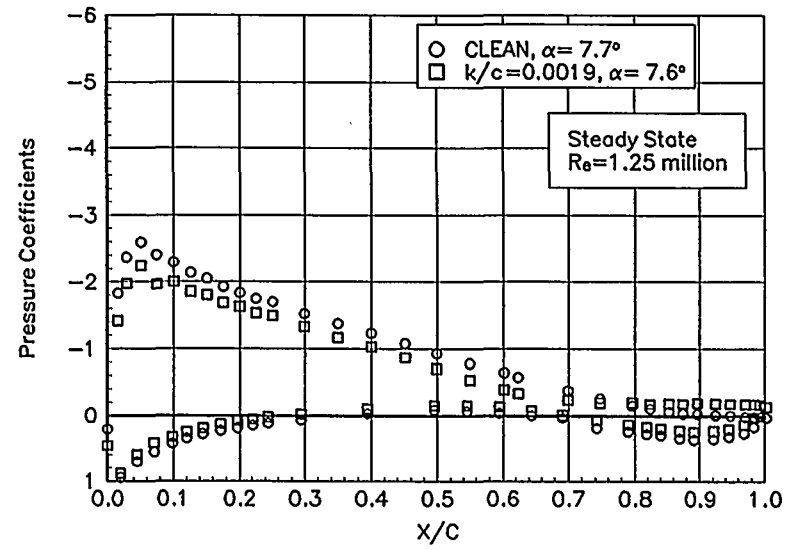
Figure B71. $\alpha = 5.6°$

Figure B72. $\alpha = 7.7°$
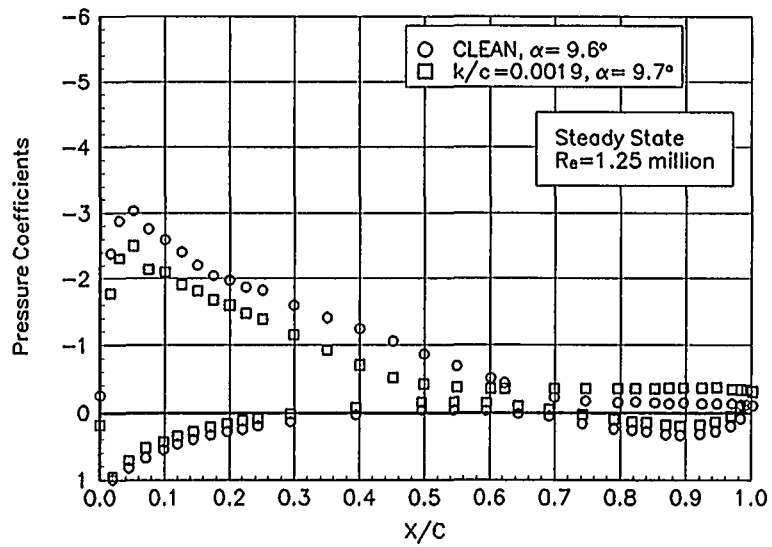
Figure B73. $\alpha = 9.6°$
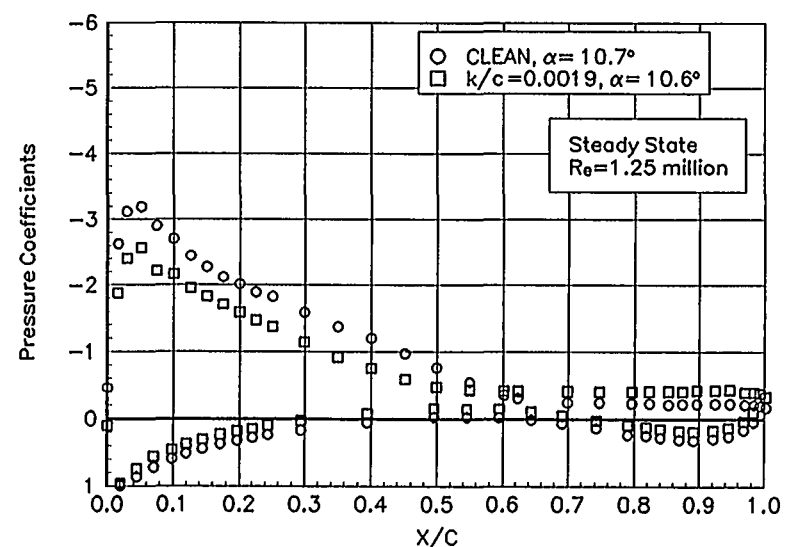
Figure B74. $\alpha = 10.7°$

Figure B75. $a = 11.6°$

Figure B76. $a = 12.7°$

Figure B77. $a = 13.7°$

Figure B78. $a = 14.7°$

B-40
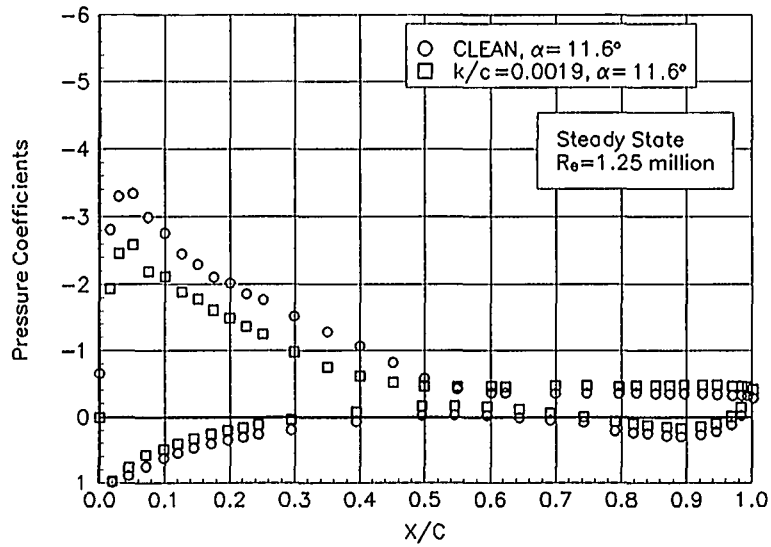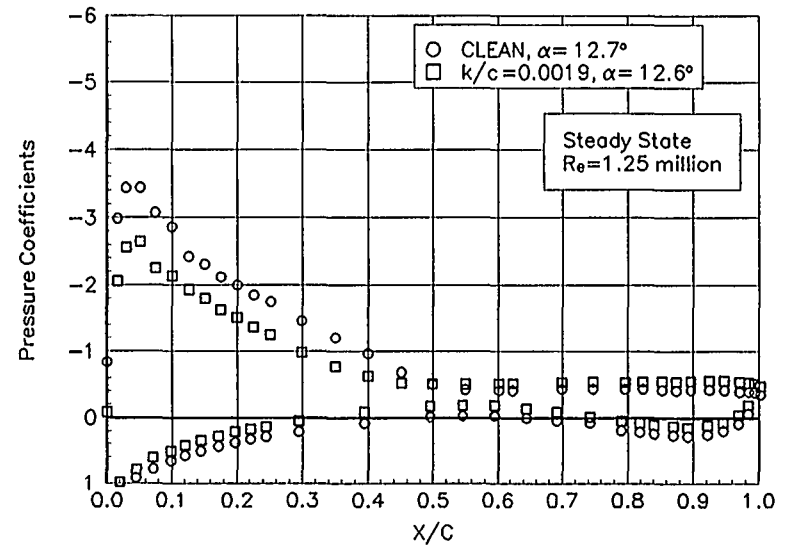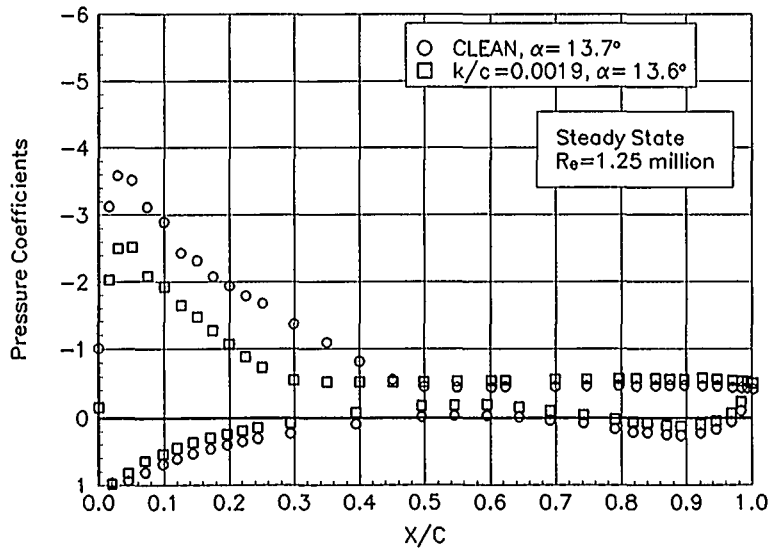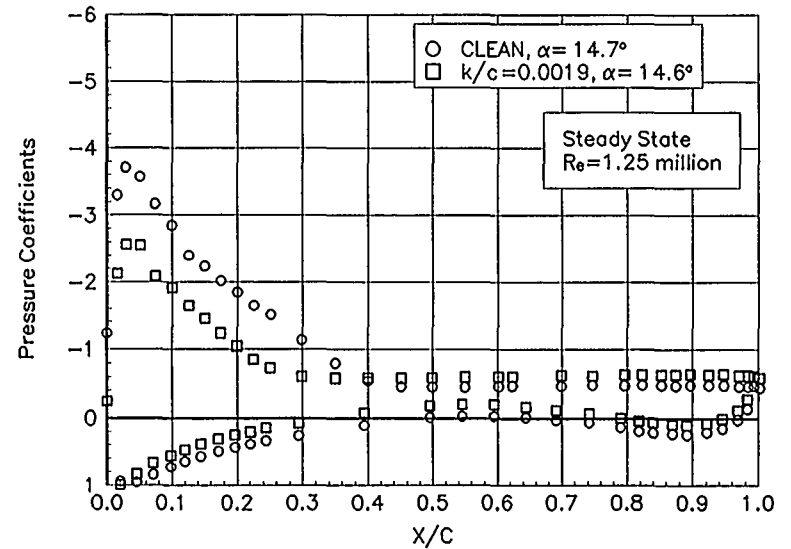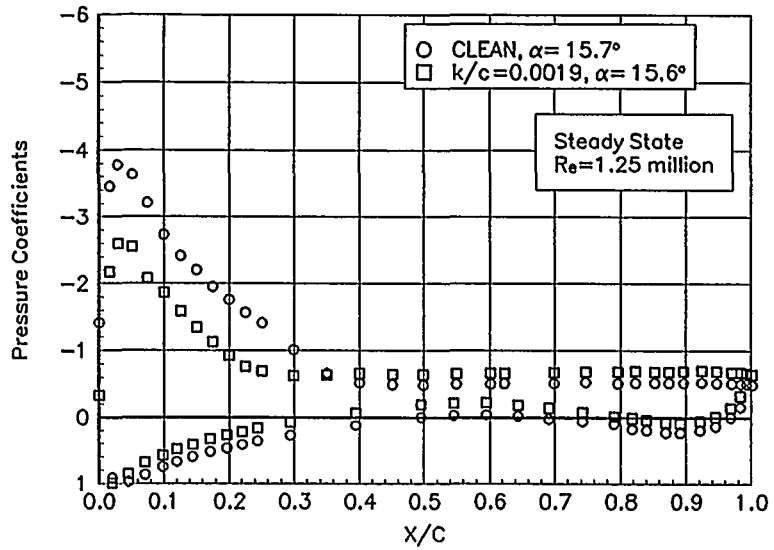
Figure B79. $\alpha = 15.7°$
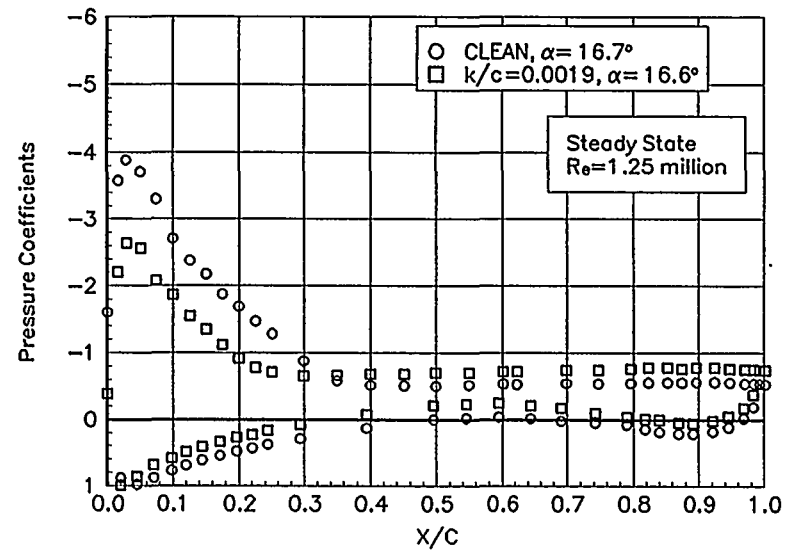
Figure B80. $\alpha = 16.7°$
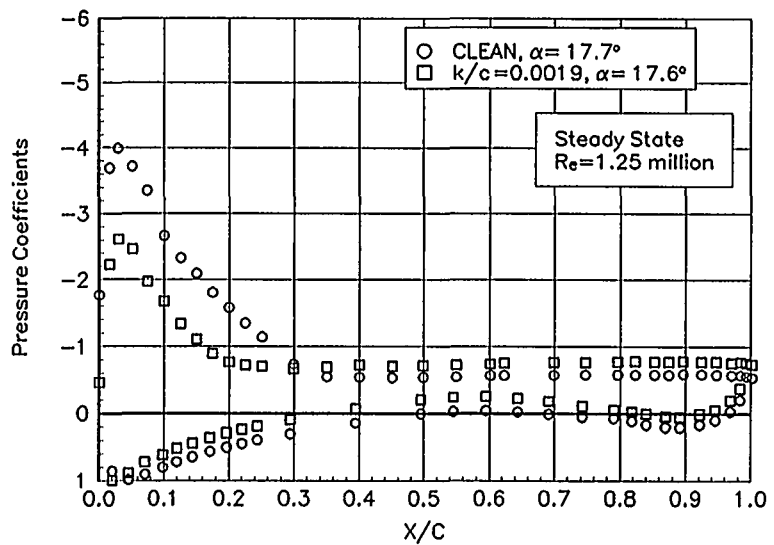
Figure B81. $\alpha = 17.7°$

Figure B82. $\alpha = 18.6°$

B-41
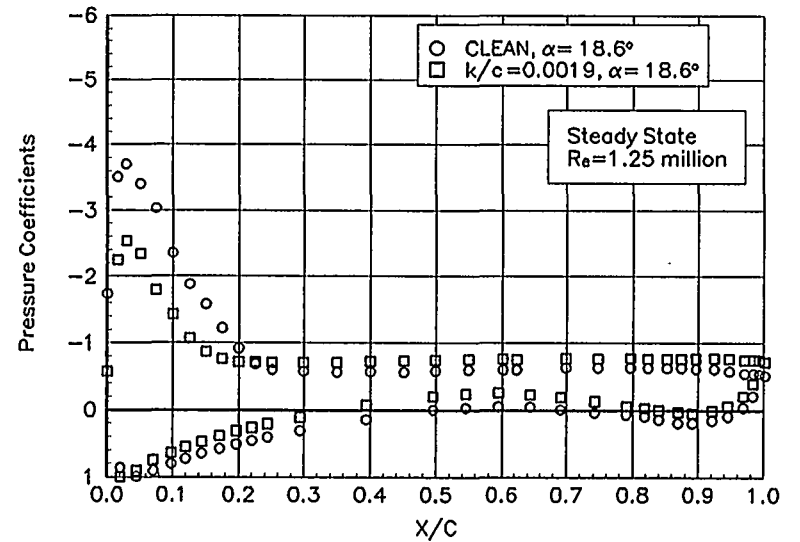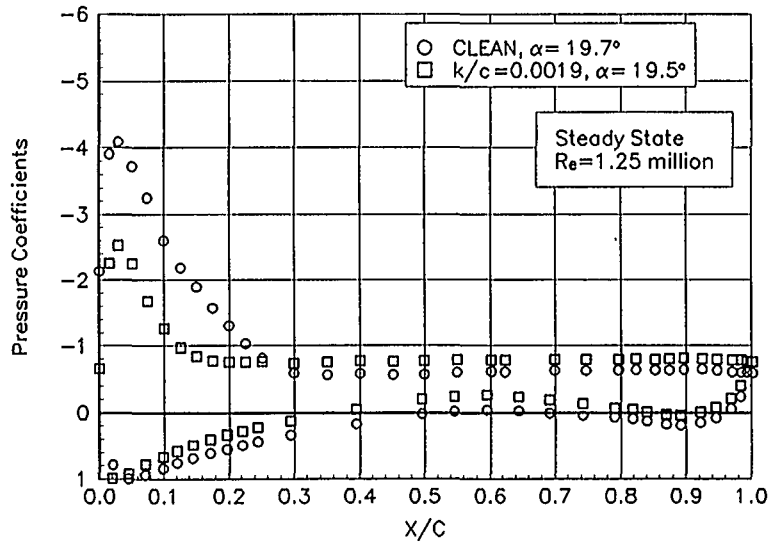
Figure B83. $\alpha = 19.7°$
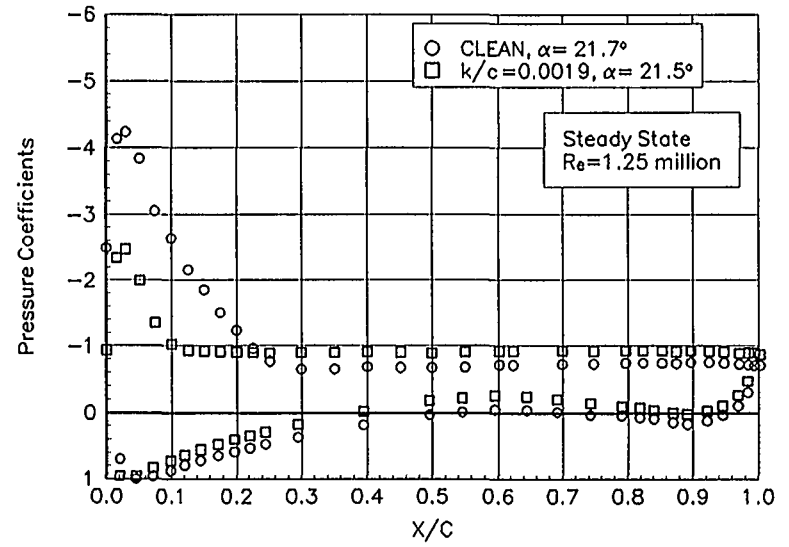
Figure B84. $\alpha = 21.7°$
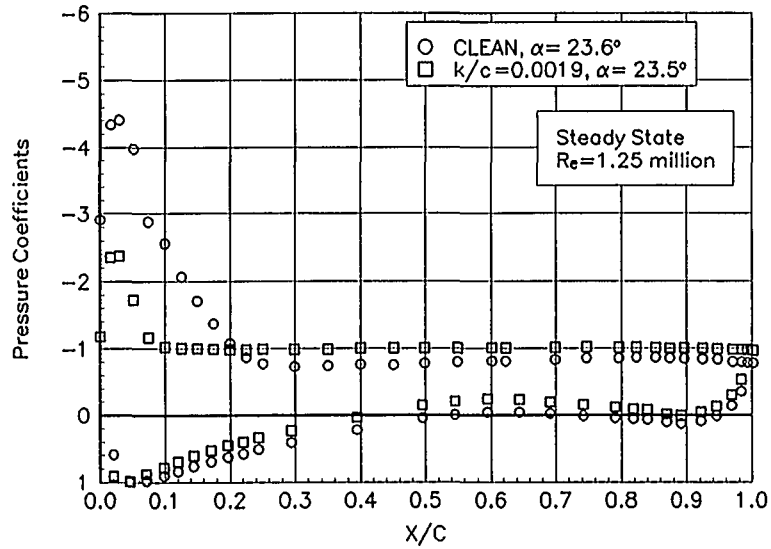
Figure B85. $\alpha = 23.6°$

Figure B86. $\alpha = 25.6°$

B-42
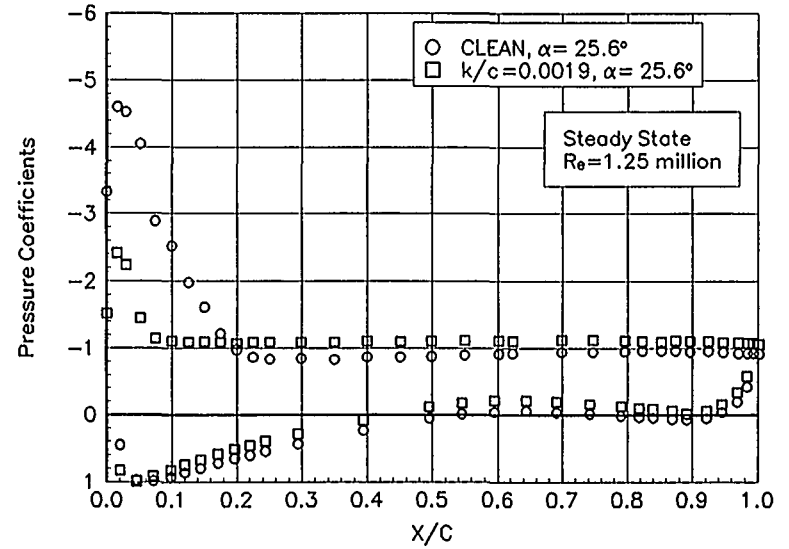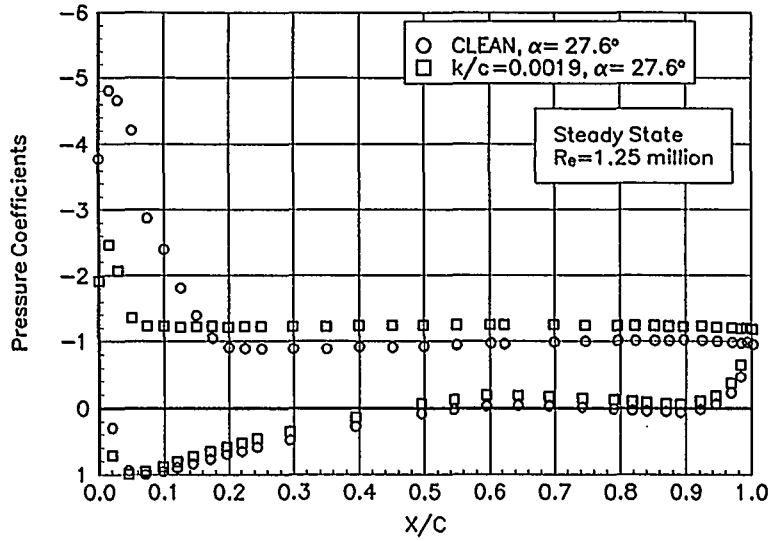
Figure B87. $\alpha = 27.6°$
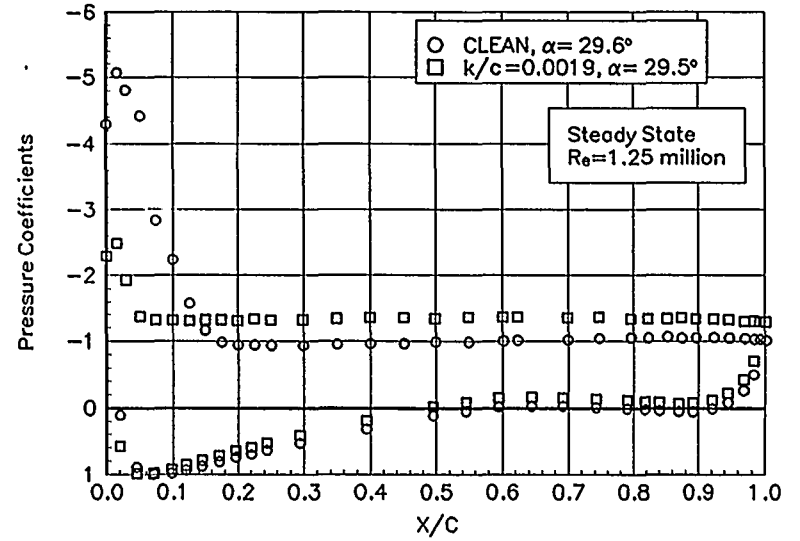
Figure B88. $\alpha = 39.6°$
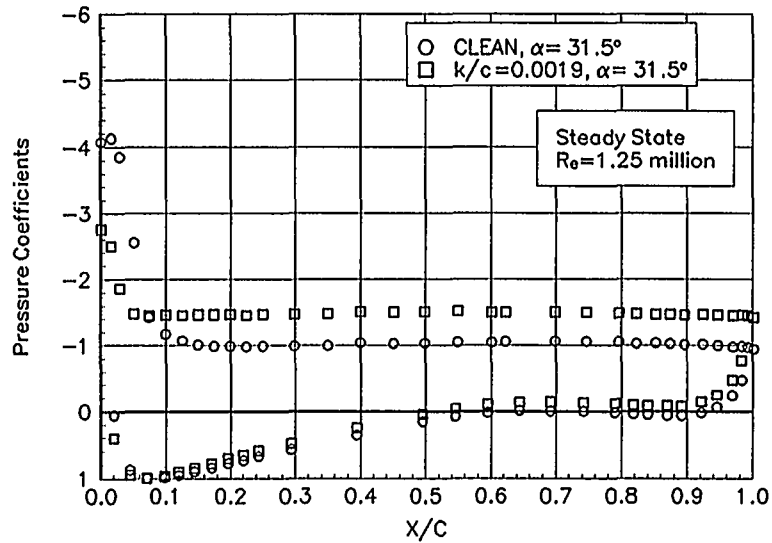
Figure B89. $\alpha = 31.5°$

Figure B90. $\alpha = 33.6°$

Figure B91. $\alpha = 35.6°$

Figure B92. $\alpha = 37.6°$
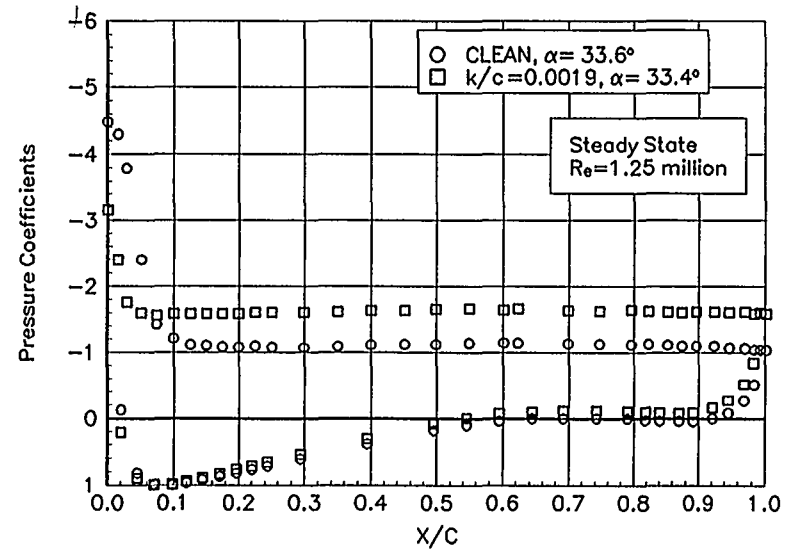
Figure B93. $\alpha = 39.6°$
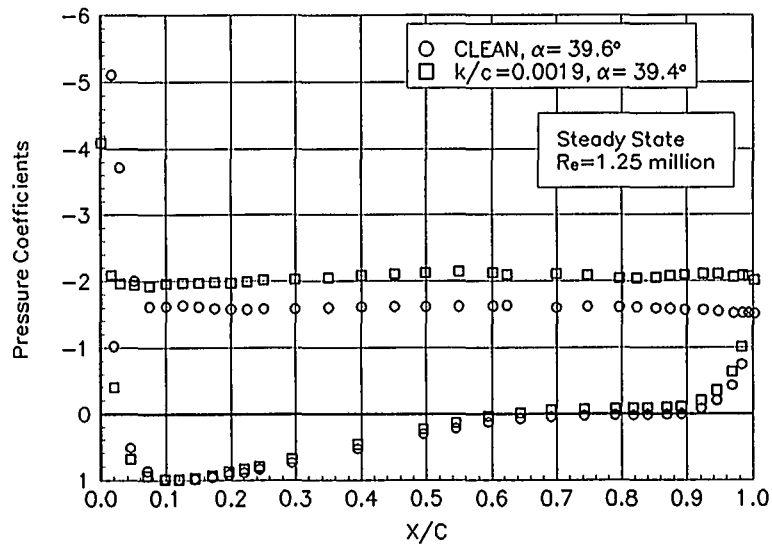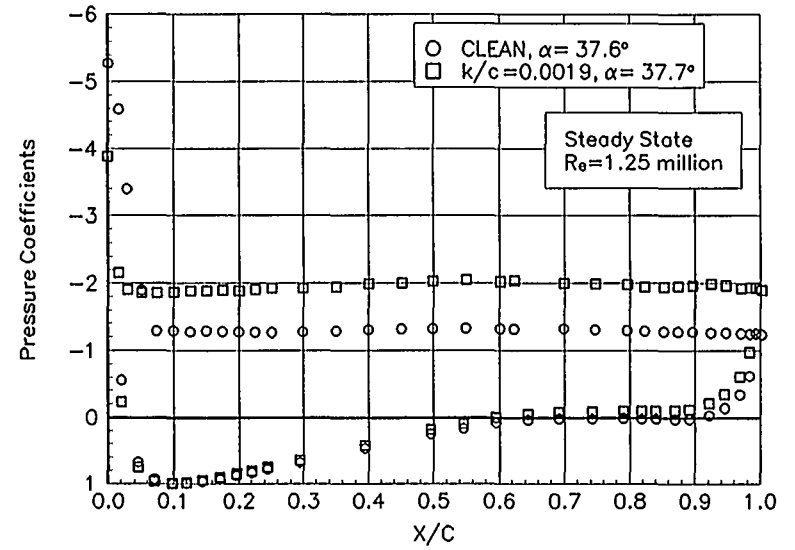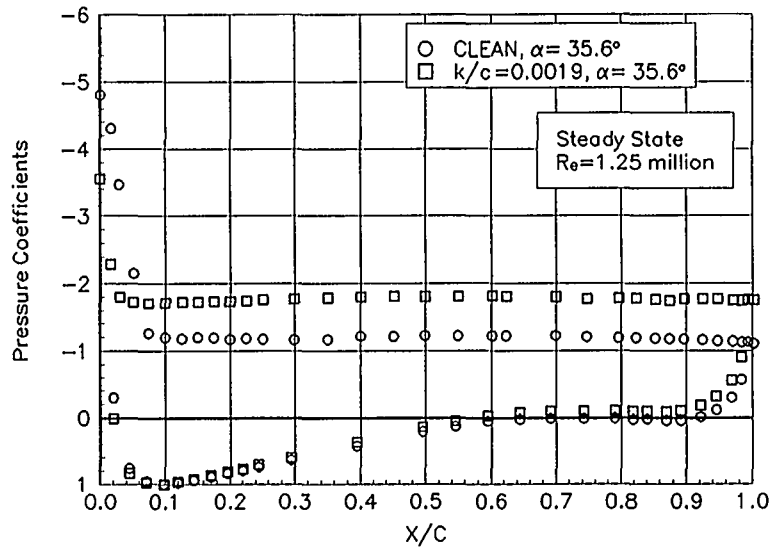
Appendix C: Unsteady Data

Integrated Coefficients

List of Figures　　　　　　　Page

Unsteady Airfoil Characteristics

$\pm 5°$ Sine

Re = 0.75 Million
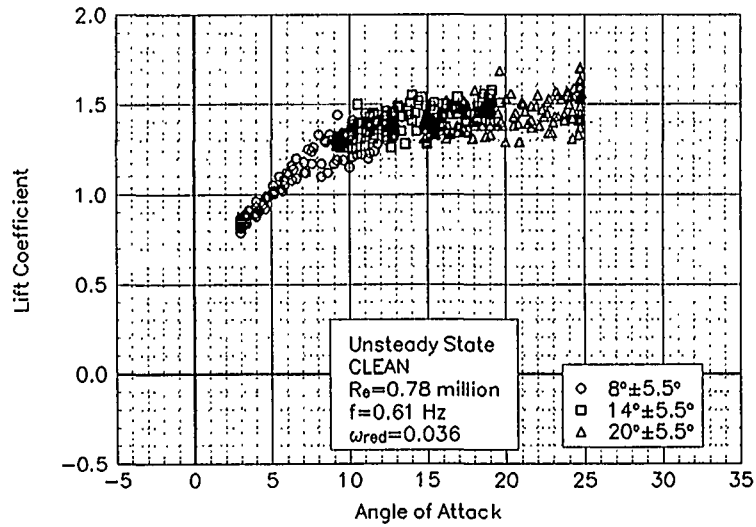
Figure C1. Lift coefficient vs α.

LS(1)-0421MOD
Clean
Re = 0.75 Million
$\omega_{red} = 0.036$
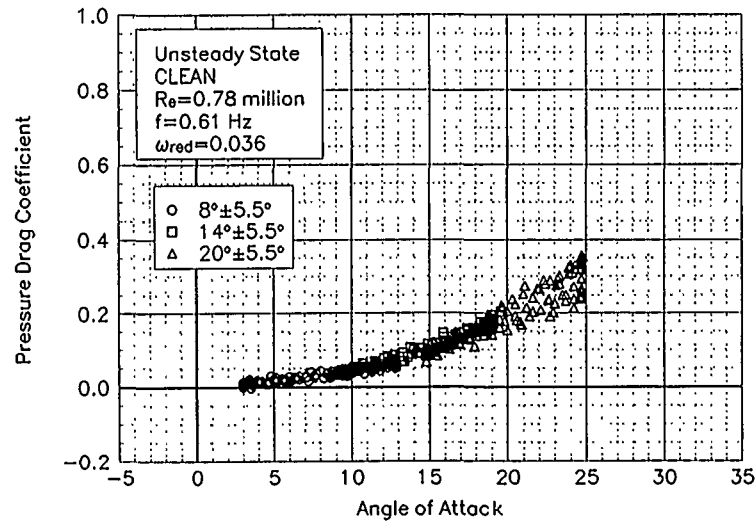
Figure C2. Pressure drag coefficient vs α.
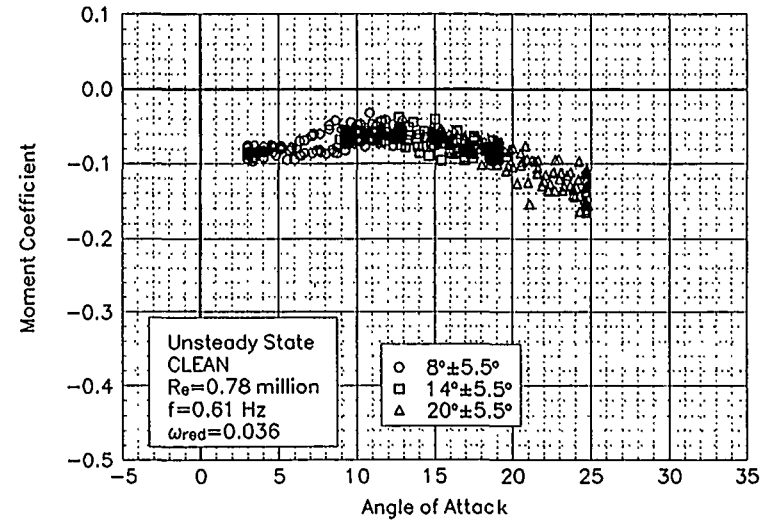
Figure C3. Moment coefficient vs α.
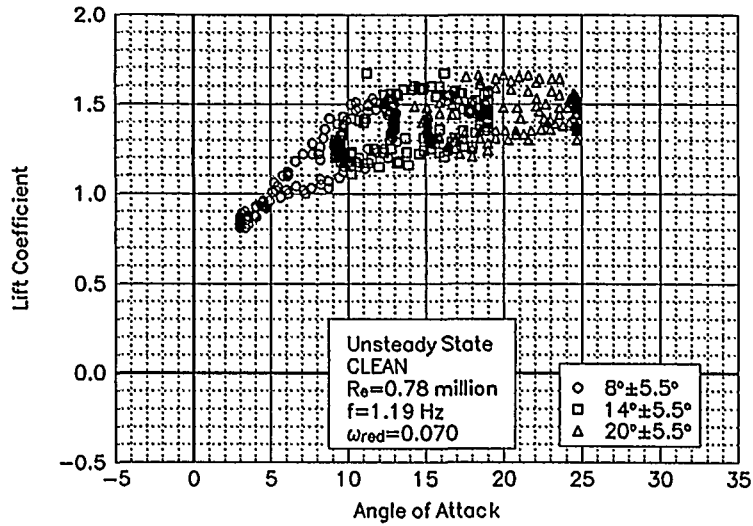
Figure C4. Lift coefficient vs α.

LS(1)-0421MOD
Clean
Re = 0.75 Million
$\omega_{red} = 0.070$
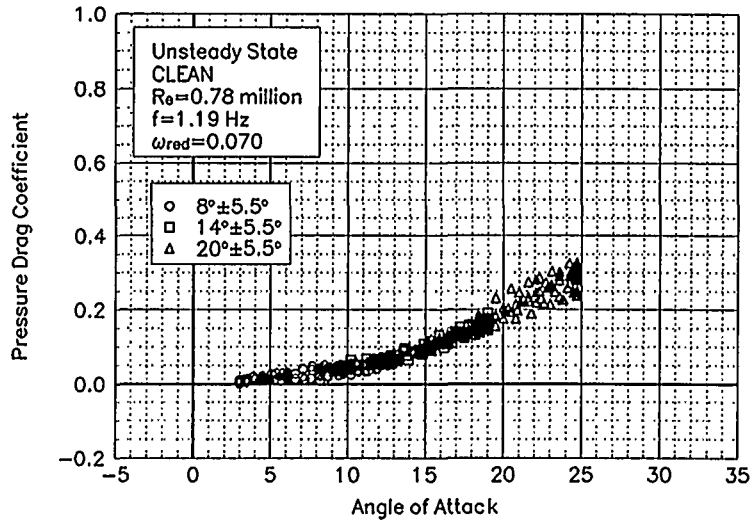
Figure C5. Pressure drag coefficient vs α.
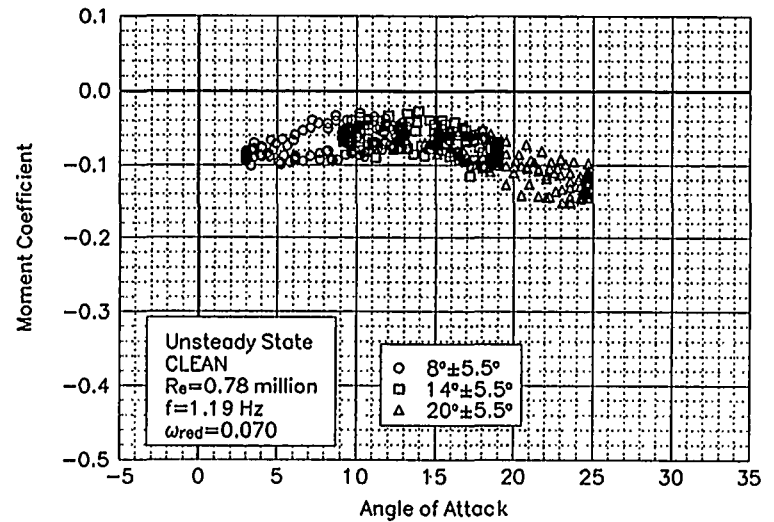
Figure C6. Moment coefficient vs α.
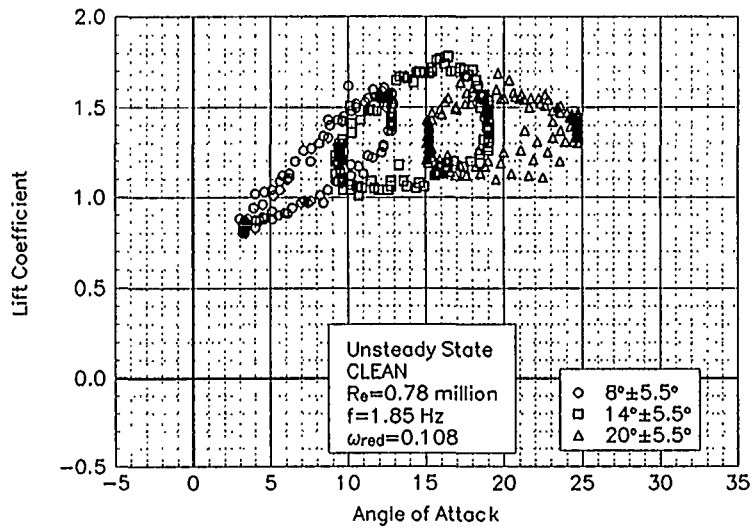
Figure C7. Lift coefficient vs a.

LS(1)-0421MOD
Clean
Re = 0.75 Million
$\omega_{red} = 0.108$
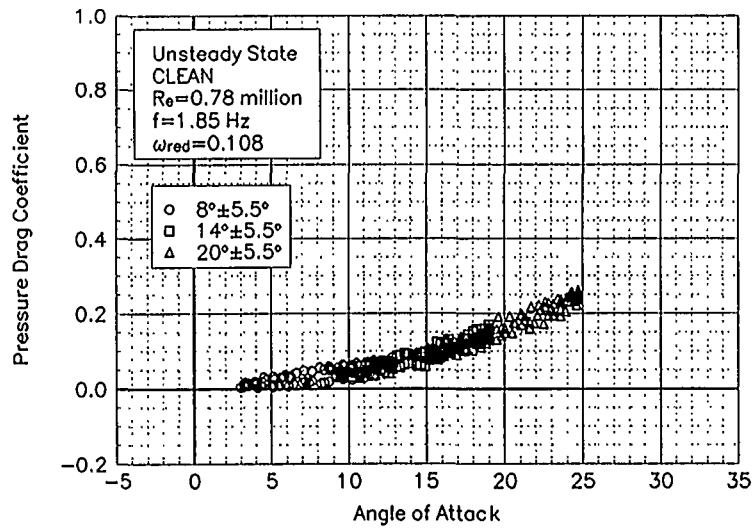
Figure C8. Pressure drag coefficient vs a.
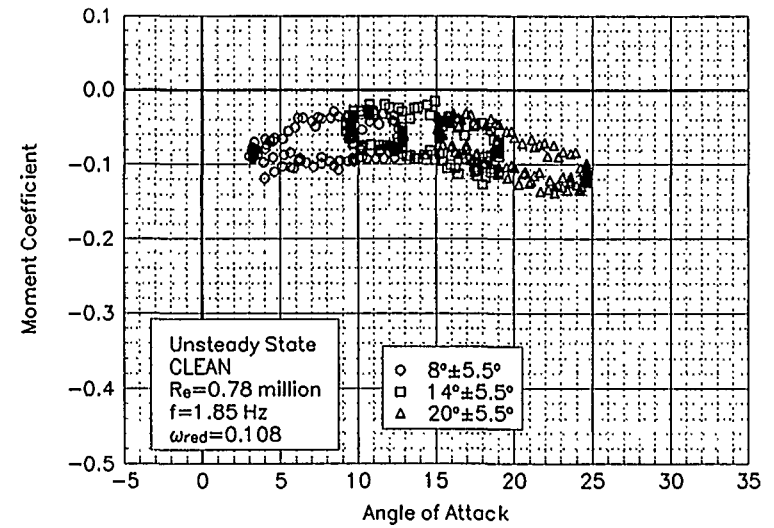
Figure C9. Moment coefficient vs a.
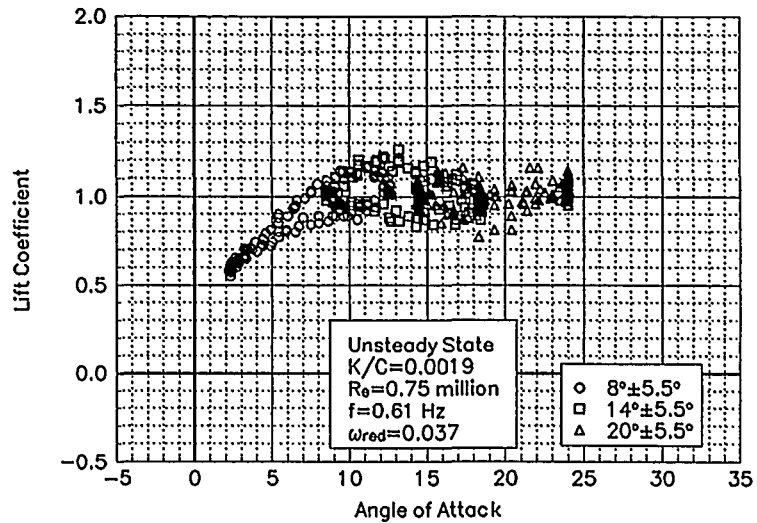
Figure C10. Lift coefficient vs α.

LS(1)-0421MOD
LEGR
Re = 0.75 Million
$\omega_{red} = 0.037$
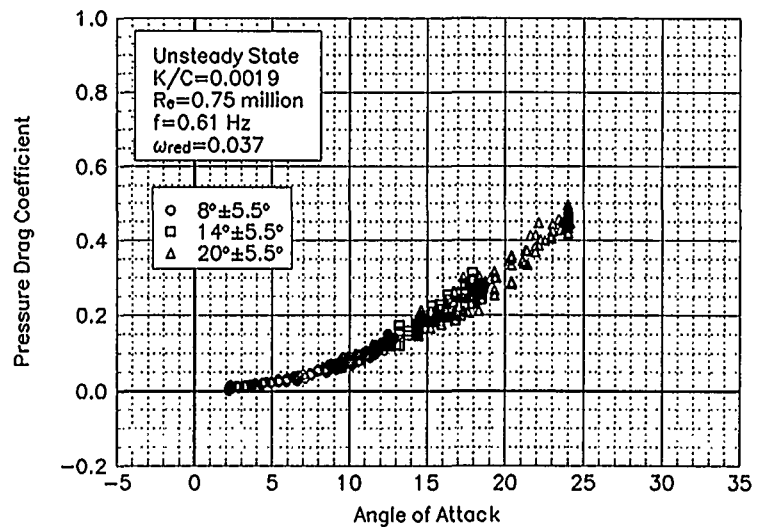
Figure C11. Pressure drag coefficient vs α.
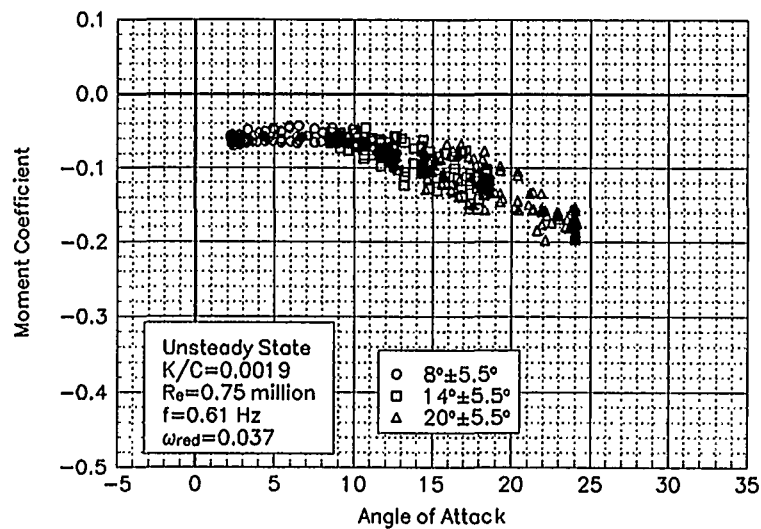
Figure C12. Moment coefficient vs α.
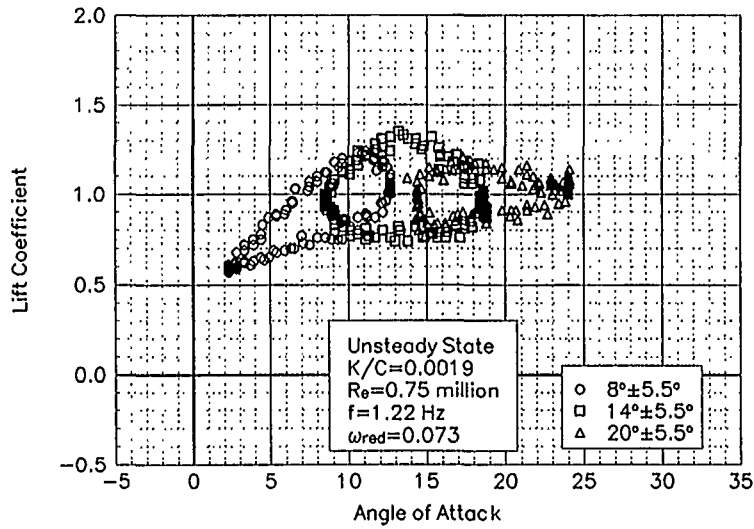
Figure C13. Lift coefficient vs α.

LS(1)-0421MOD
LEGR
Re = 0.75 Million
$\omega_{red} = 0.073$
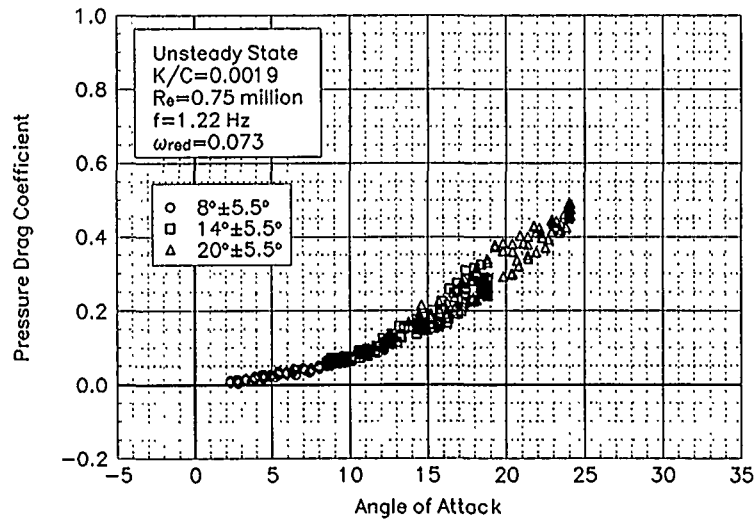
Figure C14. Pressure drag coefficient vs α.
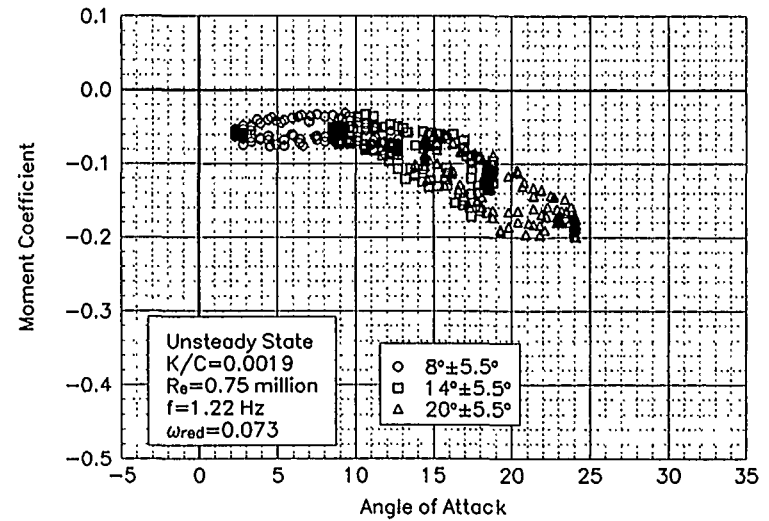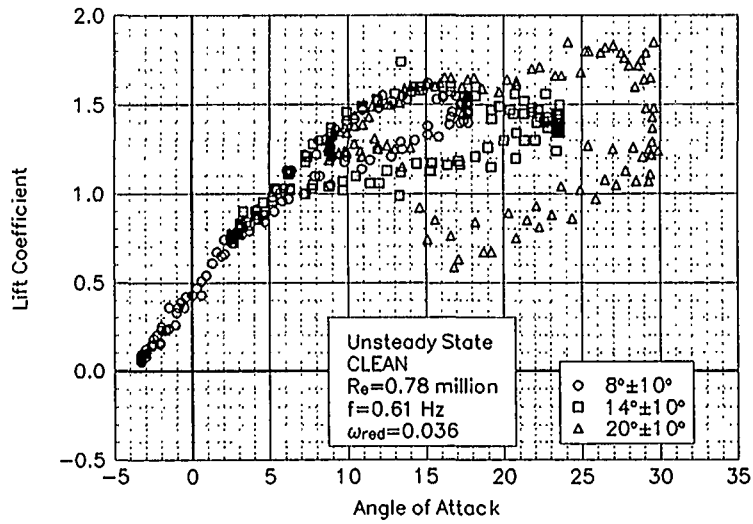

Figure C15. Moment coefficient vs α.

C-8
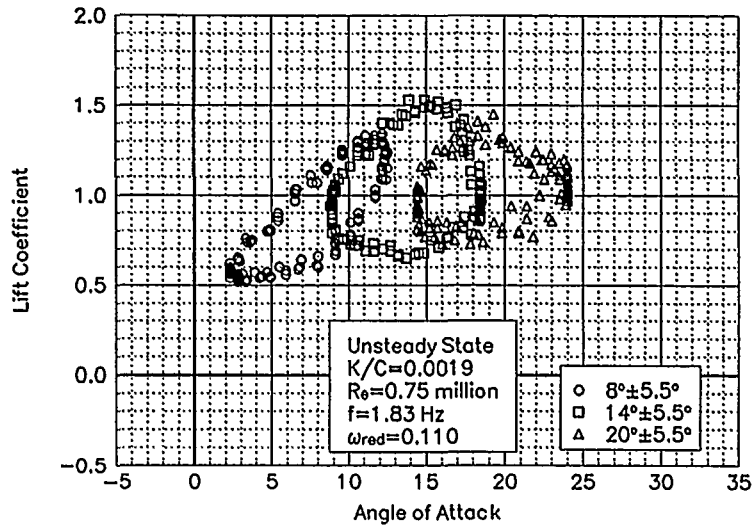
Figure C16. Lift coefficient vs α.

LS(1)-0421MOD
LEGR
Re = 0.75 Million
$\omega_{red} = 0.110$
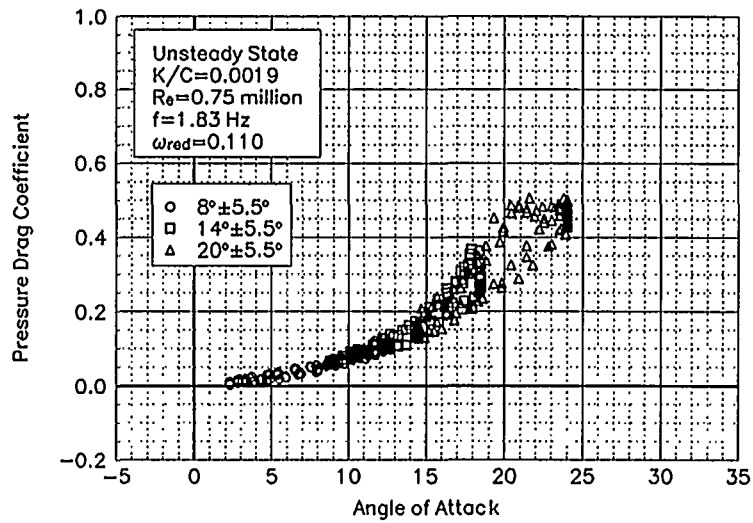
Figure C17. Pressure drag coefficient vs α.
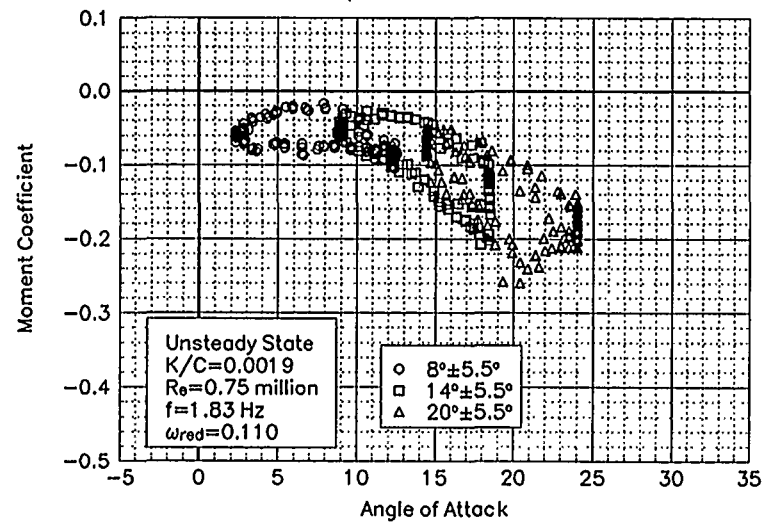
Figure C18. Moment coefficient vs α.

C-9

Unsteady Airfoil Characteristics

$\pm\,5^{\circ}$ Sine

Re = 1 Million
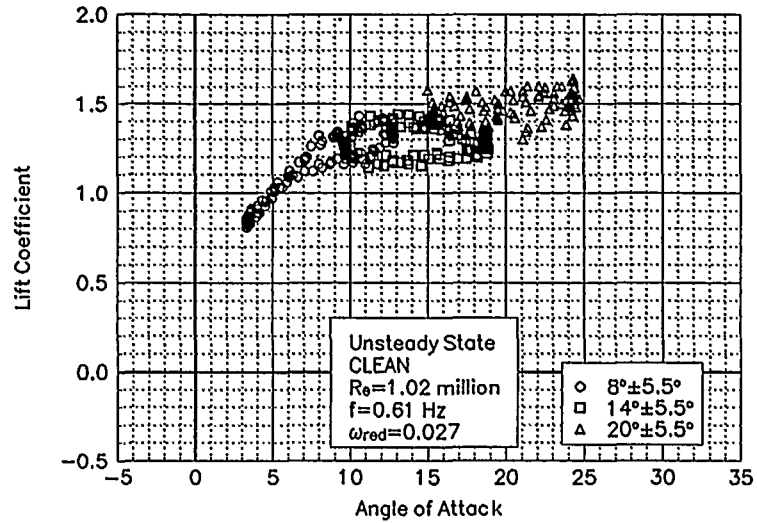
Figure C19. Lift coefficient vs α.

LS(1)-0421MOD
Clean
Re = 1 Million
$\omega_{red} = 0.027$
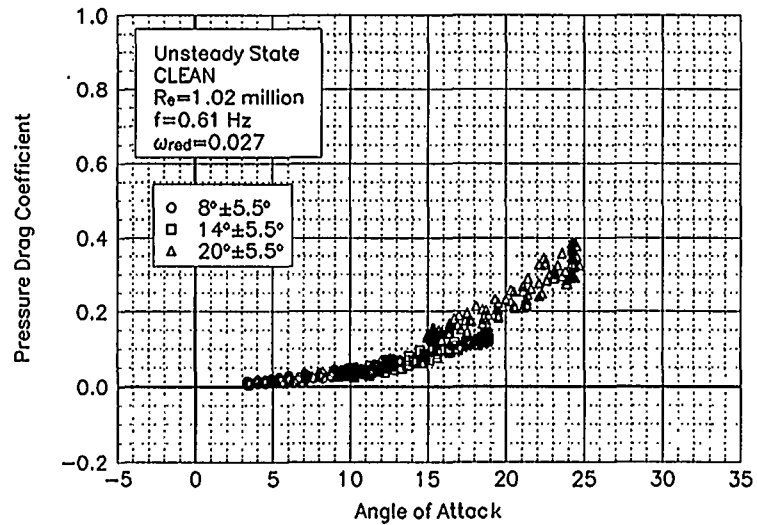
Figure C20. Pressure drag coefficient vs α.
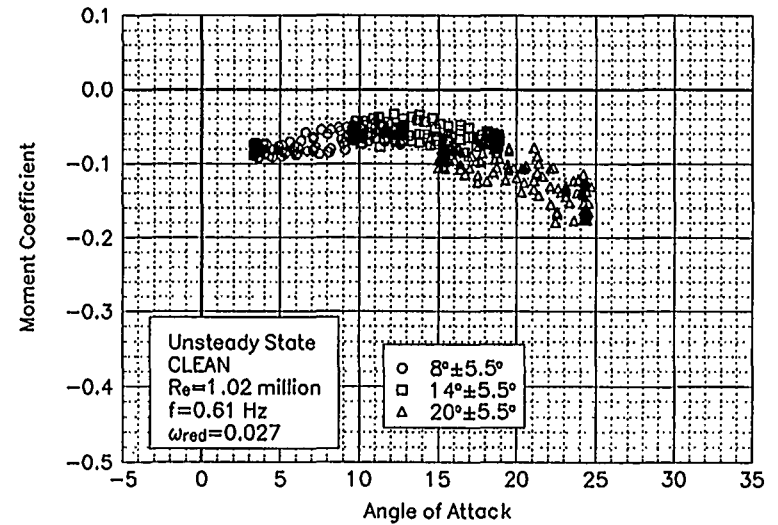
Figure C21. Moment coefficient vs α.
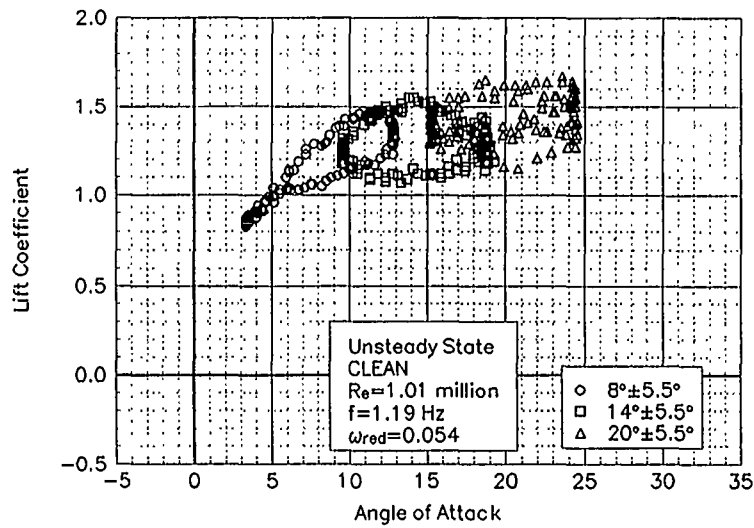
Figure C22. Lift coefficient vs α.

LS(1)-0421MOD
Clean
Re = 1 Million
$\omega_{red} = 0.054$
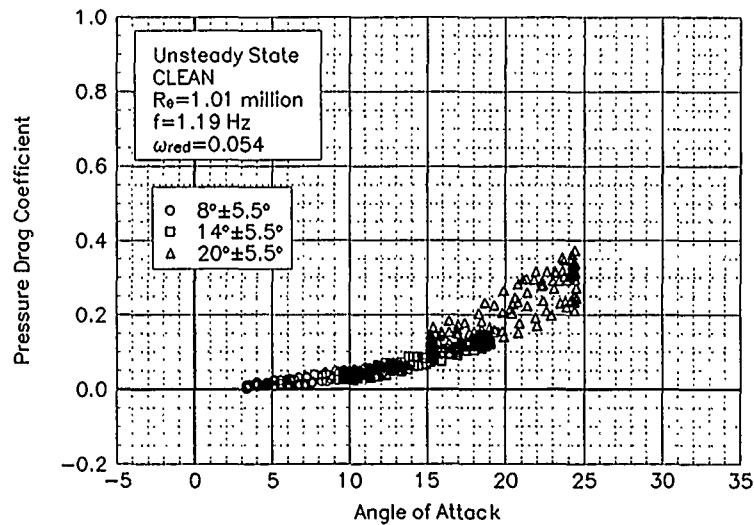
Figure C23. Pressure drag coefficient vs α.
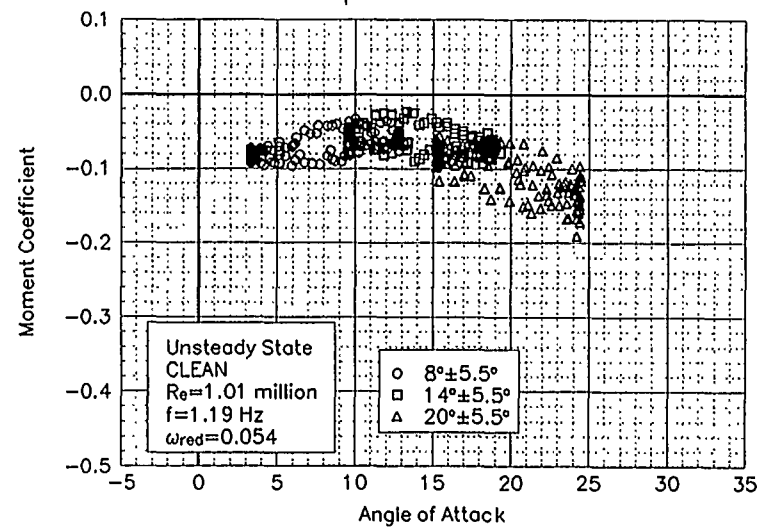
Figure C24. Moment coefficient vs α.
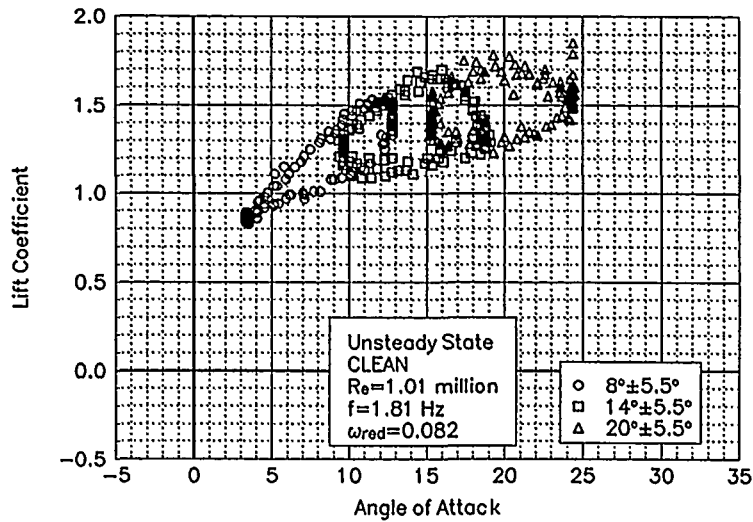
Figure C25. Lift coefficient vs α.

LS(1)-0421MOD
Clean
Re = 1 Million
$\omega_{red} = 0.082$
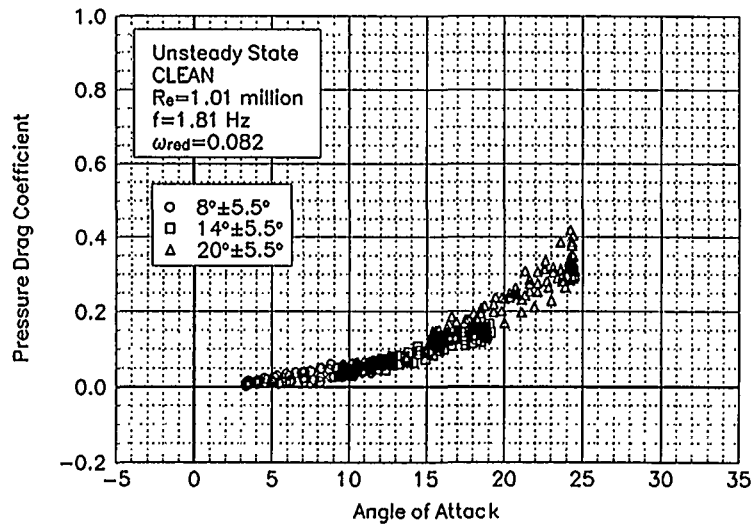
Figure C26. Pressure drag coefficient vs α.
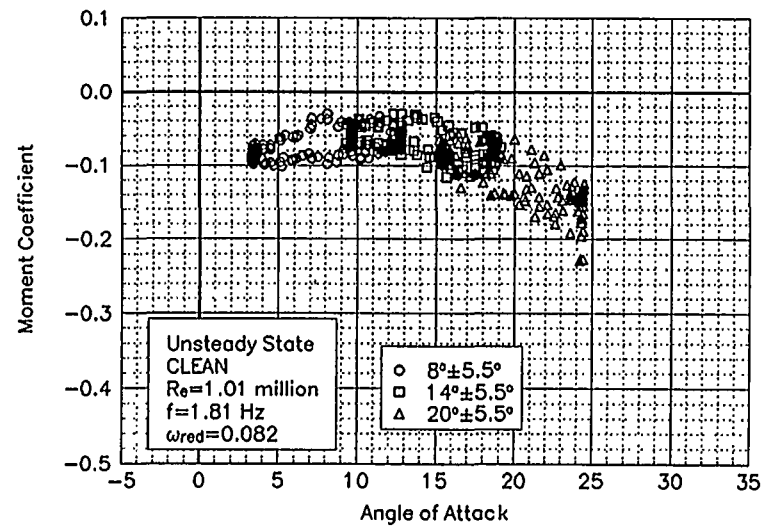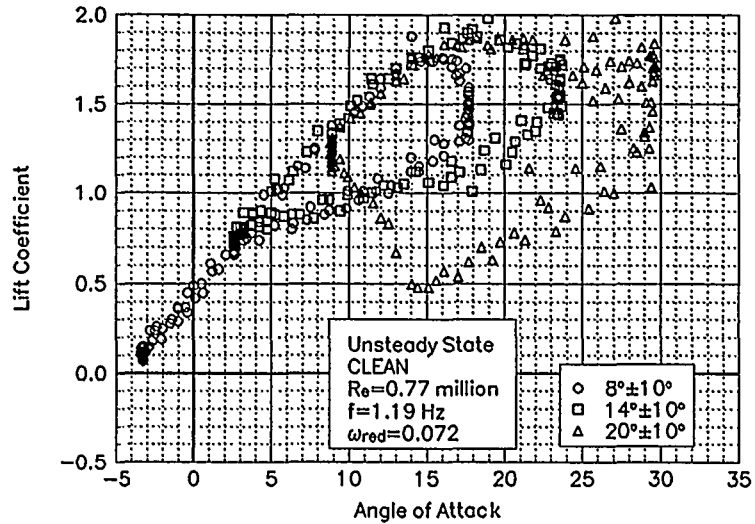

Figure C27. Moment coefficient vs α.

C-13
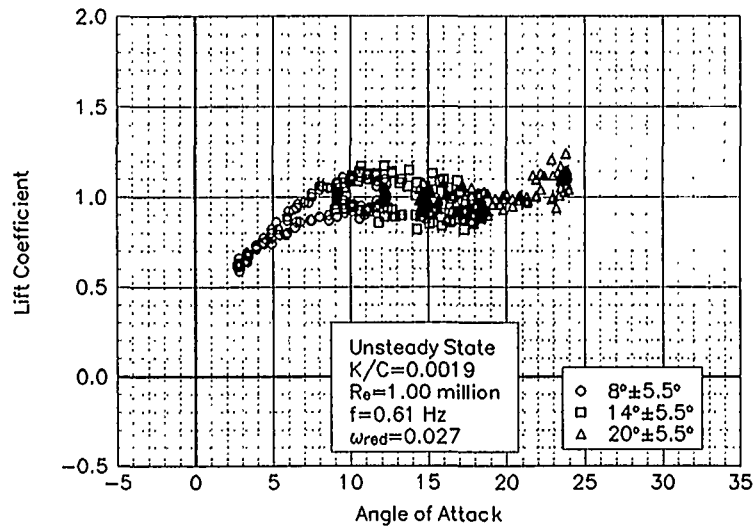
Figure C28. Lift coefficient vs α.

**LS(1)-0421MOD
LEGR
Re = 1 Million
$\omega_{red} = 0.027$**
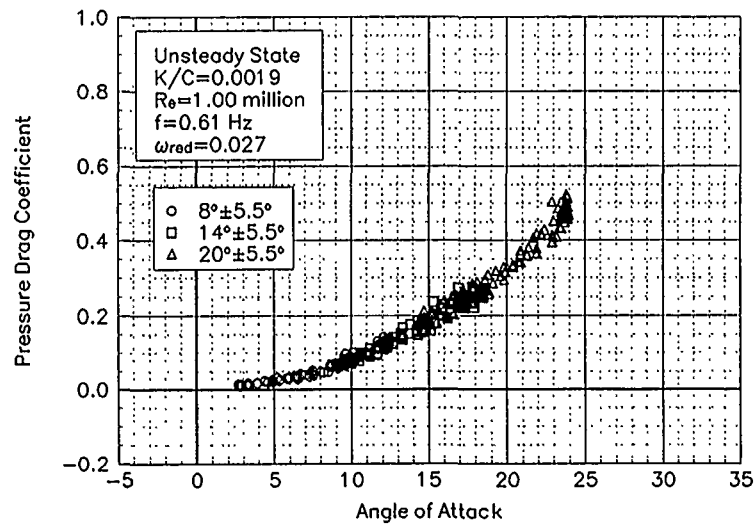
Figure C29. Pressure drag coefficient vs α.
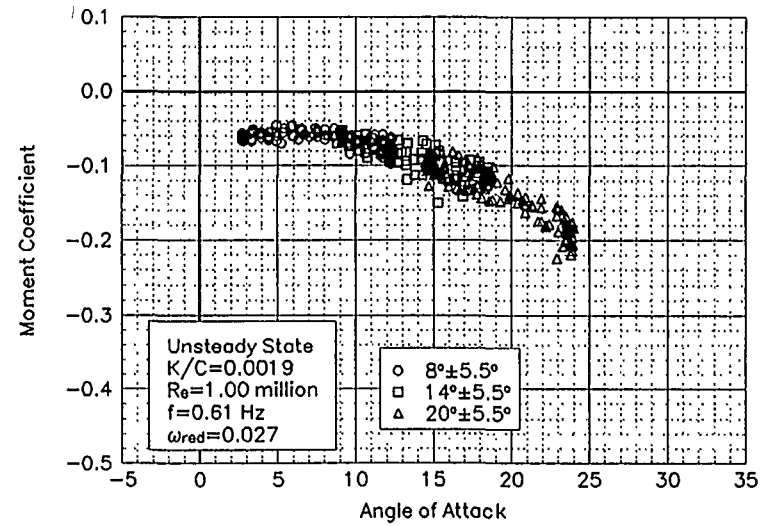
Figure C30. Moment coefficient vs α.

C-14
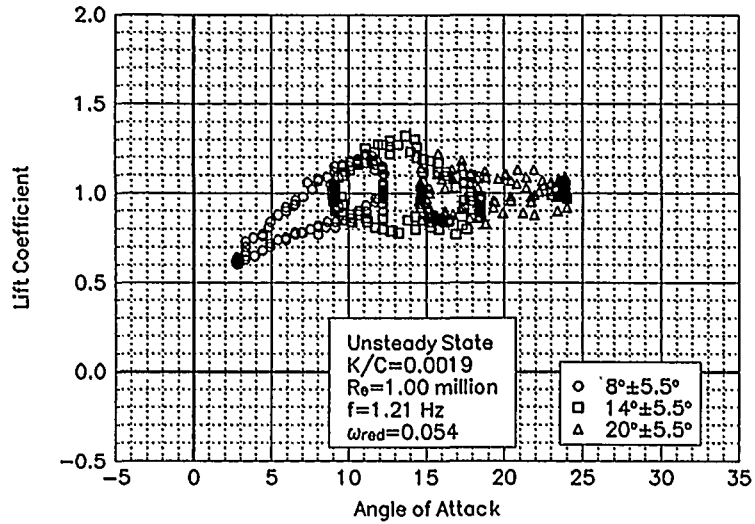
Figure C31. Lift coefficient vs α.

LS(1)-0421MOD
LEGR
Re = 1 Million
## $\omega_{red} = 0.054$
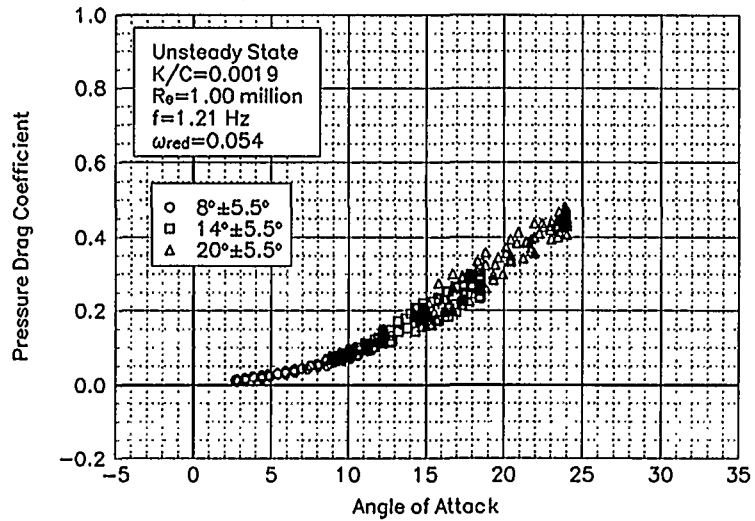
Figure C32. Pressure drag coefficient vs α.
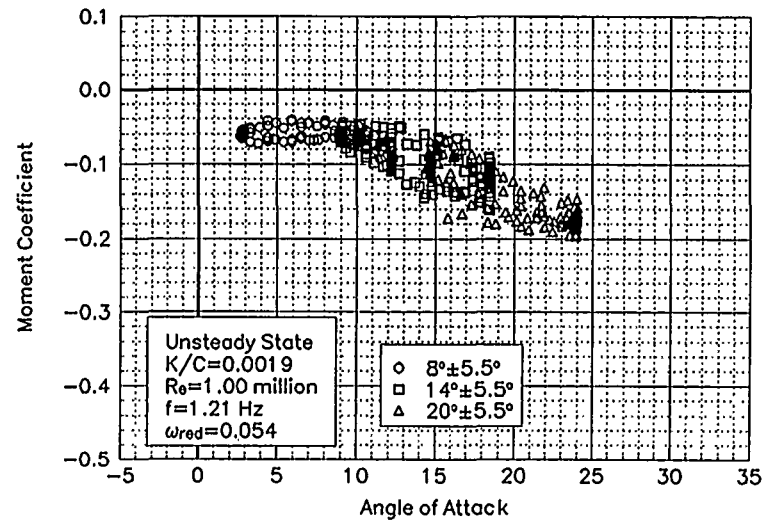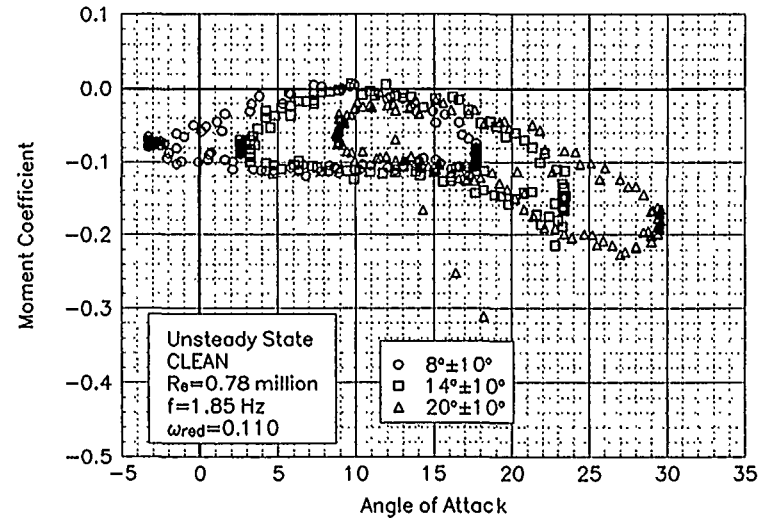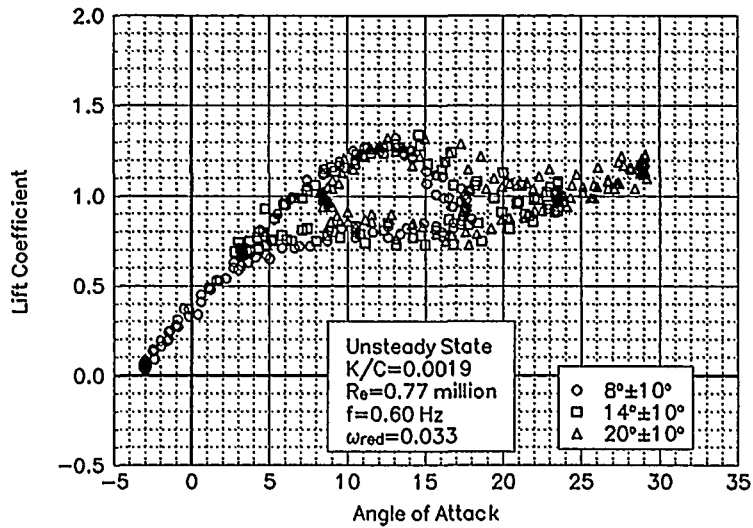

Figure C33. Moment coefficient vs α.
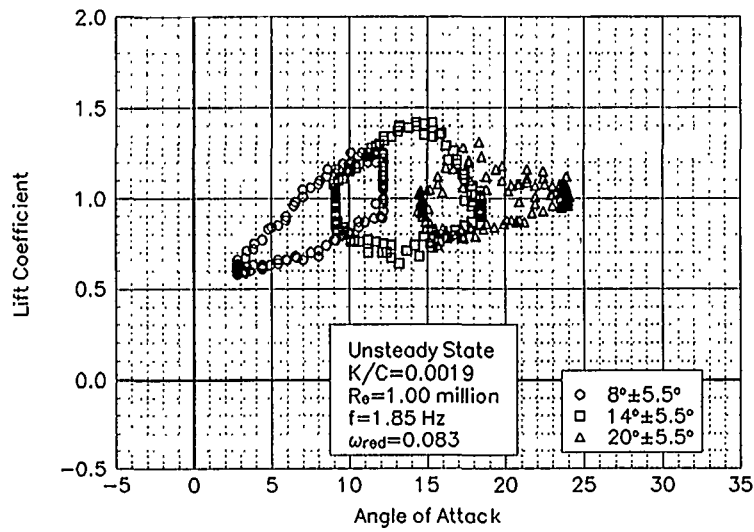
Figure C34. Lift coefficient vs α.

LS(1)-0421MOD
LEGR
Re = 1 Million
ω_{red} = 0.083
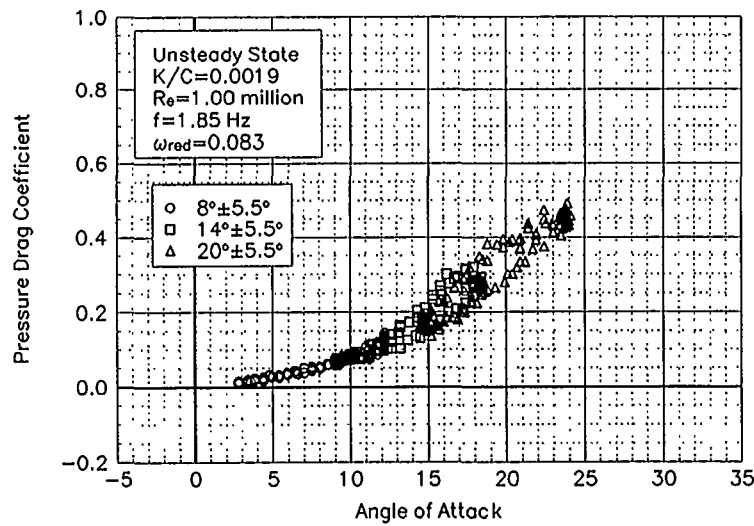
Figure C35. Pressure drag coefficient vs α.
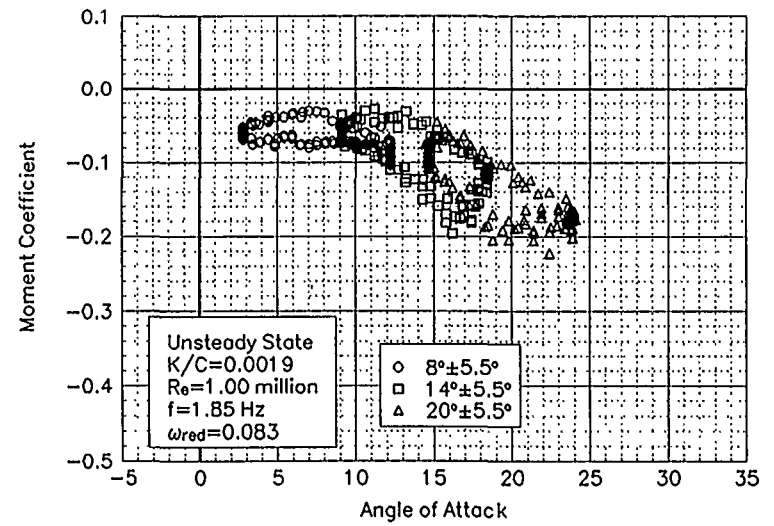
Figure C36. Moment coefficient vs α.

Unsteady Airfoil Characteristics

± 5° Sine

Re = 1.25 Million
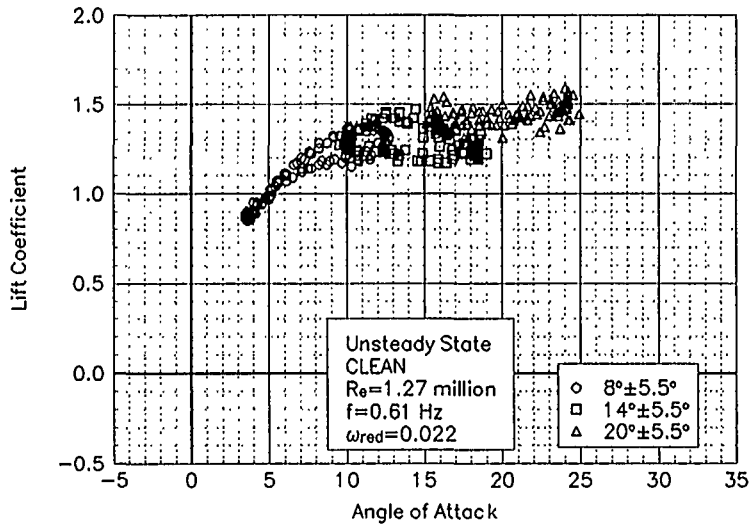
Figure C37. Lift coefficient vs α.

LS(1)-0421MOD
Clean
## Re = 1.25 Million
$\omega_{red} = 0.022$
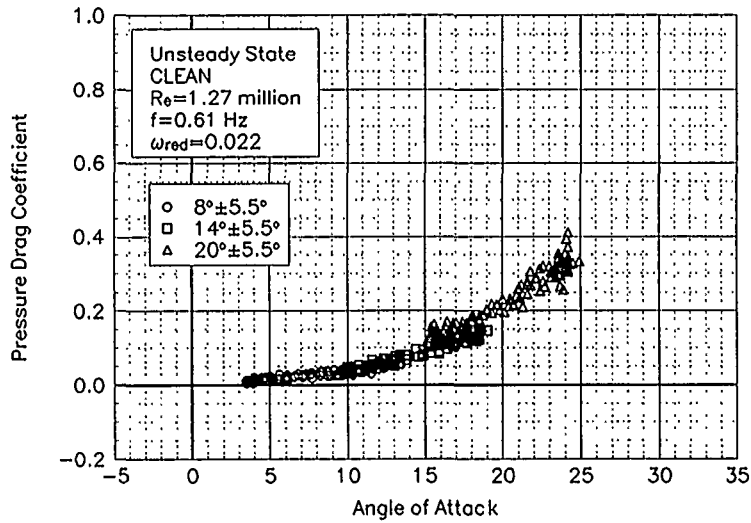
Figure C38. Pressure drag coefficient vs α.
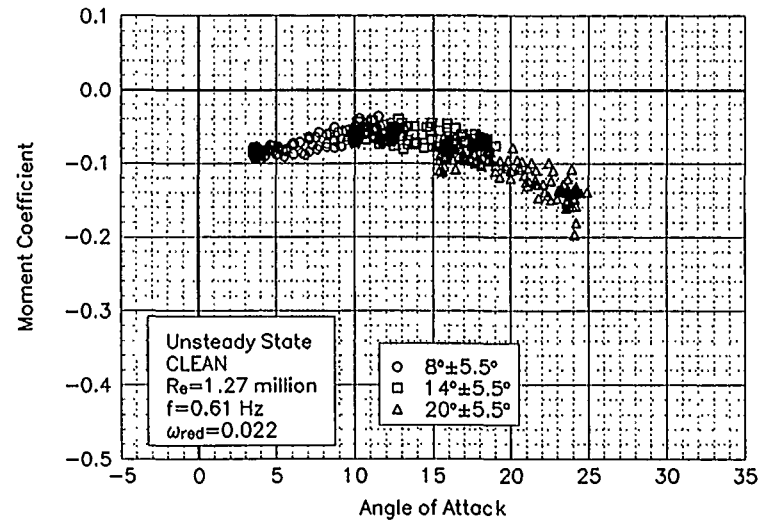
Figure C39. Moment coefficient vs α.
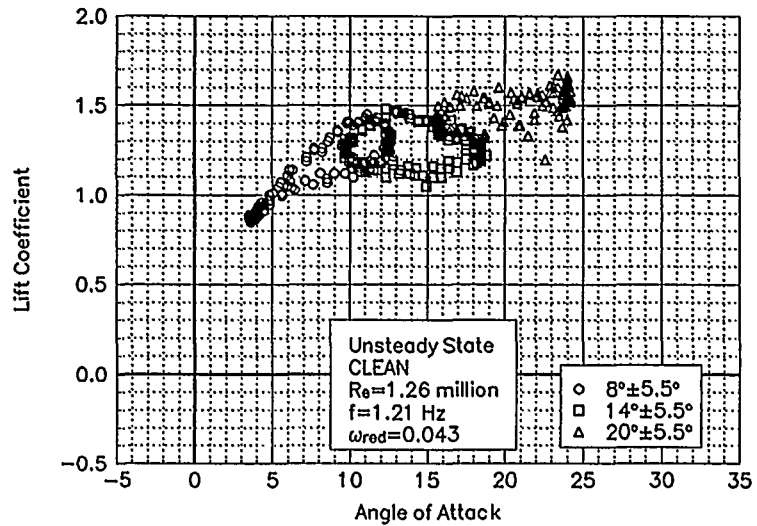
Figure C40. Lift coefficient vs α.

**LS(1)-0421MOD
Clean
Re = 1.25 Million
$\omega_{red} = 0.043$**
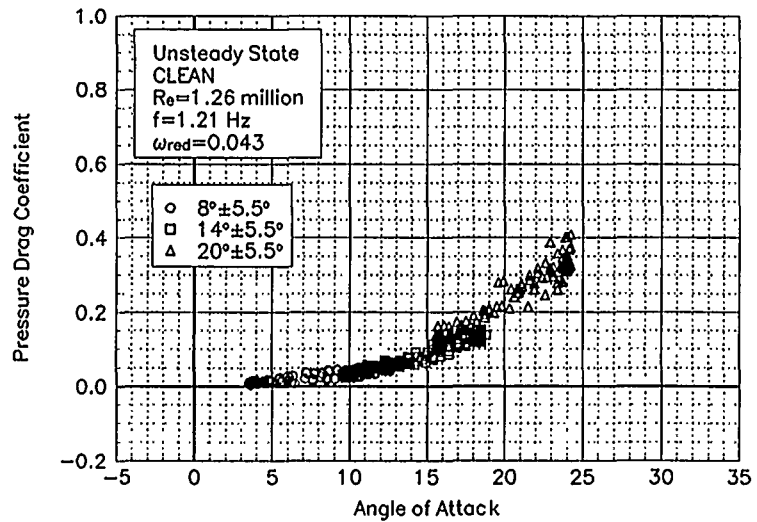
Figure C41. Pressure drag coefficient vs α.
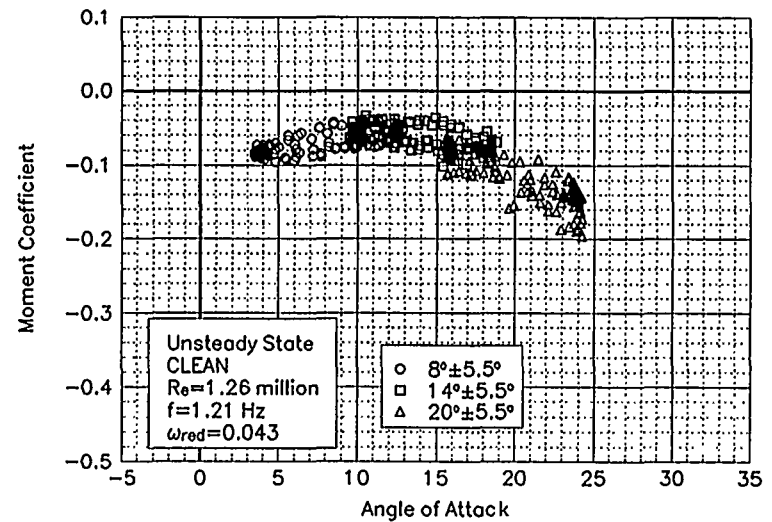
Figure C42. Moment coefficient vs α.

C-19
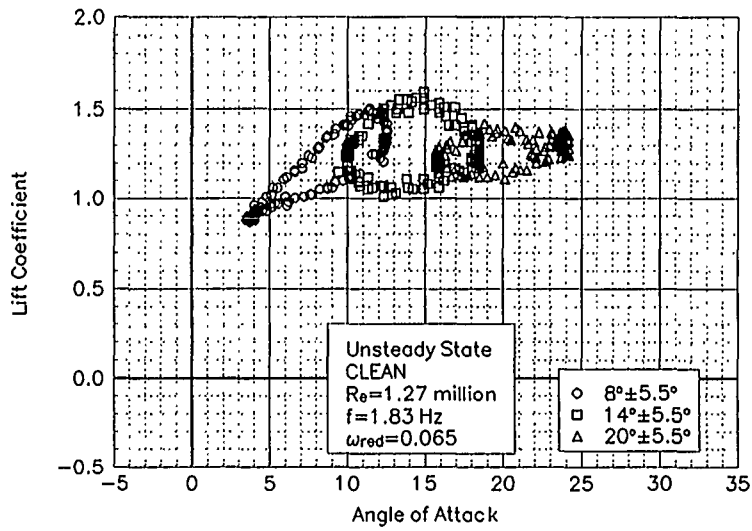
Figure C43. Lift coefficient vs α.

LS(1)-0421MOD
Clean
Re = 1.25 Million
$\omega_{red} = 0.065$
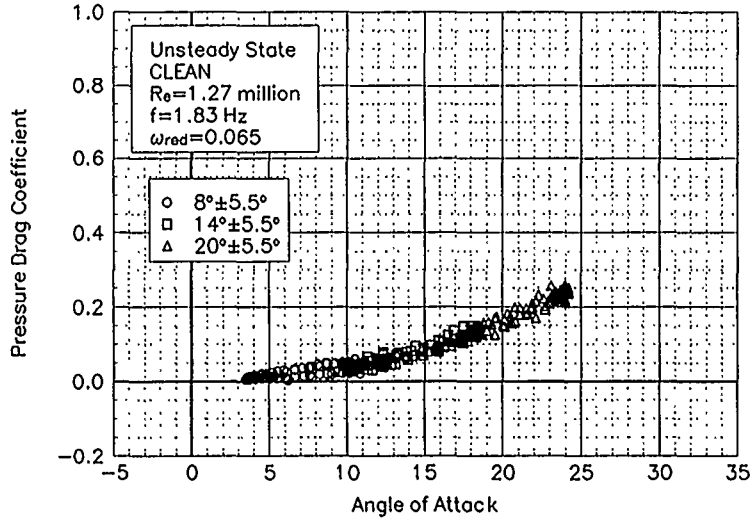
Figure C44. Pressure drag coefficient vs α.
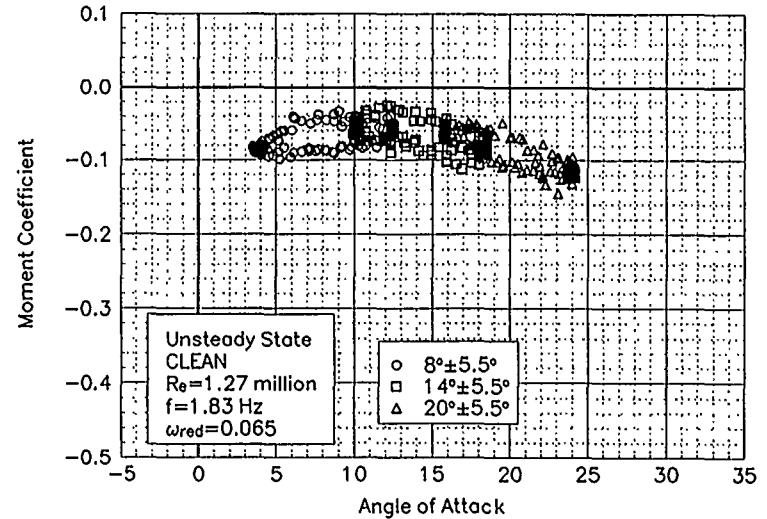
Figure C45. Moment coefficient vs α.
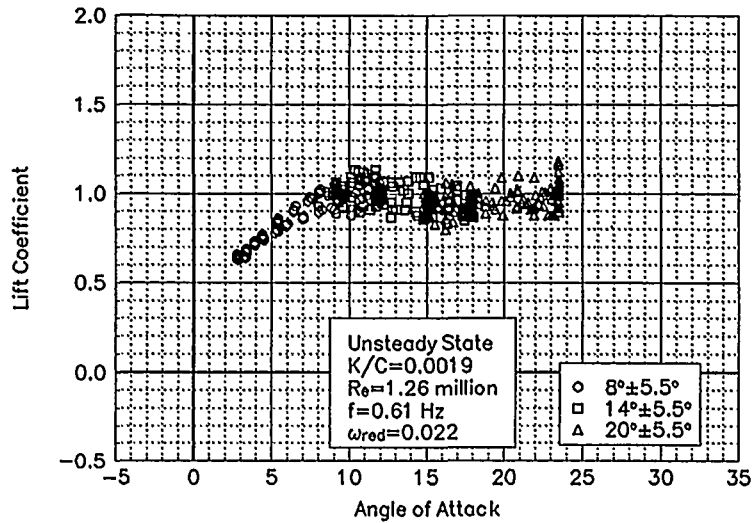
Figure C46. Lift coefficient vs α.
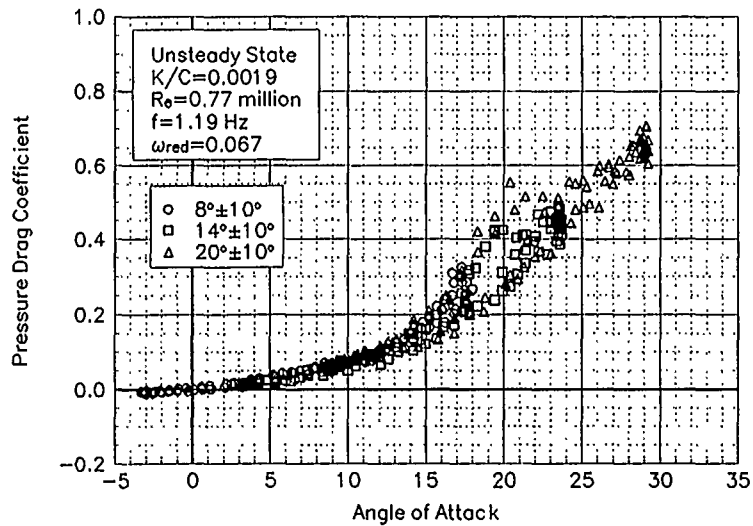
LS(1)-0421MOD
LEGR
Re = 1.25 Million
ω_{red} = 0.022
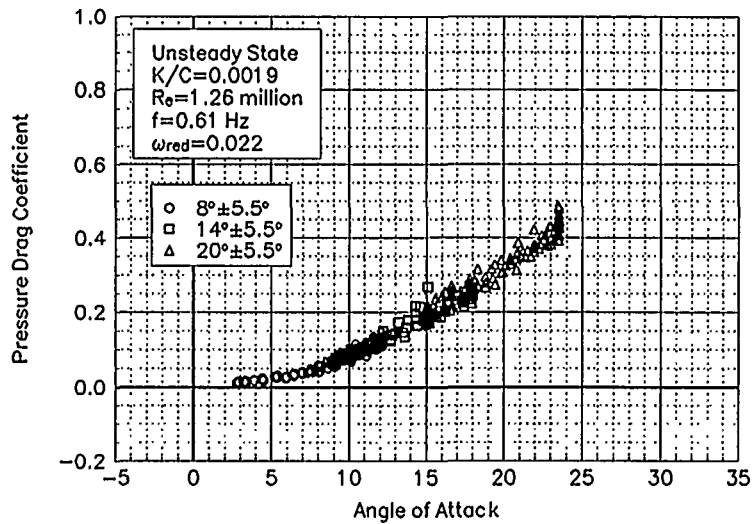
Figure C47. Pressure drag coefficient vs α.
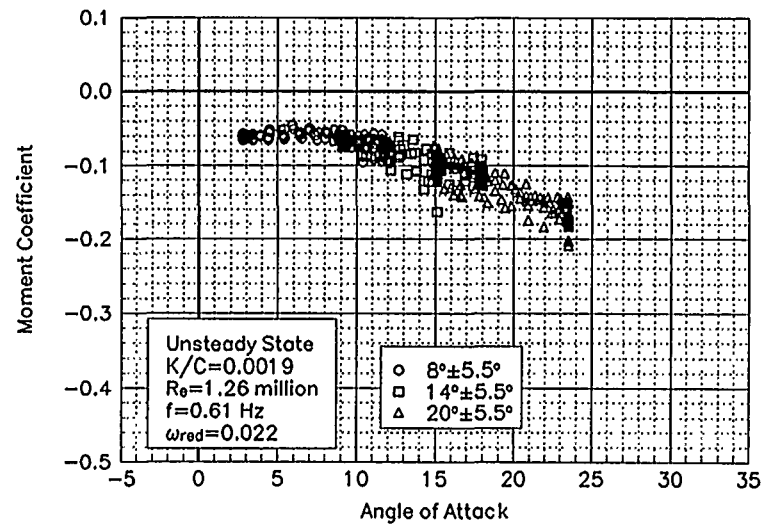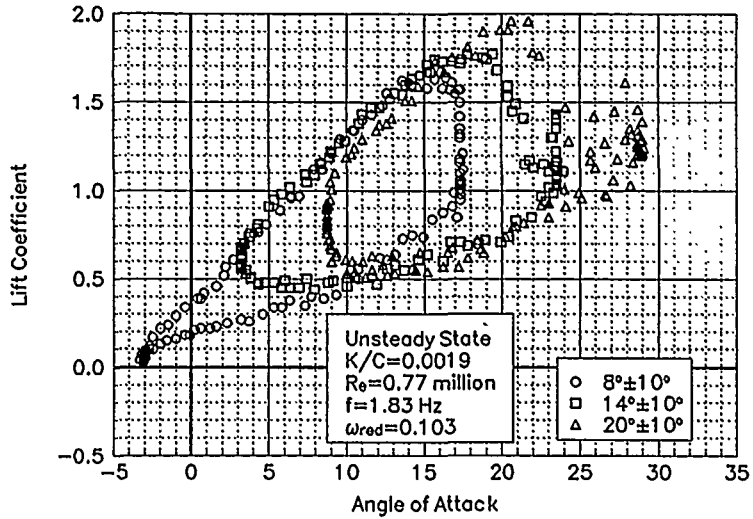

Figure C48. Moment coefficient vs α.

C-21
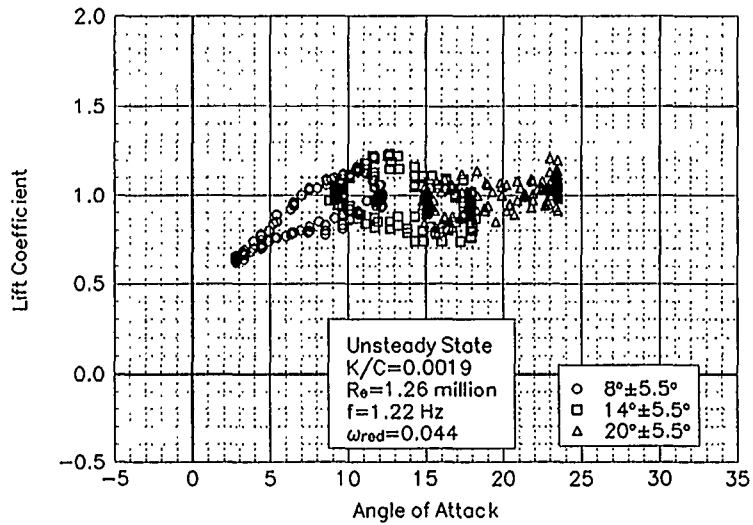
Figure C49. Lift coefficient vs α.

LS(1)-0421MOD
LEGR
Re = 1.25 Million
ω_{red} = 0.044
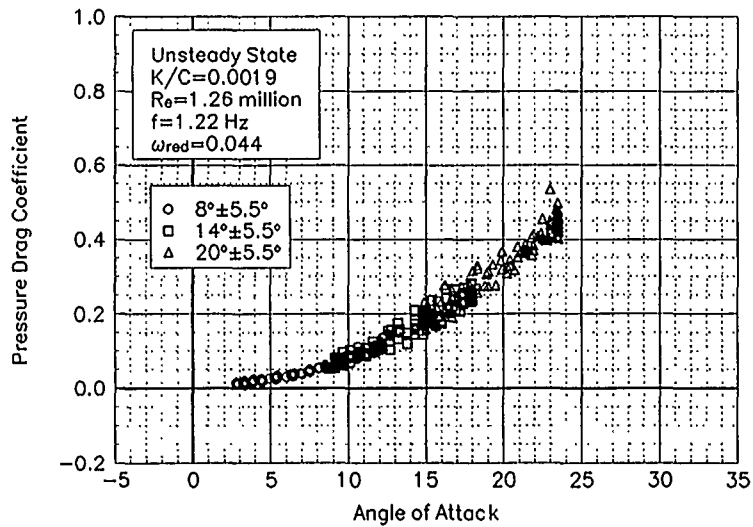
Figure C50. Pressure drag coefficient vs α.
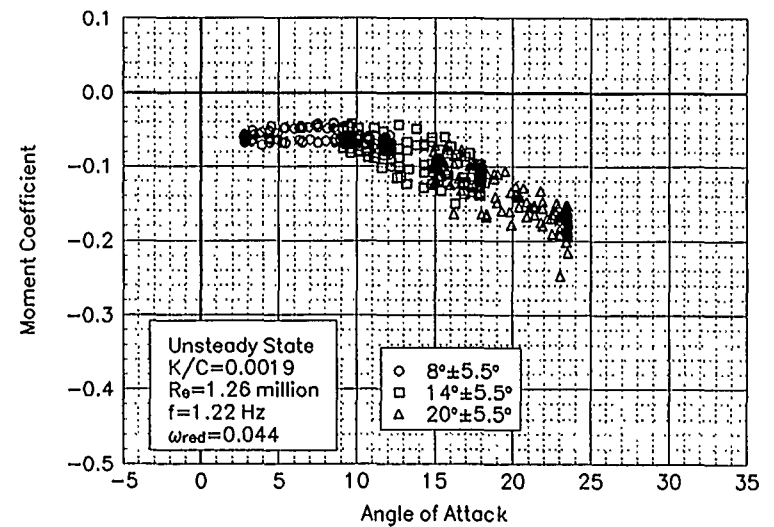
Figure C51. Moment coefficient vs α.
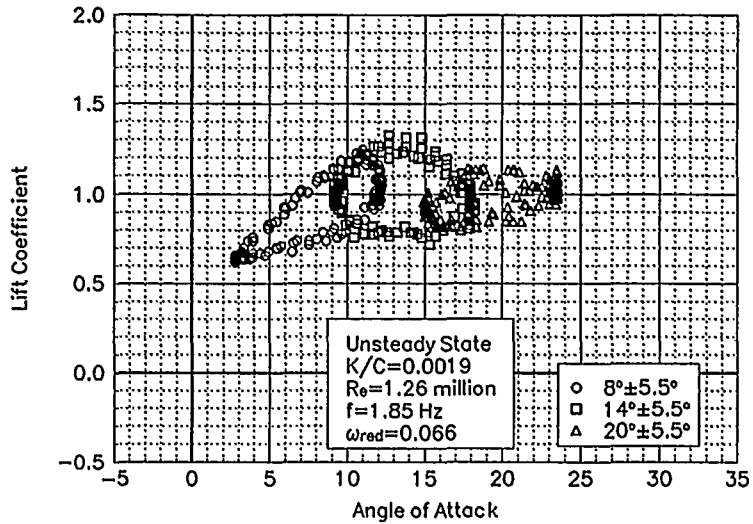
Figure C52. Lift coefficient vs α.

**LS(1)-0421MOD
LEGR
Re = 1.25 Million
ω_{red} = 0.066**
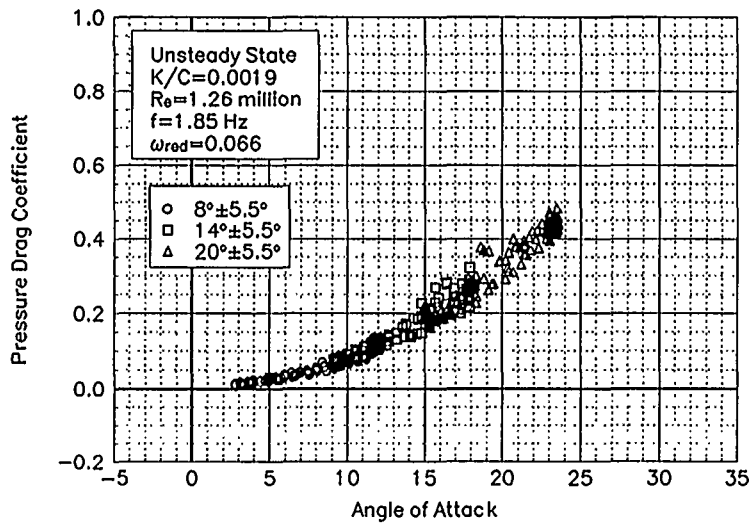
Figure C53. Pressure drag coefficient vs α.
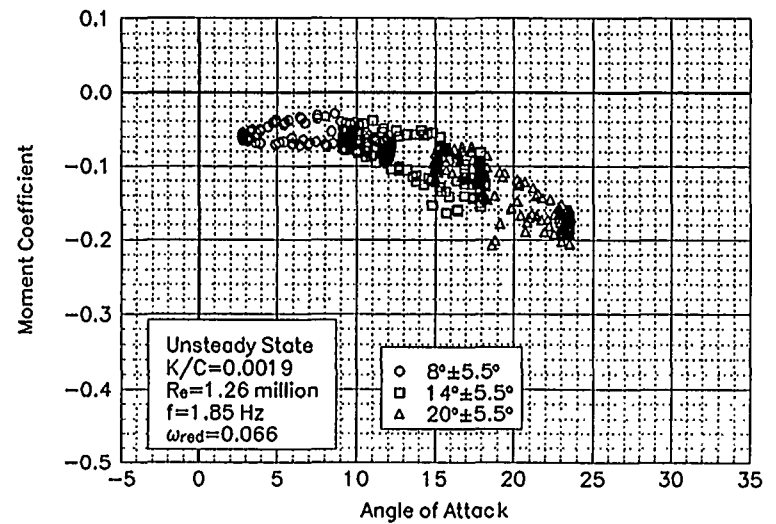
Figure C54. Moment coefficient vs α.

C-23

Unsteady Airfoil Characteristics

$\pm\,5^{\circ}$ Sine

Re $=$ 1.5 Million
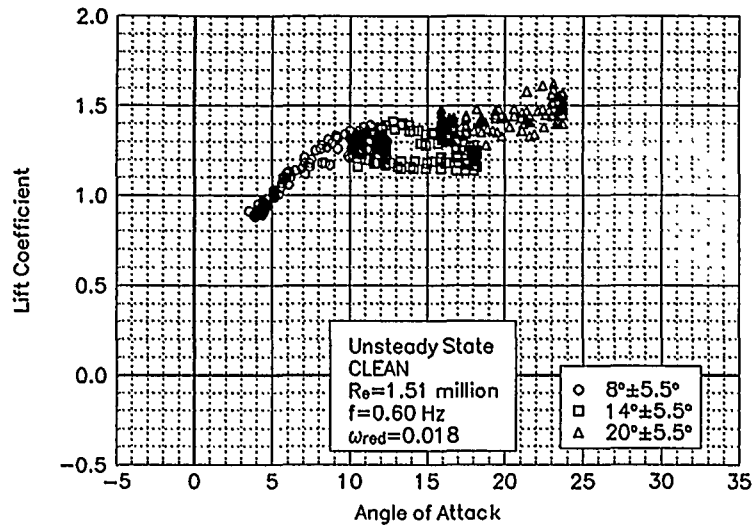
Figure C55. Lift coefficient vs α.

**LS(1)-0421MOD
Clean
Re = 1.5 Million
$\omega_{red} = 0.018$**
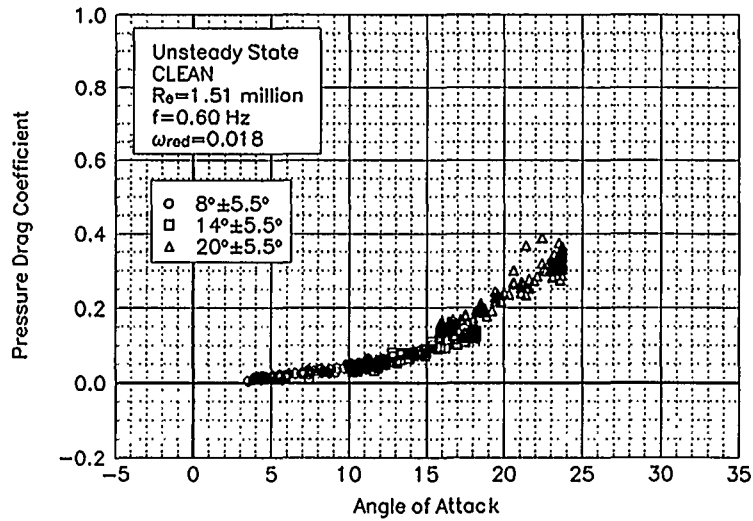
Figure C56. Pressure drag coefficient vs α.
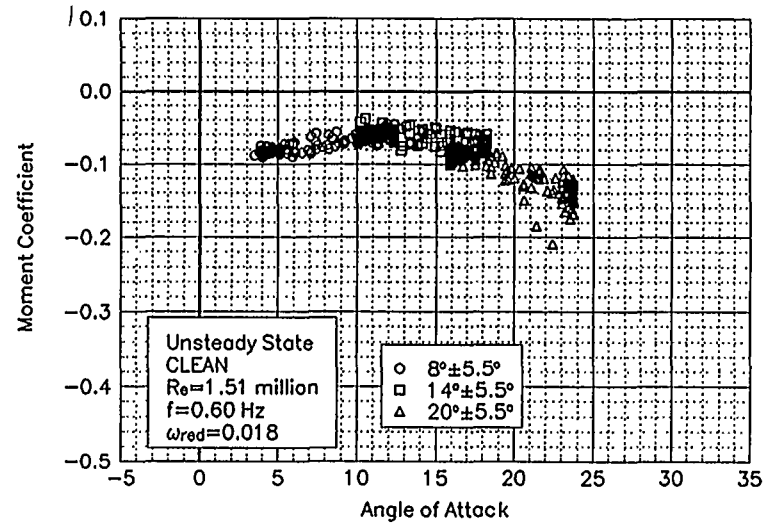
Figure C57. Moment coefficient vs α.
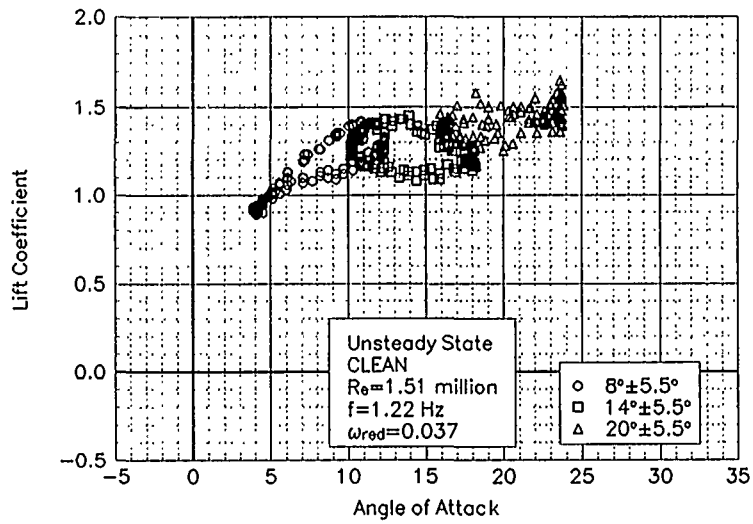
Figure C58. Lift coefficient vs α.

LS(1)-0421MOD
Clean
Re = 1.5 Million
$\omega_{red} = 0.037$
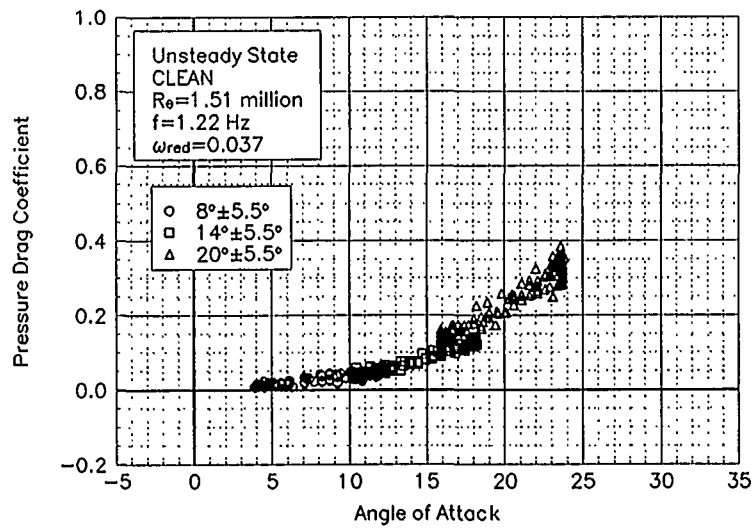
Figure C59. Pressure drag coefficient vs α.
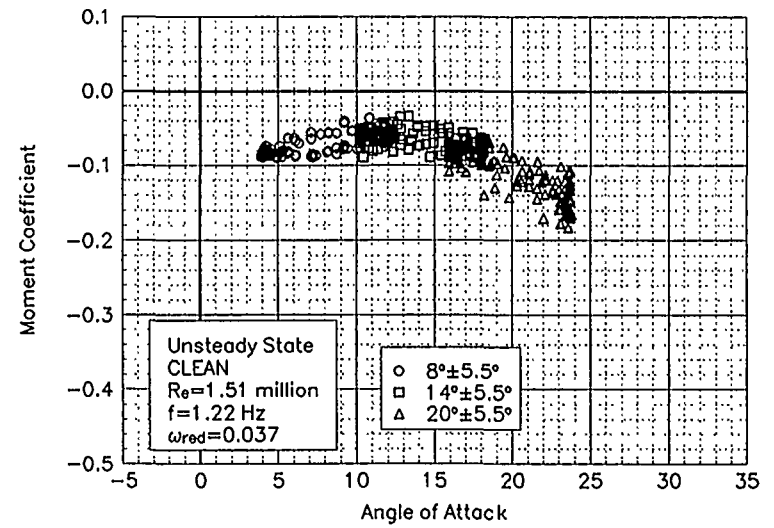
Figure C60. Moment coefficient vs α.

C-26
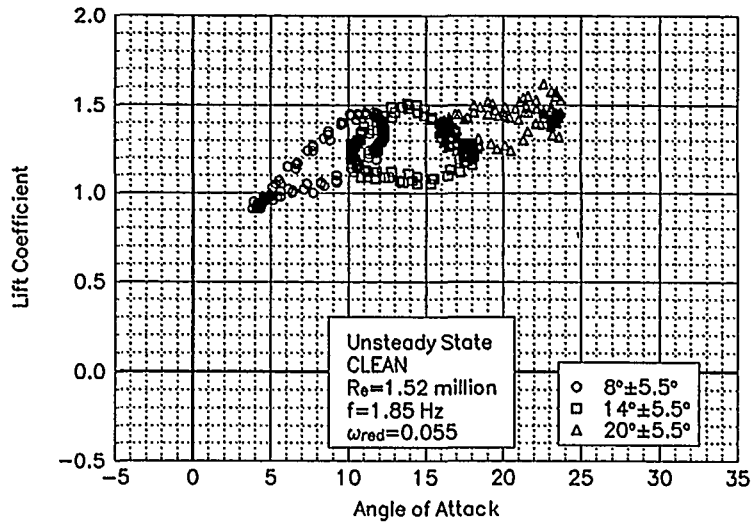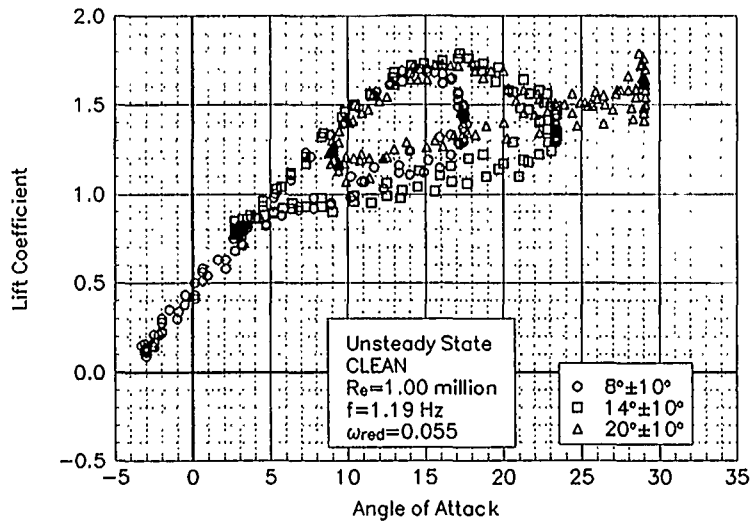
Figure C61. Lift coefficient vs α.

LS(1)-0421MOD
Clean
Re = 1.5 Million
$\omega_{red} = 0.055$
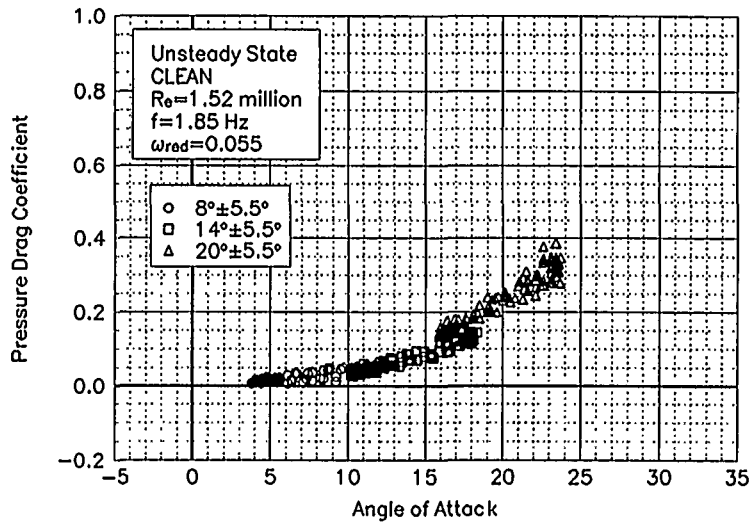
Figure C62. Pressure drag coefficient vs α.
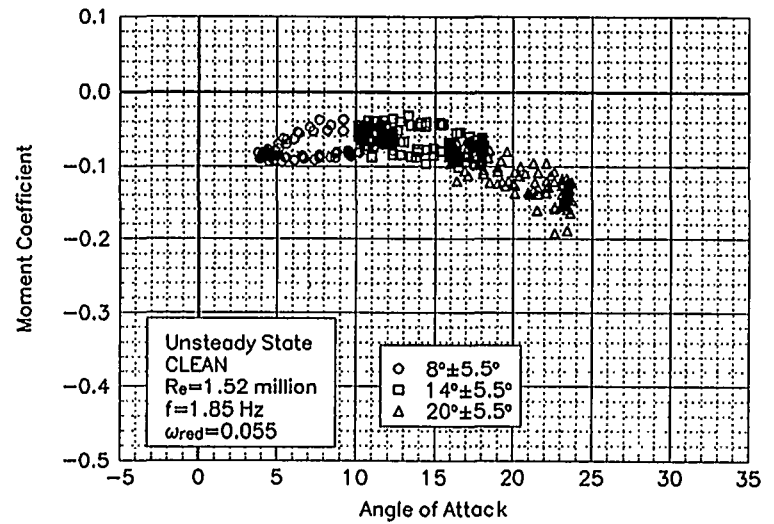
Figure C63. Moment coefficient vs α.

C-27
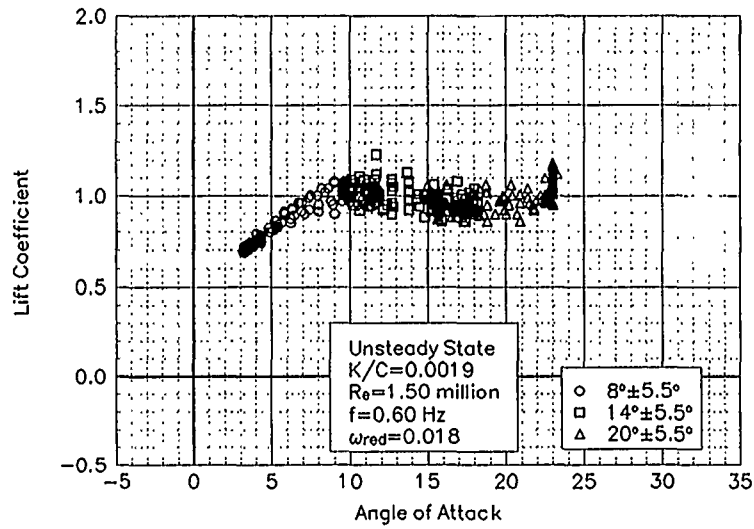
Figure C64. Lift coefficient vs a.

LS(1)-0421MOD
LEGR
**Re = 1.5 Million**
$\omega_{red} = 0.018$
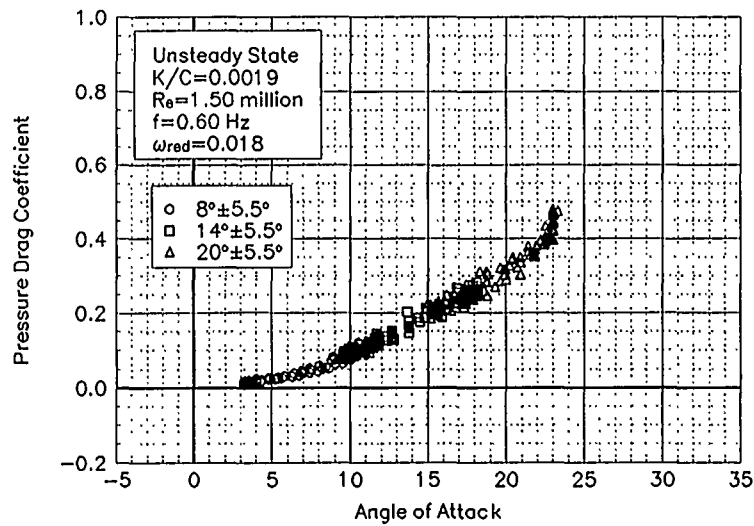
Figure C65. Pressure drag coefficient vs a.
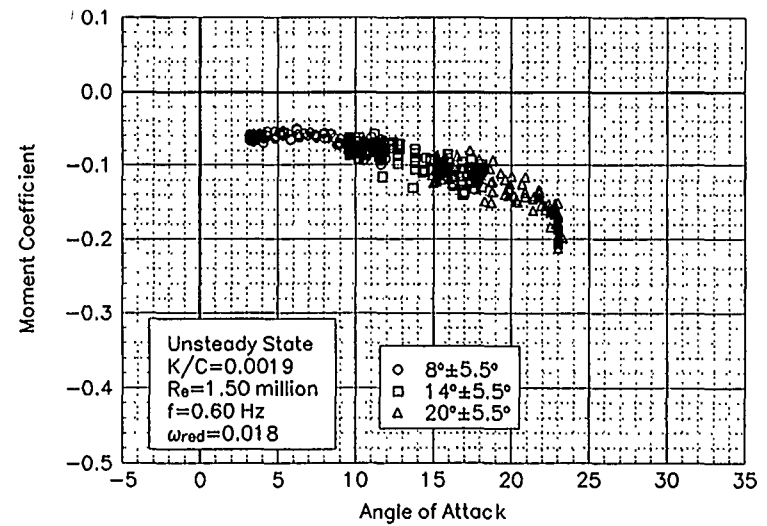
Figure C66. Moment coefficient vs a.
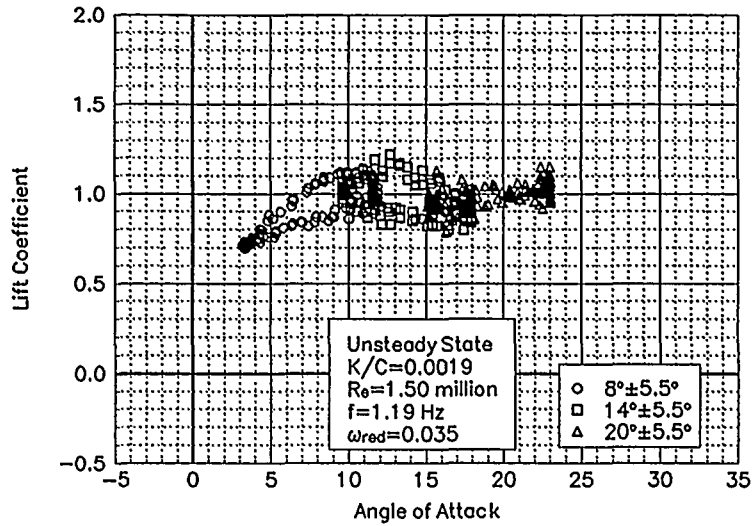
Figure C67. Lift coefficient vs α.

LS(1)-0421MOD
LEGR
Re = 1.5 Million
ω_{red} = 0.035
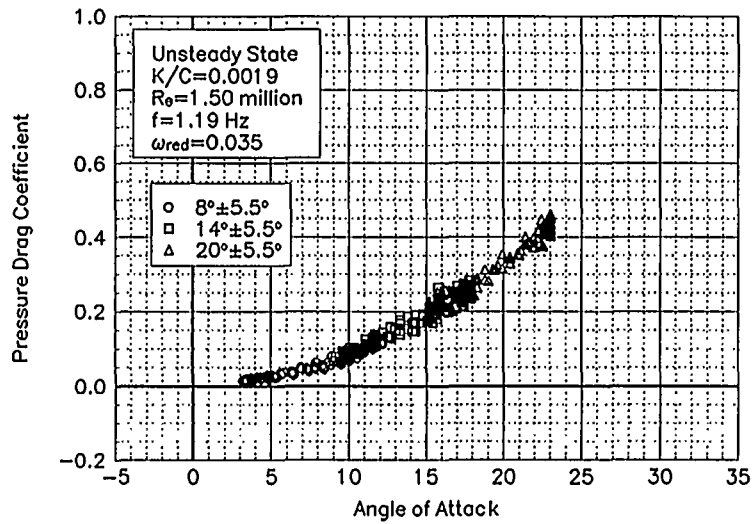
Figure C68. Pressure drag coefficient vs α.
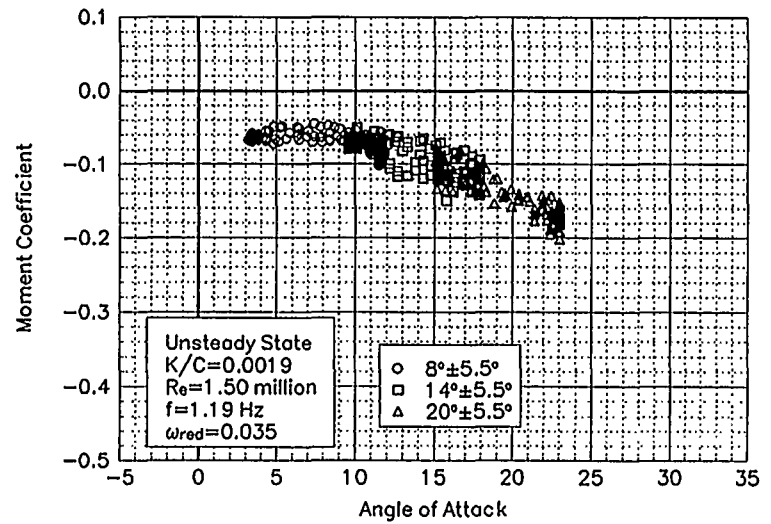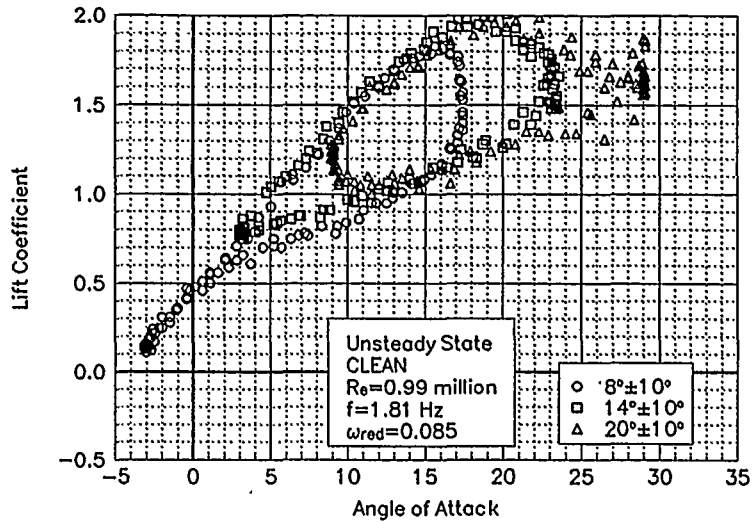

Figure C69. Moment coefficient vs α.

C-29
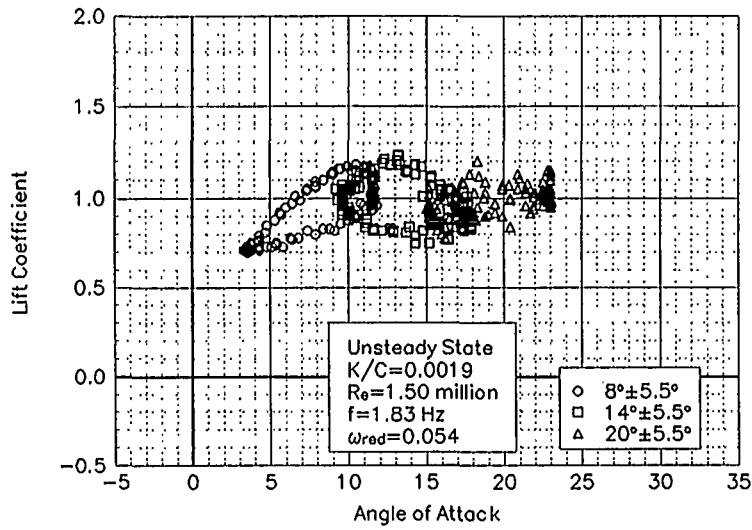
Figure C70. Lift coefficient vs a.

LS(1)-0421MOD
LEGR
Re = 1.5 Million
$\omega_{red} = 0.054$
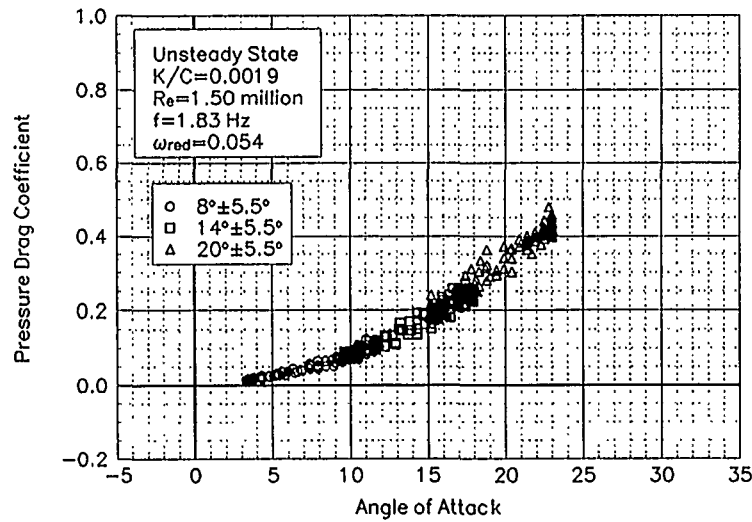
Figure C71. Pressure drag coefficient vs a.
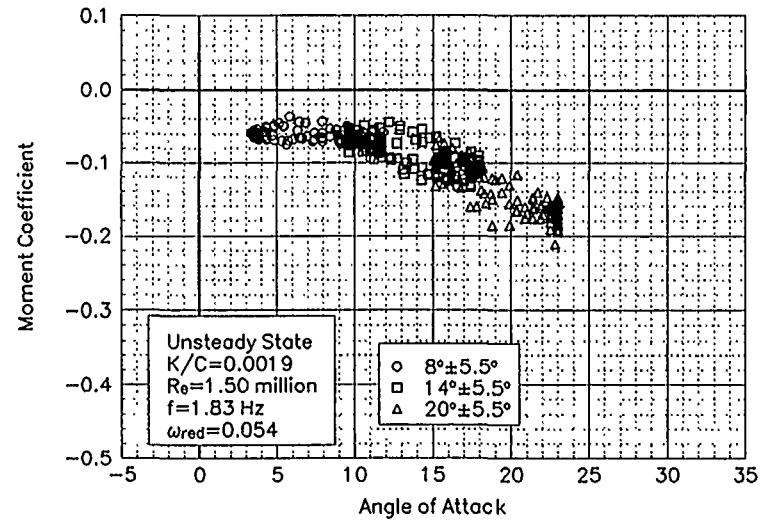
Figure C72. Moment coefficient vs a.

Unsteady Airfoil Characteristics

± 10° Sine

Re = 0.75 Million

Figure C73. Lift coefficient vs α.

LS(1)-0421MOD
Clean
Re = 0.75 Million
$\omega_{red} = 0.036$
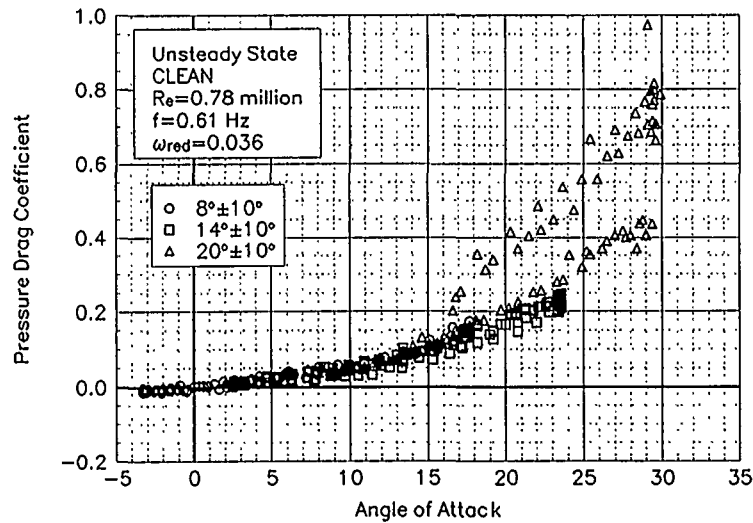
Figure C74. Pressure drag coefficient vs α.
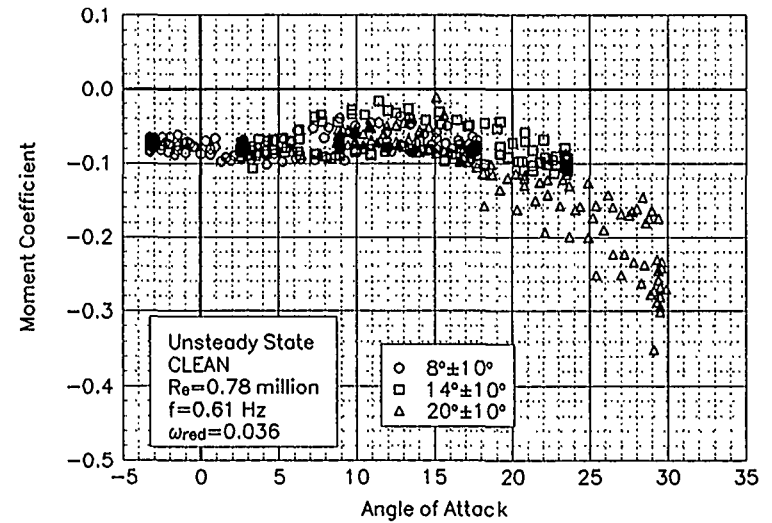
Figure C75. Moment coefficient vs α.

Figure C76. Lift coefficient vs α.

LS(1)-0421MOD
Clean
Re = 0.75 Million
$\omega_{red} = 0.072$
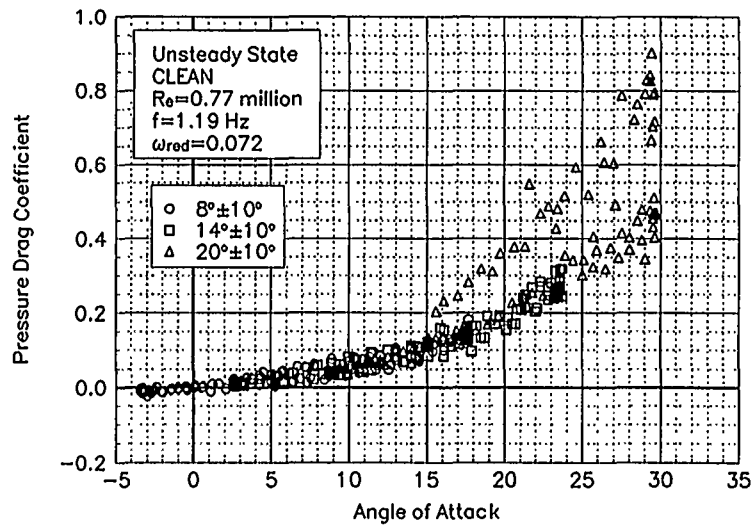
Figure C77. Pressure drag coefficient vs α.
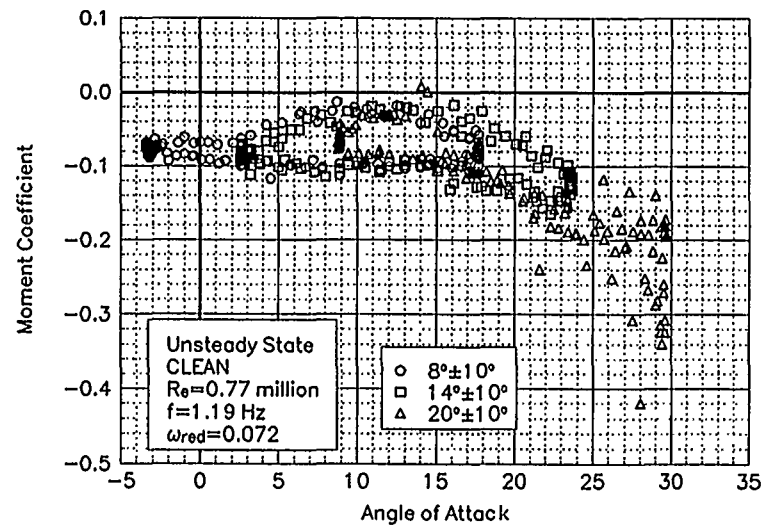
Figure C78. Moment coefficient vs α.

C-33
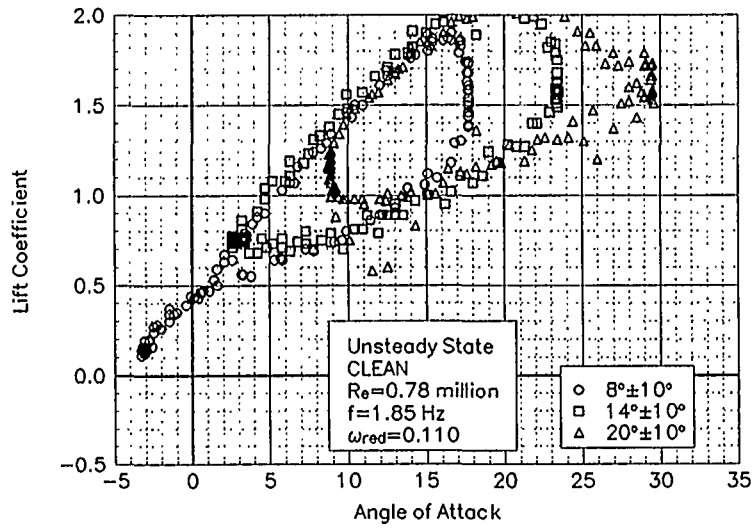
Figure C79. Lift coefficient vs α.

**LS(1)-0421MOD
Clean
Re = 0.75 Million
ω_{red} = 0.110**
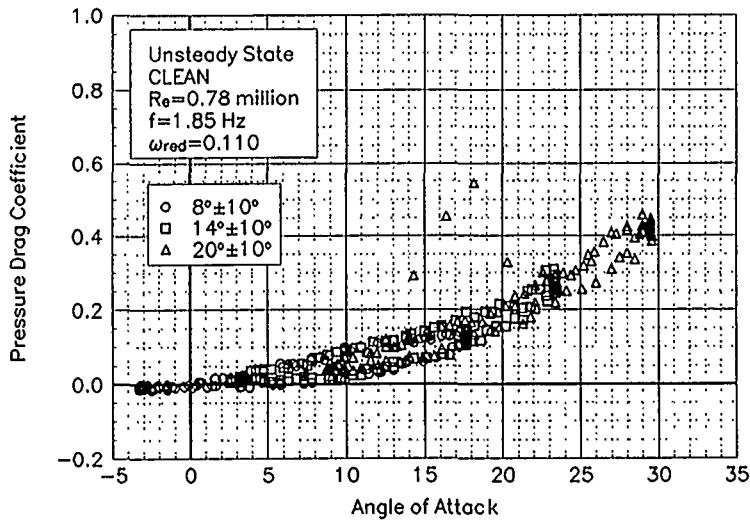
Figure C80. Pressure drag coefficient vs α.

Figure C81. Moment coefficient vs α.

Figure C82. Lift coefficient vs α.

LS(1)-0421MOD
LEGR
Re = 0.75 Million
$\omega_{red} = 0.033$
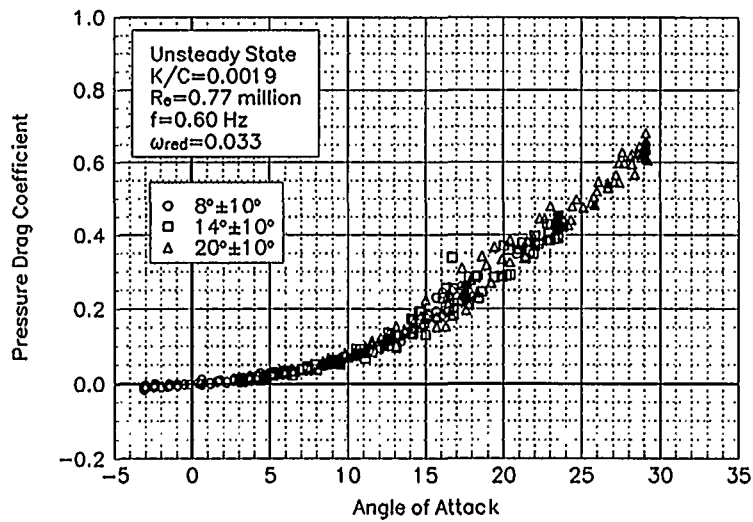
Figure C83. Pressure drag coefficient vs α.
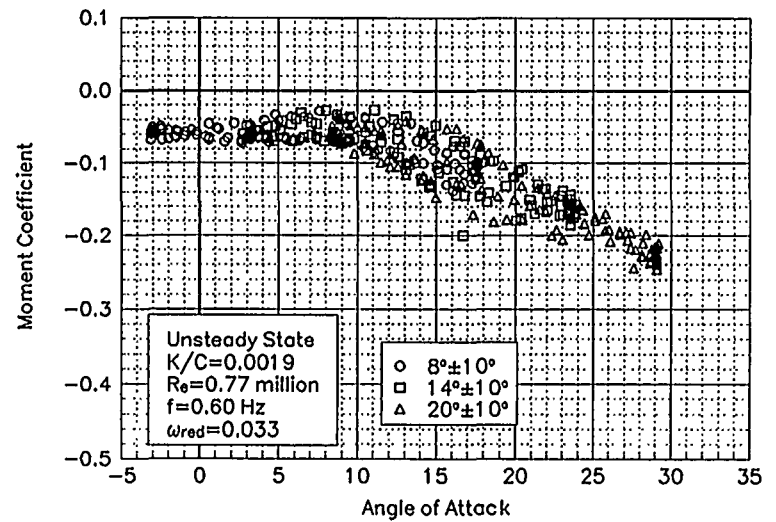
Figure C84. Moment coefficient vs α.
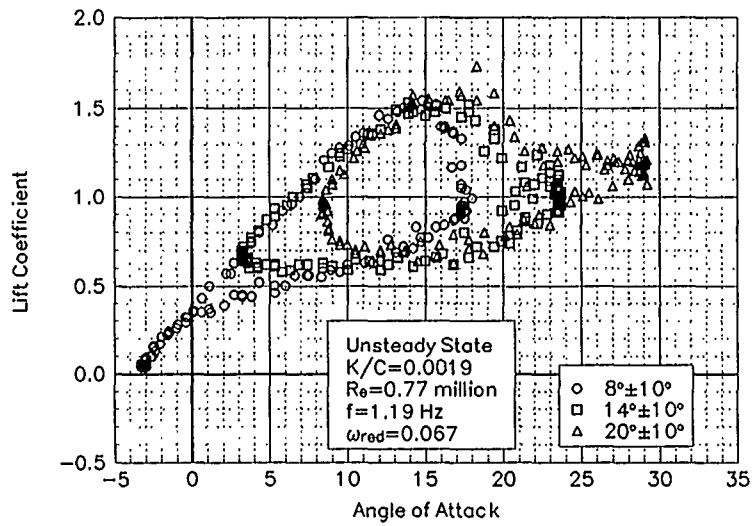
Figure C85. Lift coefficient vs α.

**LS(1)-0421MOD
LEGR
Re = 0.75 Million
ω_{red} = 0.067**

Figure C86. Pressure drag coefficient vs α.
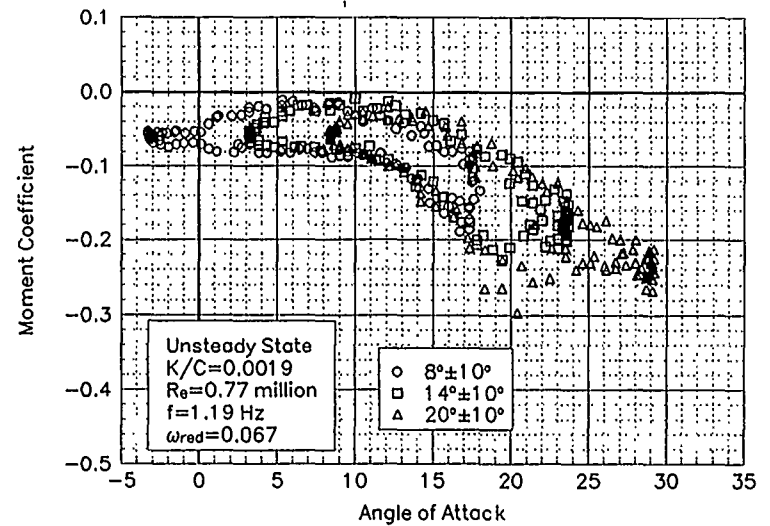
Figure C87. Moment coefficient vs α.

Figure C88. Lift coefficient vs α.

LS(1)-0421MOD
LEGR
Re = 0.75 Million
ω_{red} = 0.103
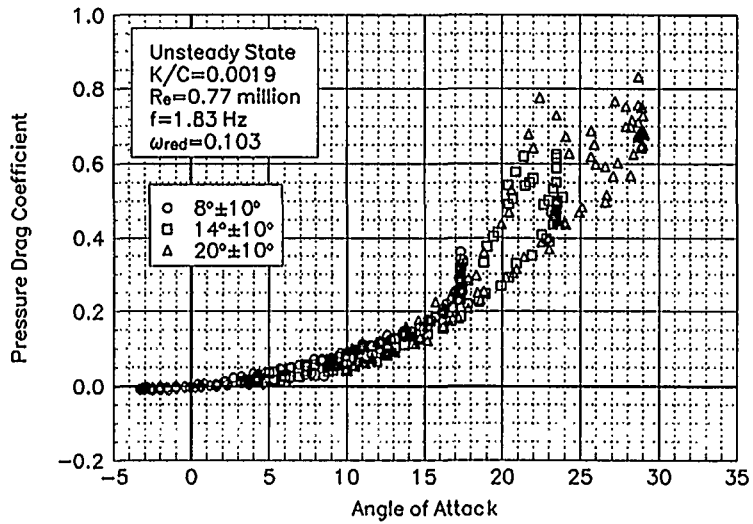
Figure C89. Pressure drag coefficient vs α.
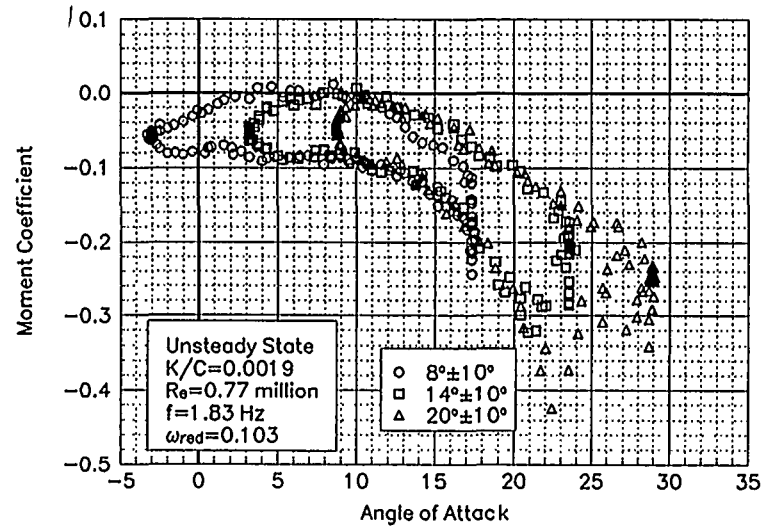
Figure C90. Moment coefficient vs α.

Unsteady Airfoil Characteristics

± 10° Sine

Re = 1 Million
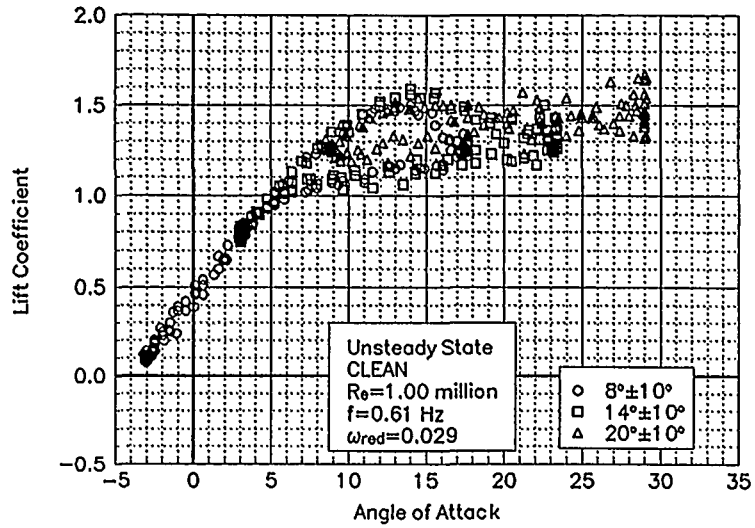
Figure C91. Lift coefficient vs α.

LS(1)-0421MOD
Clean
Re = 1 Million
$\omega_{red} = 0.029$
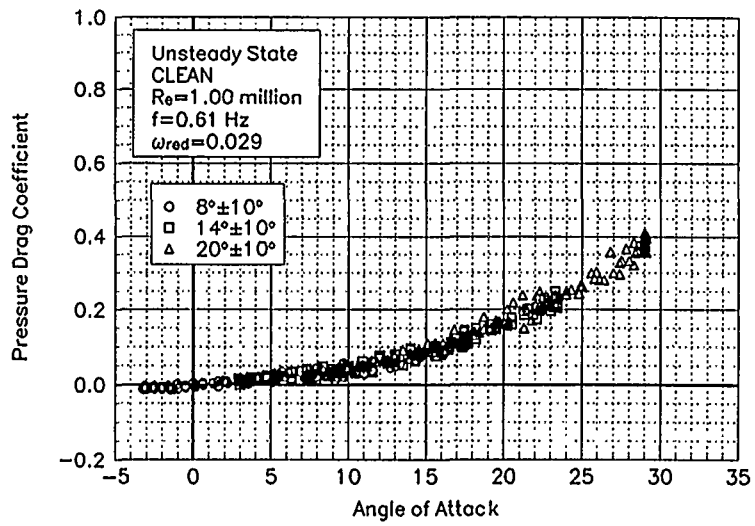
Figure C92. Pressure drag coefficient vs α.
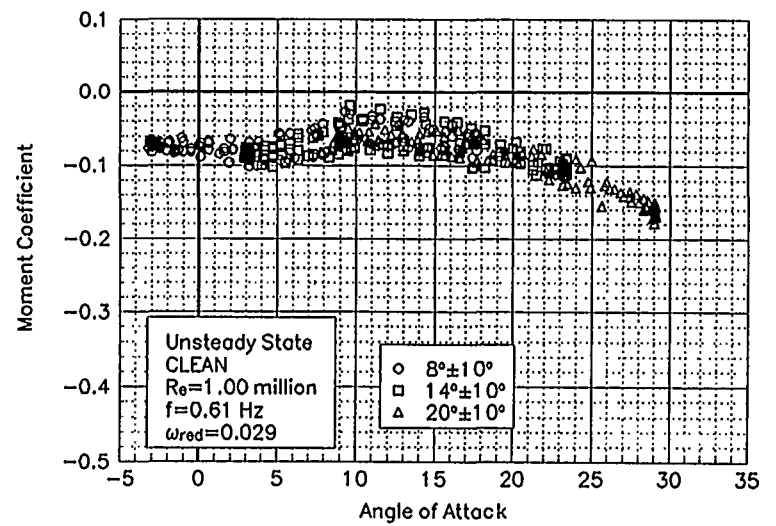
Figure C93. Moment coefficient vs α.

C-39

Figure C94. Lift coefficient vs α.

LS(1)-0421MOD
Clean
Re = 1 Million
$\omega_{red} = 0.055$
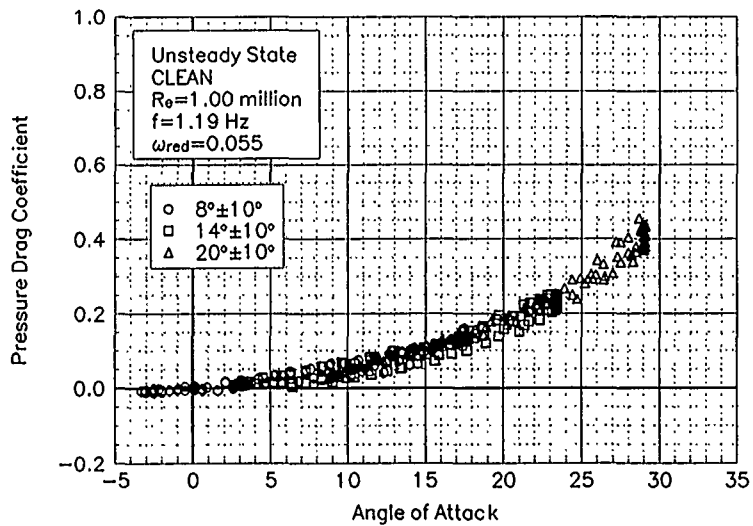
Figure C95. Pressure drag coefficient vs α.
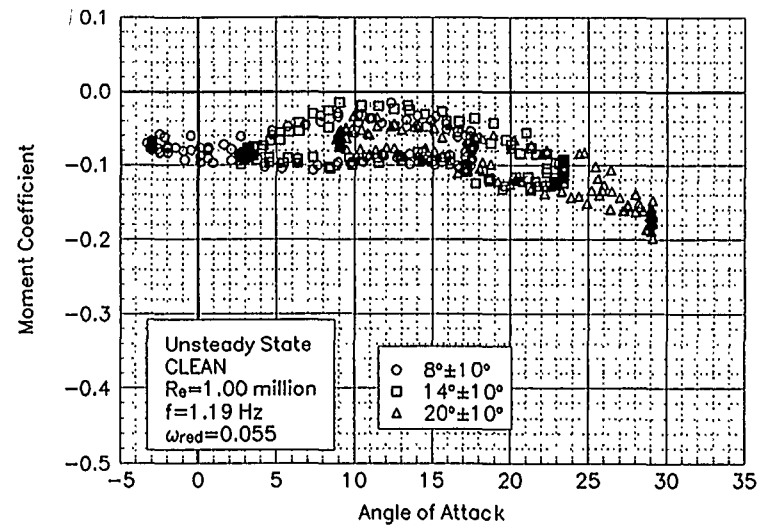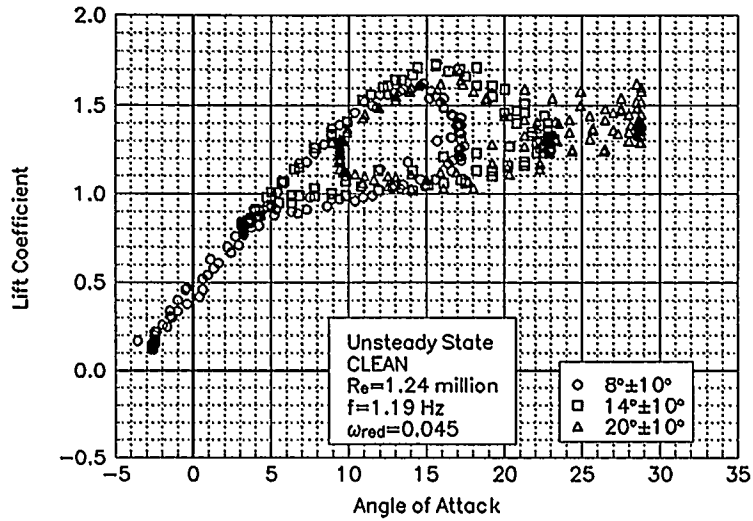

Figure C96. Moment coefficient vs α.

Figure C97. Lift coefficient vs α.

LS(1)-0421MOD
Clean
Re = 1 Million
$\omega_{red} = 0.085$
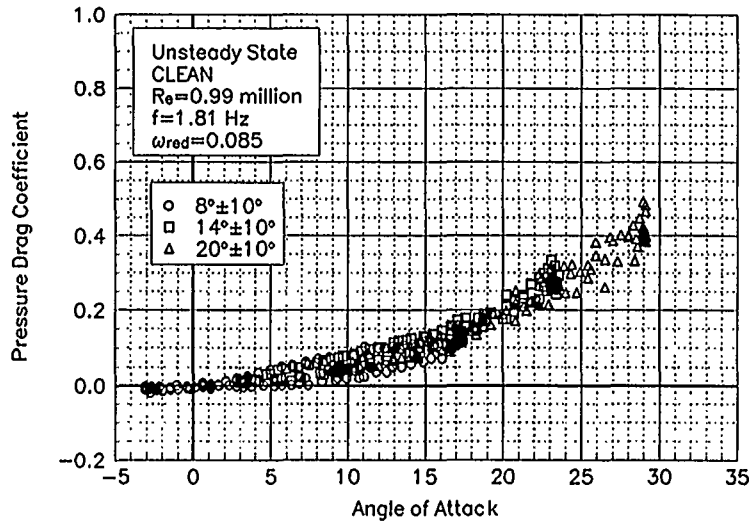
Figure C98. Pressure drag coefficient vs α.
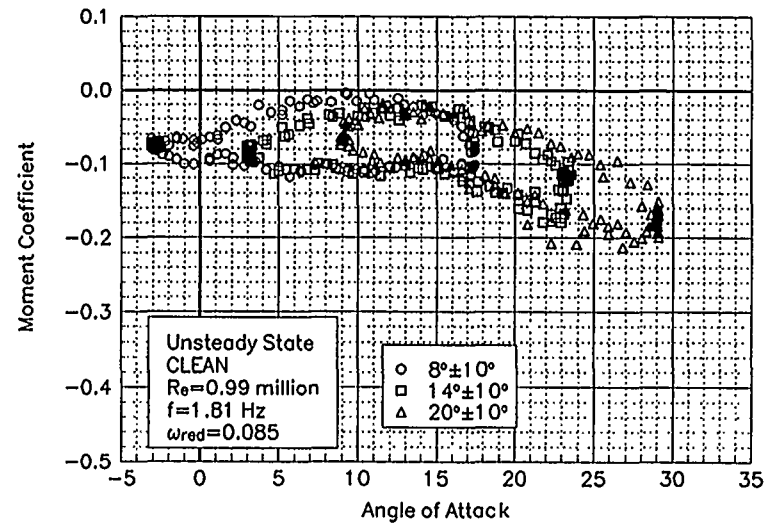
Figure C99. Moment coefficient vs α.

C-41
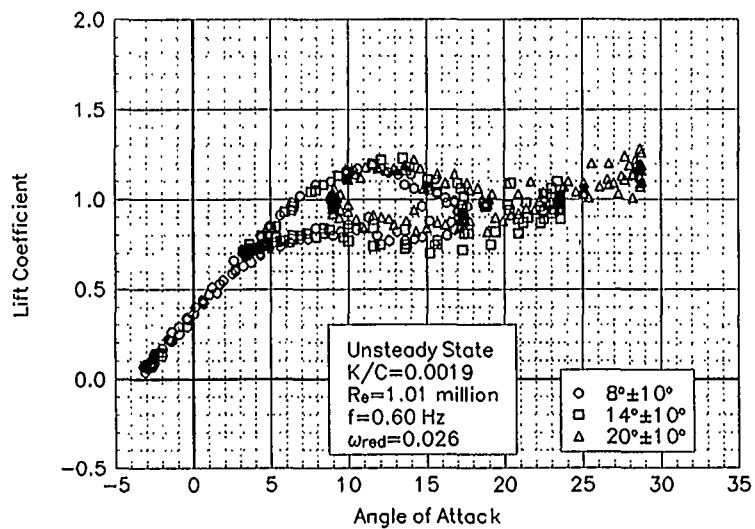
Figure C100. Lift coefficient vs α.

LS(1)-0421MOD
LEGR
Re = 1 Million
$\omega_{red} = 0.026$
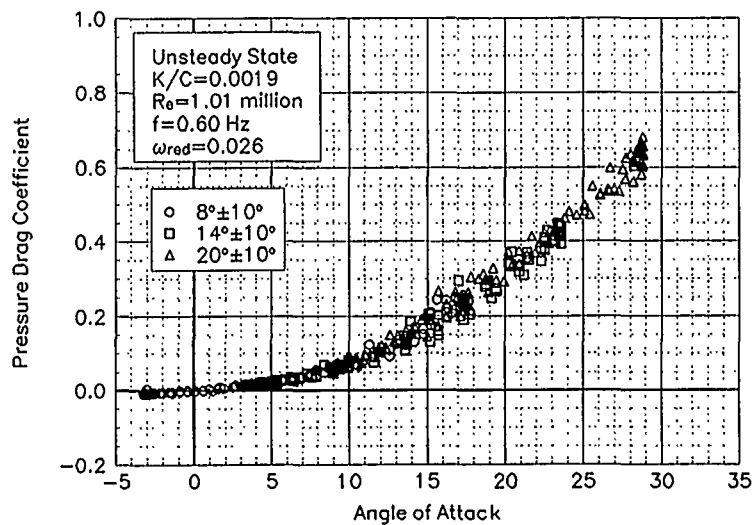
Figure C101. Pressure drag coefficient vs α.
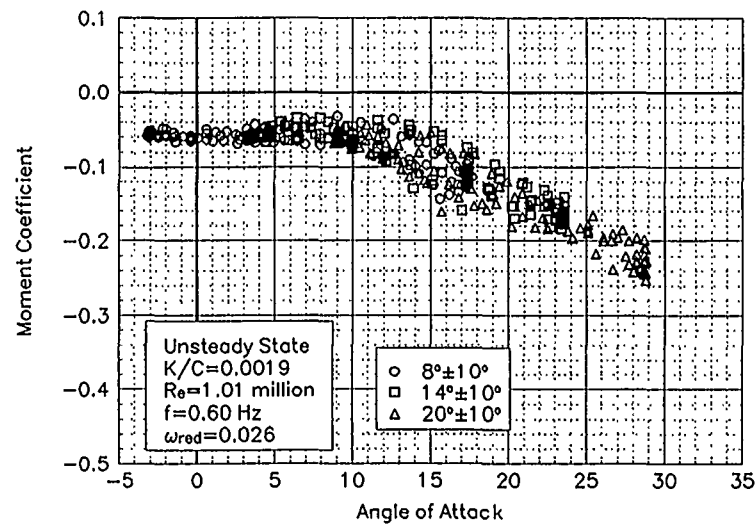
Figure C102. Moment coefficient vs α.
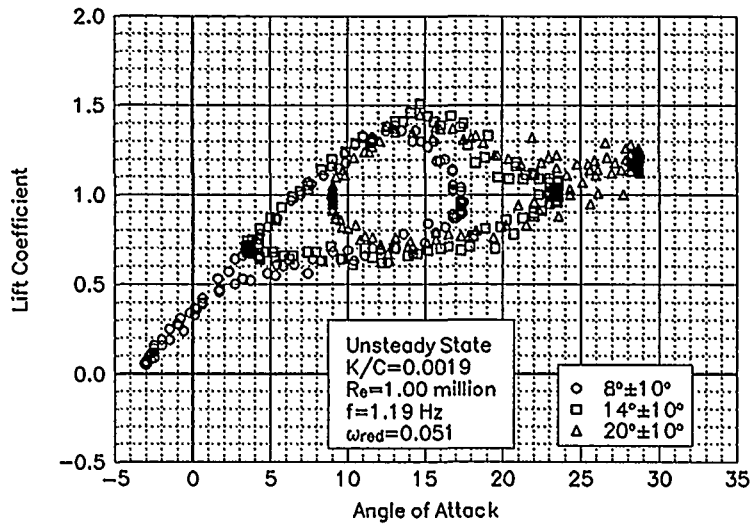
Figure C103. Lift coefficient vs α.

LS(1)-0421MOD
LEGR
Re = 1 Million
$\omega_{red} = 0.051$
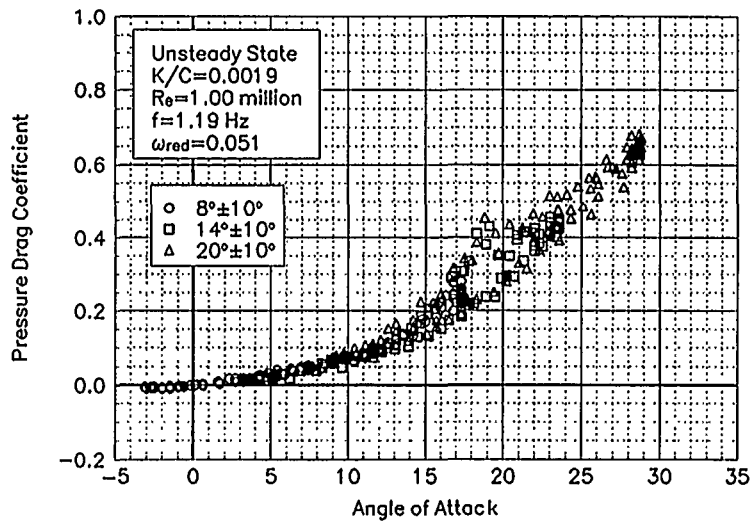
Figure C104. Pressure drag coefficient vs α.
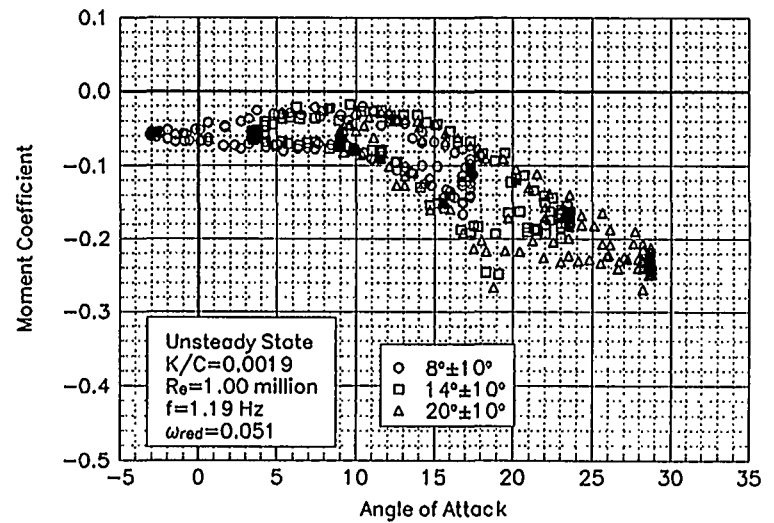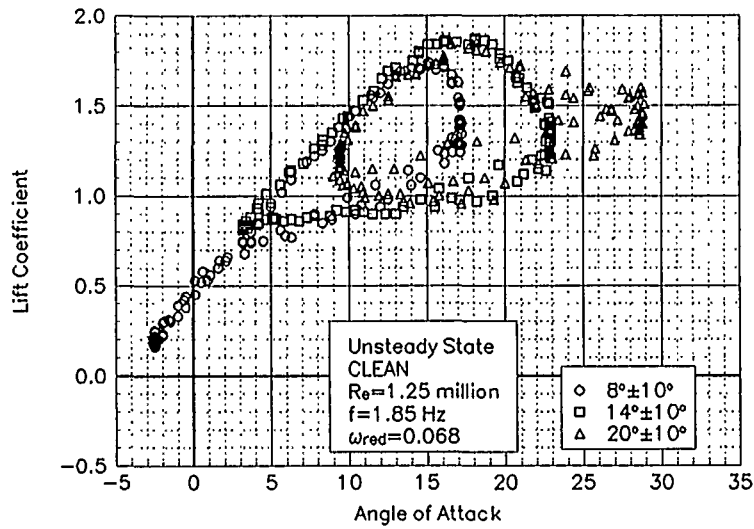

Figure C105. Moment coefficient vs α.
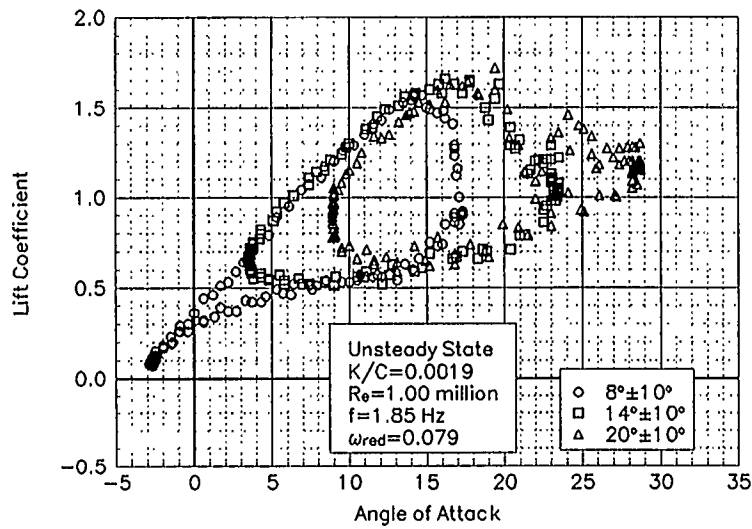
Figure C106. Lift coefficient vs α.

LS(1)-0421MOD
LEGR
Re = 1 Million
$\omega_{red} = 0.079$
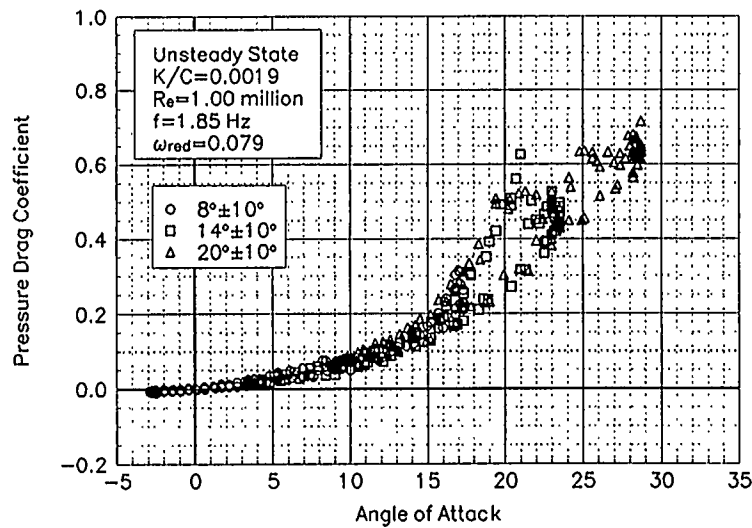
Figure C107. Pressure drag coefficient vs α.
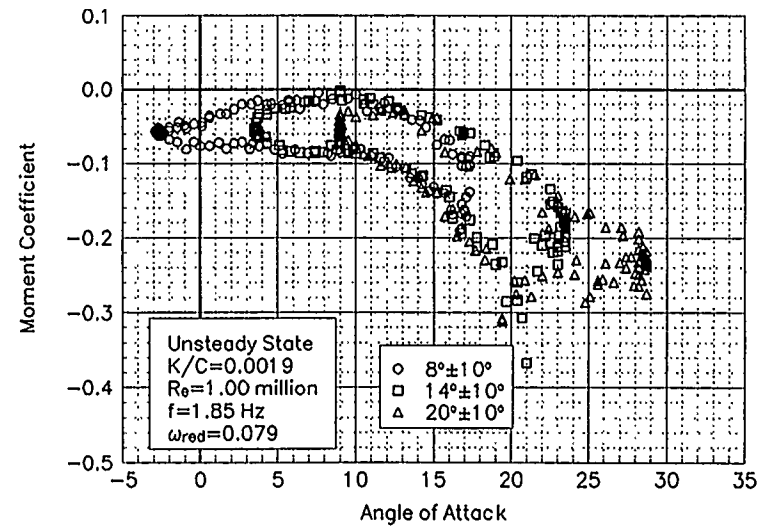
Figure C108. Moment coefficient vs α.

Unsteady Airfoil Characteristics

± 10° Sine

Re = 1.25 Million
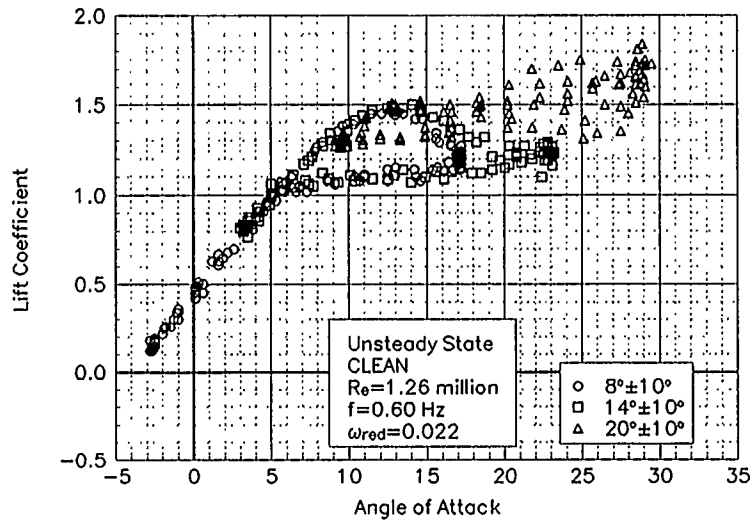
Figure C109. Lift coefficient vs α.

**LS(1)-0421MOD
Clean
Re = 1.25 Million
ω_{red} = 0.022**
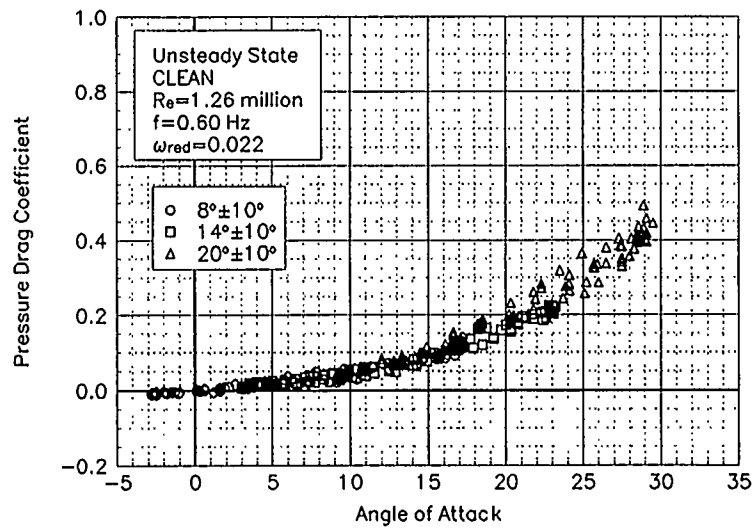
Figure C110. Pressure drag coefficient vs α.
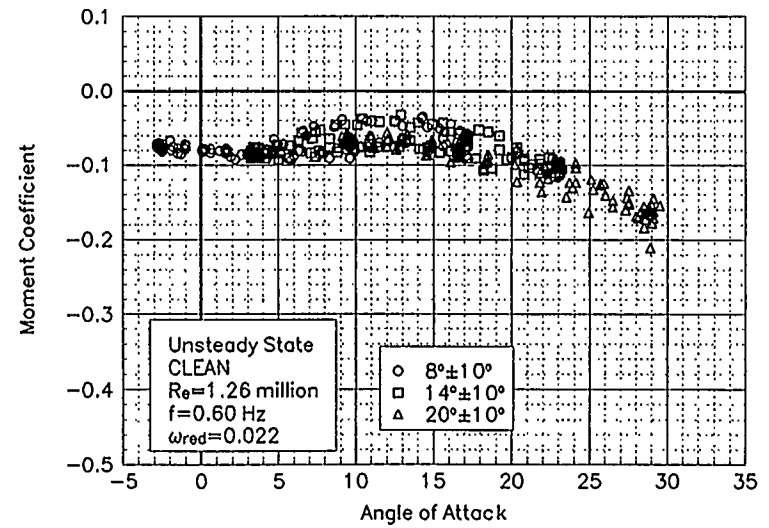
Figure C111. Moment coefficient vs α.

C-46

Figure C112. Lift coefficient vs α.

LS(1)-0421MOD
Clean
Re = 1.25 Million
$\omega_{red} = 0.045$
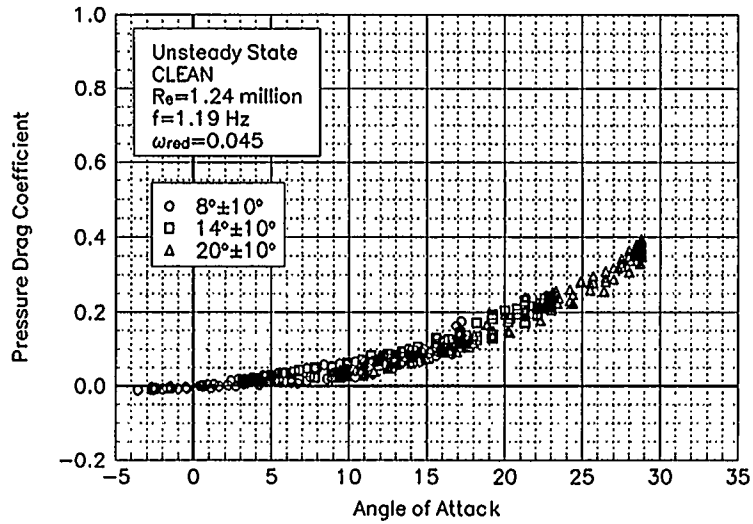
Figure C113. Pressure drag coefficient vs α.
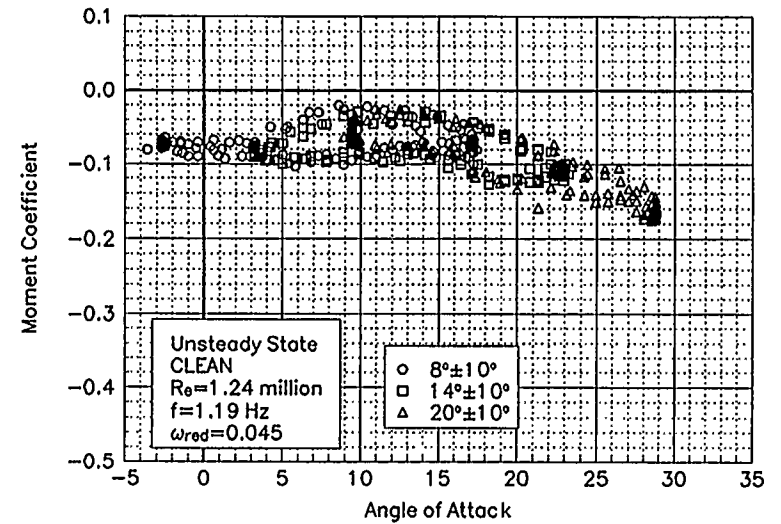
Figure C114. Moment coefficient vs α.

Figure C115. Lift coefficient vs α.

LS(1)-0421MOD
Clean
Re = 1.25 Million
$\omega_{red} = 0.068$
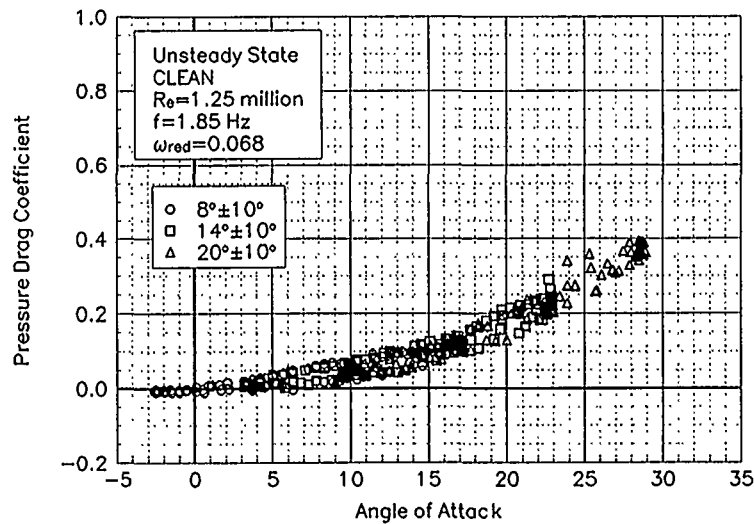
Figure C116. Pressure drag coefficient vs α.
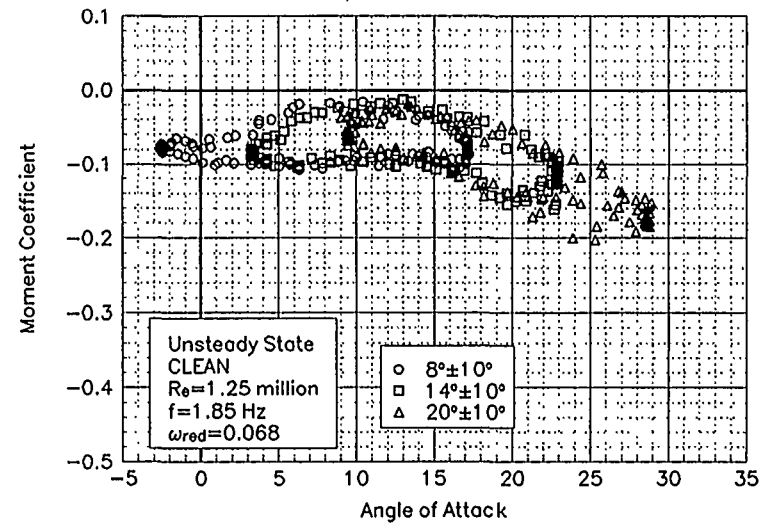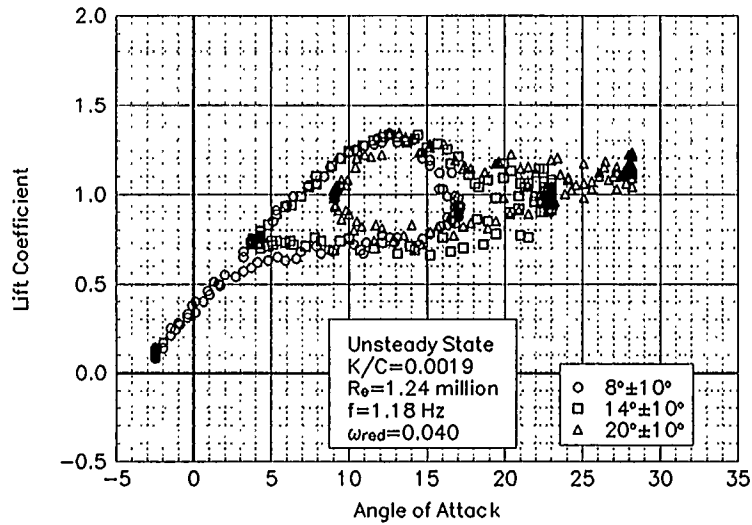

Figure C117. Moment coefficient vs α.
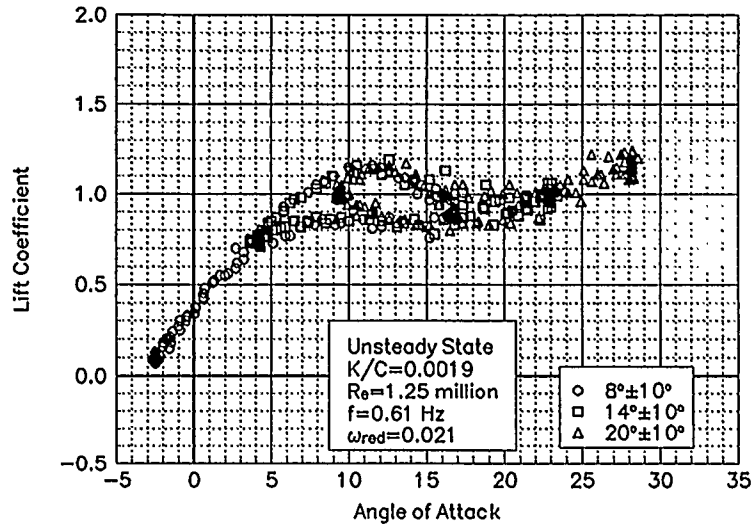
Figure C118. Lift coefficient vs α.
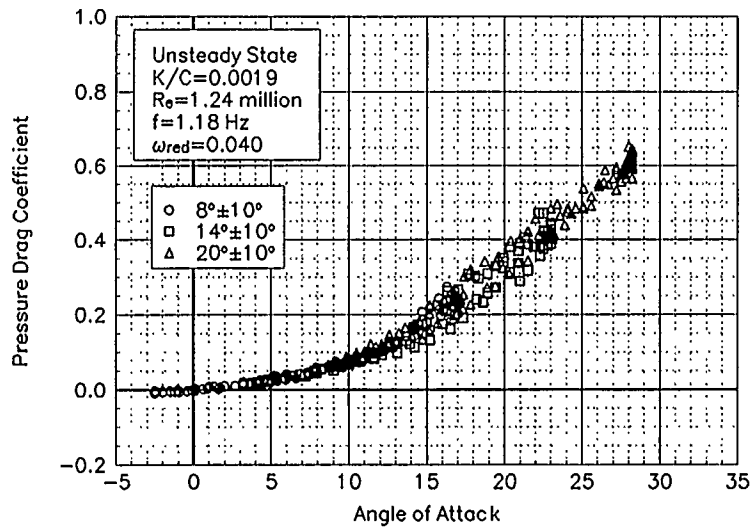
LS(1)-0421MOD
LEGR
Re = 1.25 Million
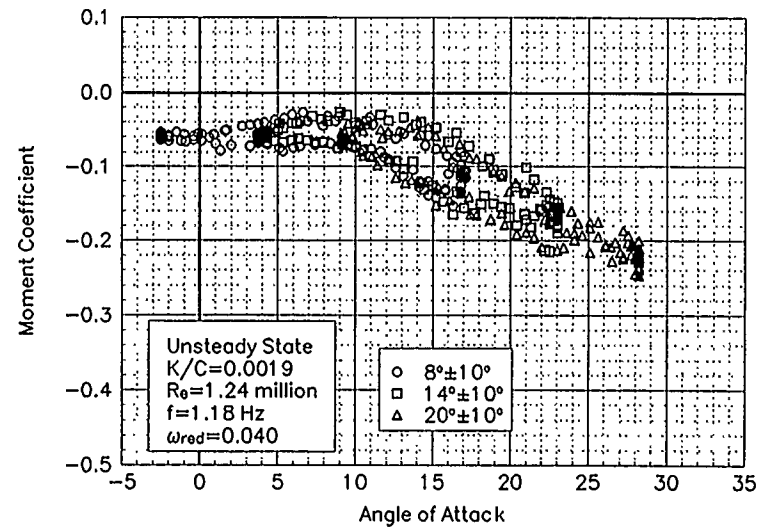$\omega_{red} = 0.021$
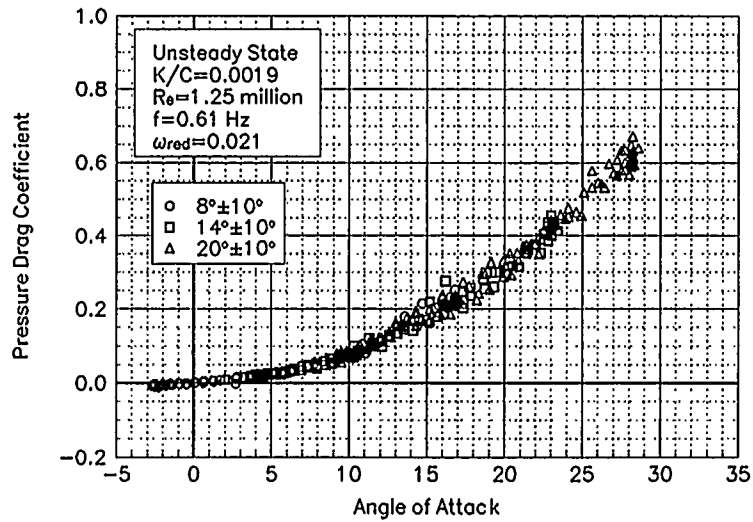
Figure C119. Pressure drag coefficient vs α.
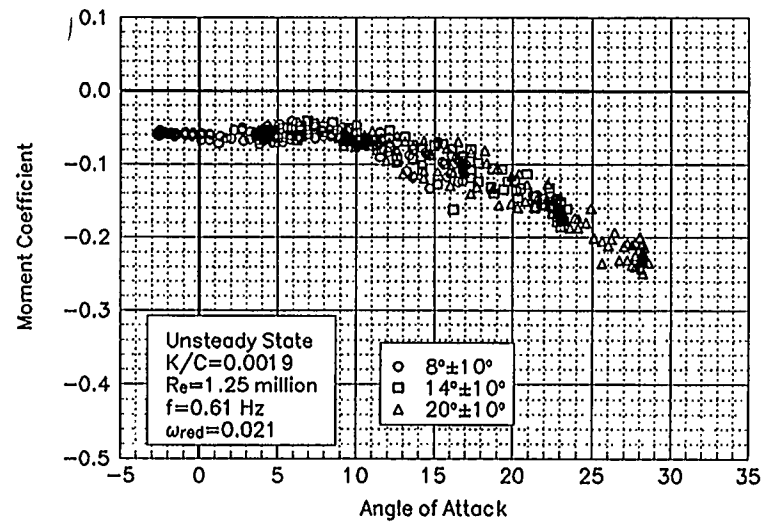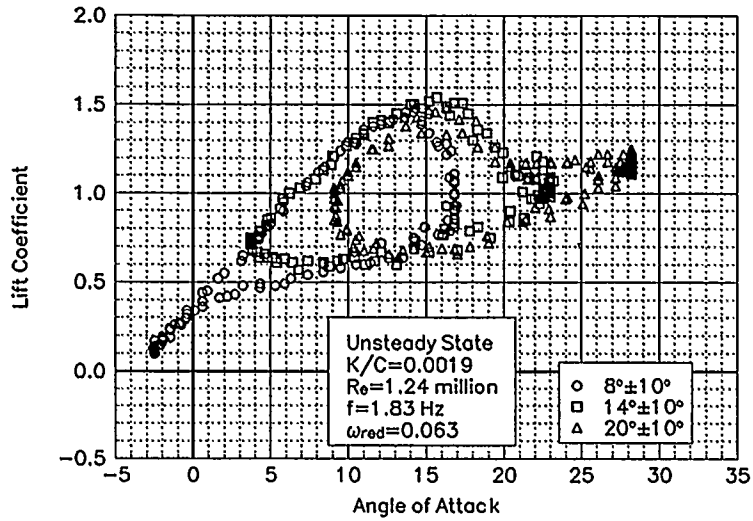

Figure C120. Moment coefficient vs α.

C-49

Figure C121. Lift coefficient vs α.

LS(1)-0421MOD
LEGR
Re = 1.25 Million
$\omega_{red} = 0.040$

Figure C122. Pressure drag coefficient vs α.

Figure C123. Moment coefficient vs α.

Figure C124. Lift coefficient vs α.

LS(1)-0421MOD
LEGR
Re = 1.25 Million
$\omega_{red} = 0.063$
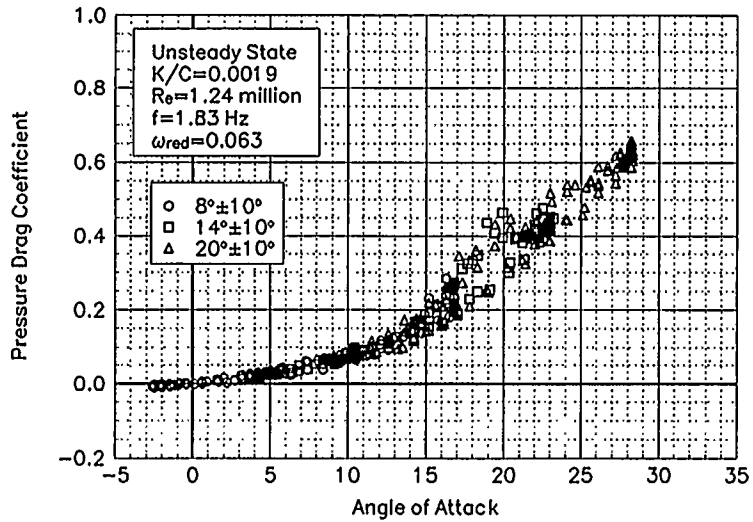
Figure C125. Pressure drag coefficient vs α.
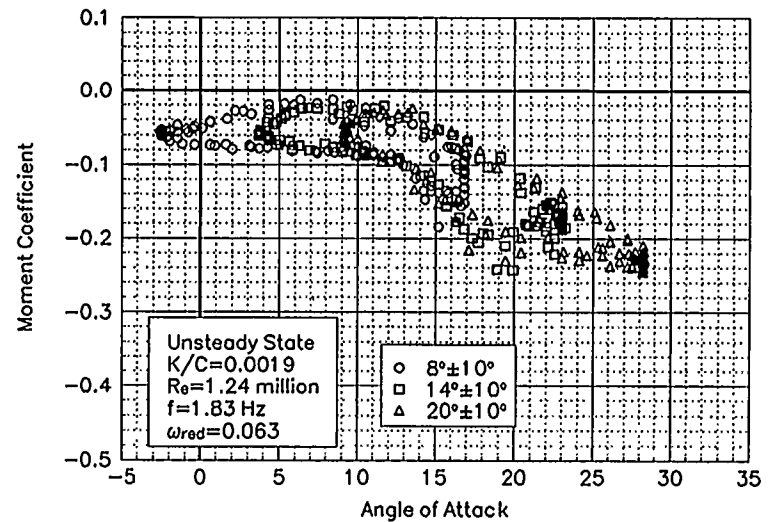
Figure C126. Moment coefficient vs α.

Unsteady Airfoil Characteristics

± 10° Sine

Re = 1.5 Million
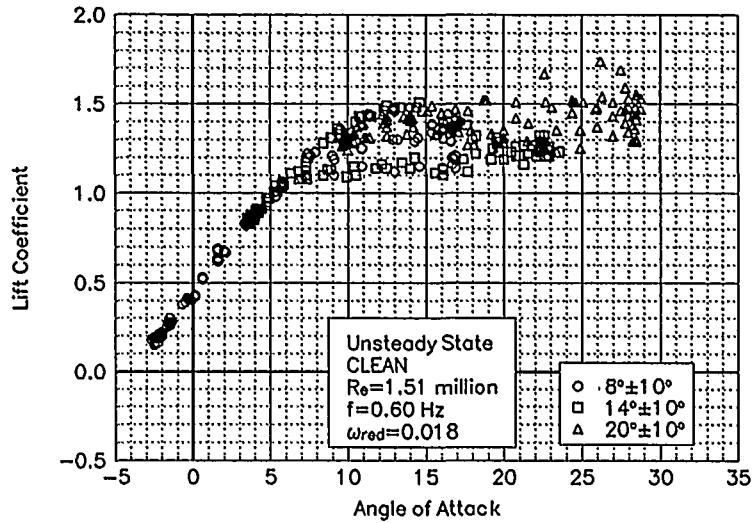
Figure C127. Lift coefficient vs α.

**LS(1)-0421MOD
Clean
Re = 1.5 Million
$\omega_{red} = 0.018$**
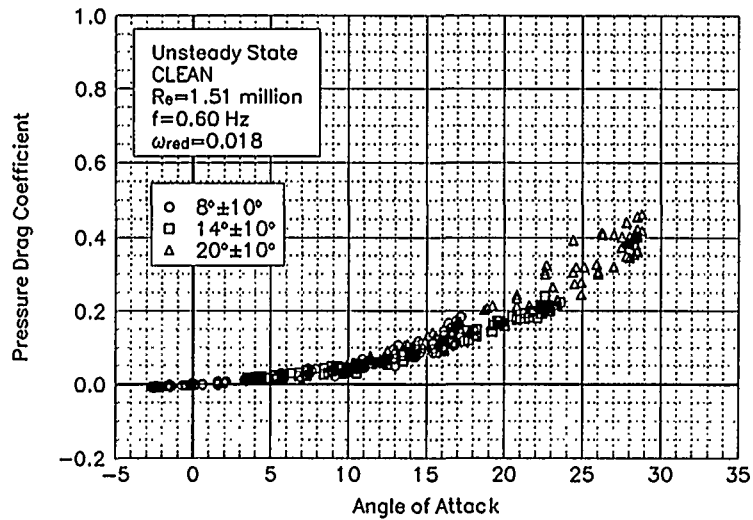
Figure C128. Pressure drag coefficient vs α.
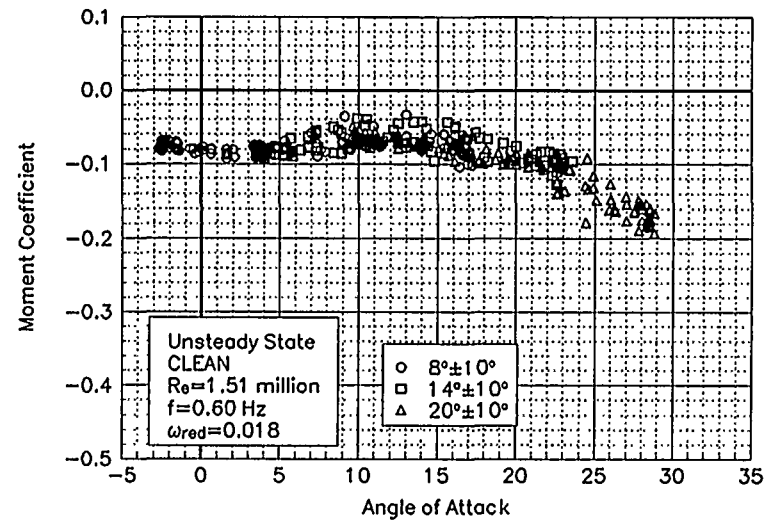
Figure C129. Moment coefficient vs α.
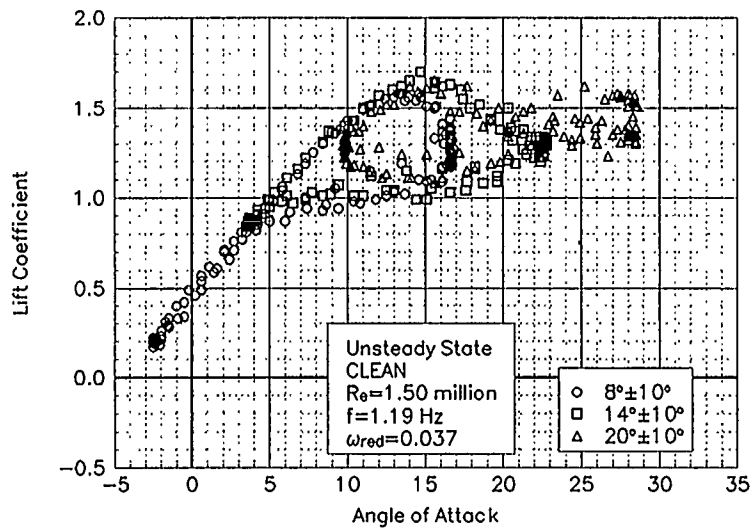
Figure C130. Lift coefficient vs α.

LS(1)-0421MOD
Clean
Re = 1.5 Million
$\omega_{red} = 0.037$
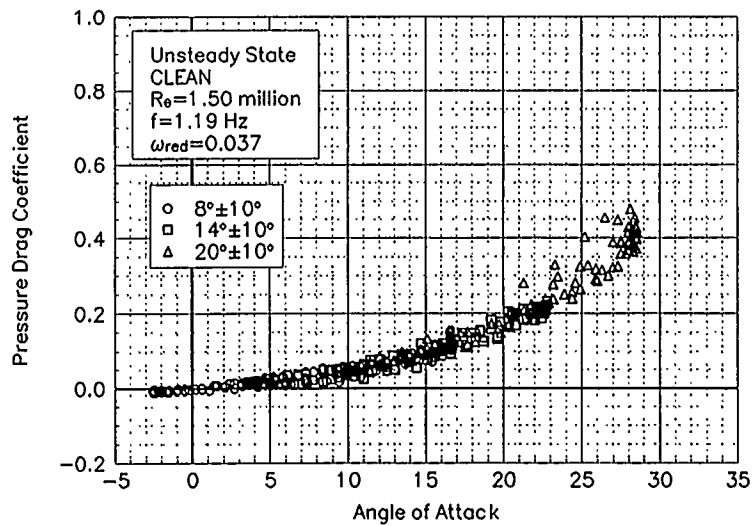
Figure C131. Pressure drag coefficient vs α.
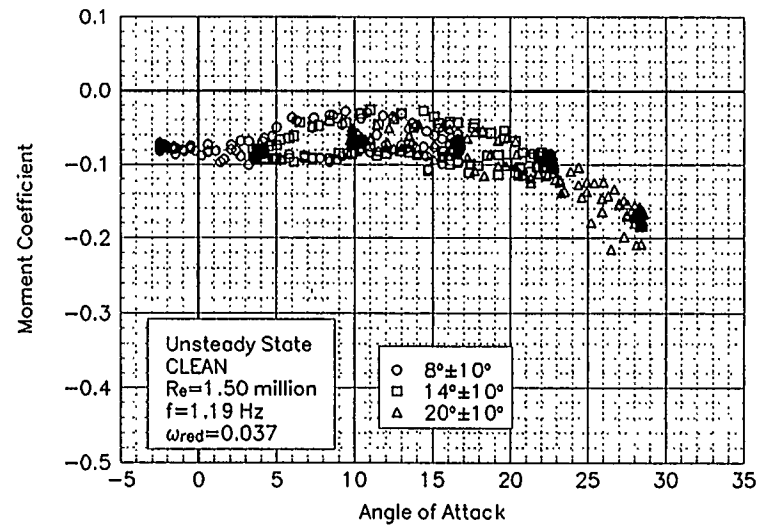
Figure C132. Moment coefficient vs α.
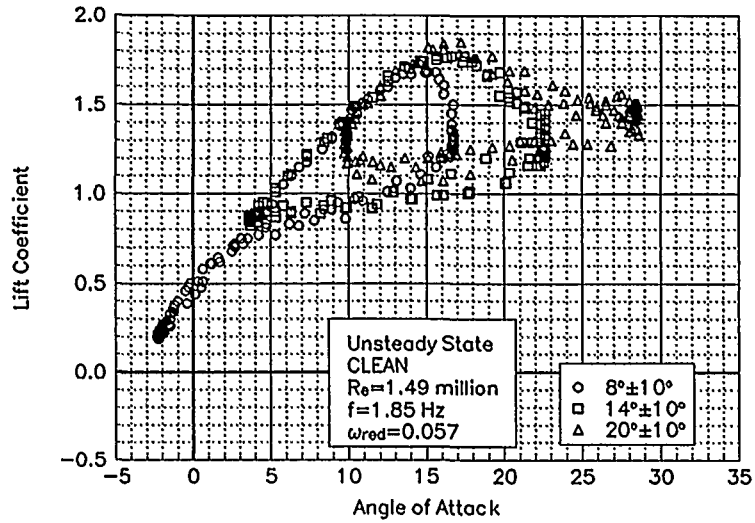
Figure C133. Lift coefficient vs α.

Figure C134. Pressure drag coefficient vs α.

LS(1)-0421MOD
Clean
Re = 1.5 Million
$\omega_{red} = 0.057$
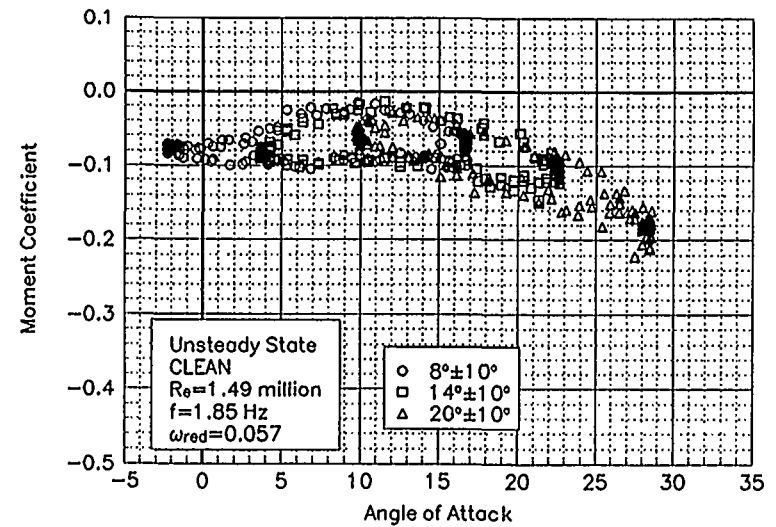
Figure C135. Moment coefficient vs α.
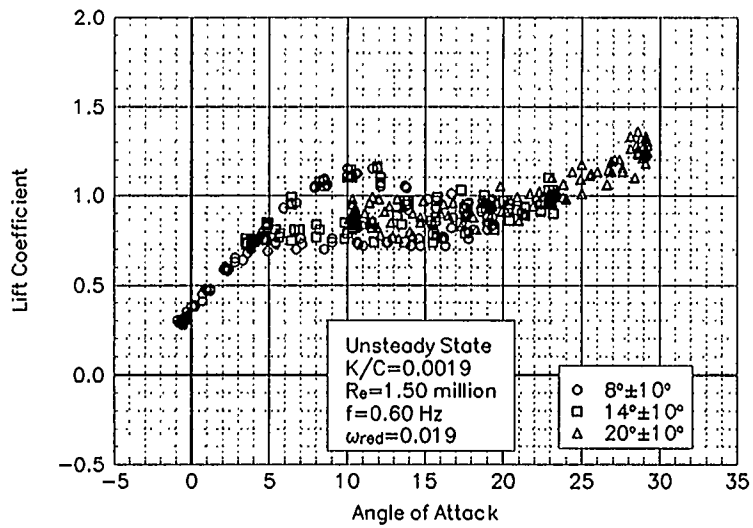
Figure C136. Lift coefficient vs a.

LS(1)-0421MOD
LEGR
Re = 1.5 Million
$\omega_{red} = 0.019$
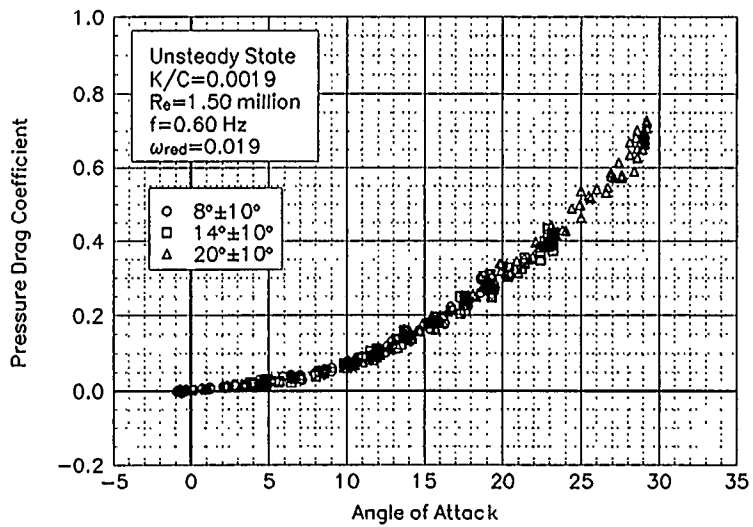
Figure C137. Pressure drag coefficient vs a.

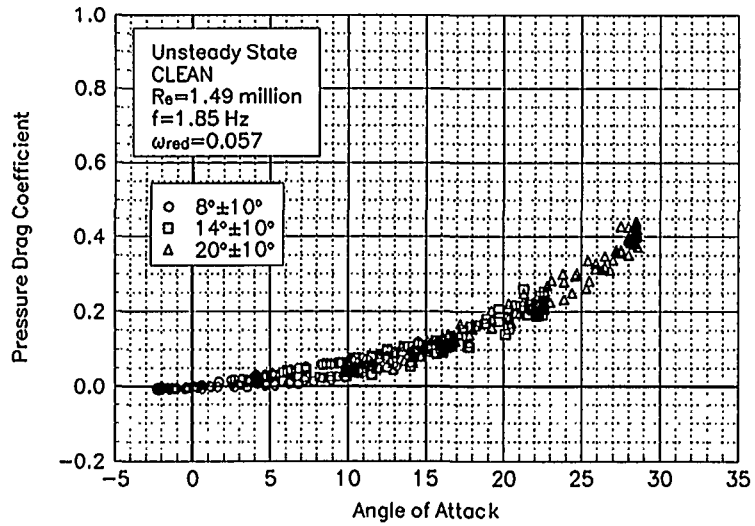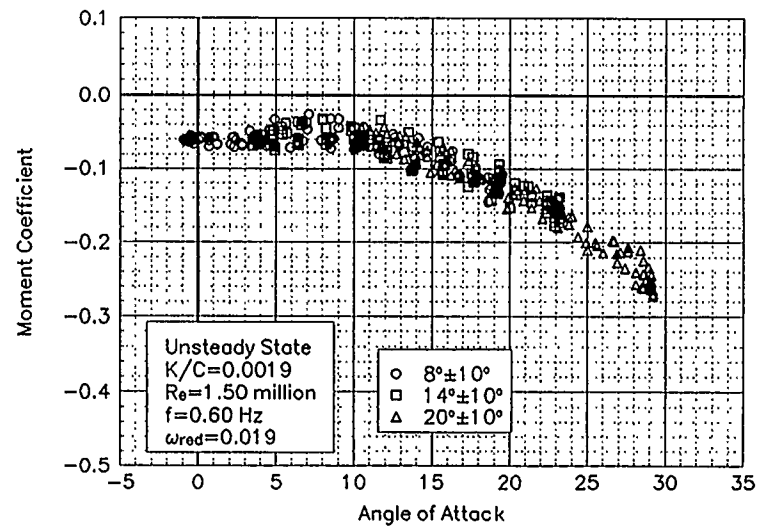Figure C138. Moment coefficient vs a.
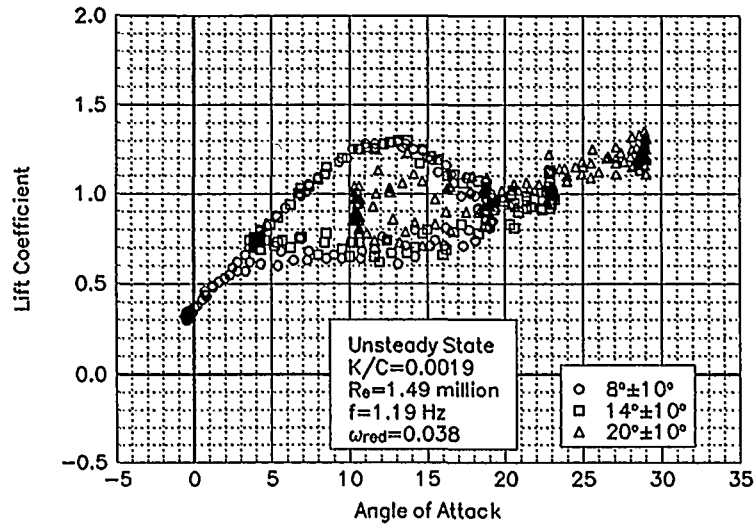
Figure C139. Lift coefficient vs α.

LS(1)-0421MOD
LEGR
Re = 1.5 Million
$\omega_{red} = 0.038$
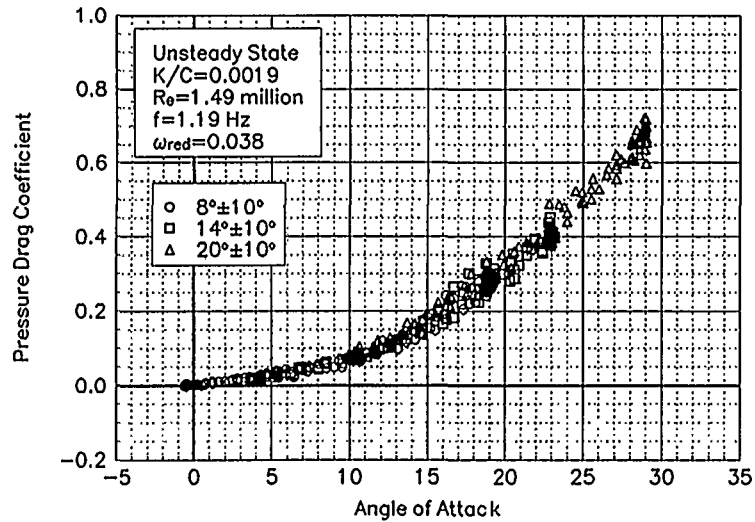
Figure C140. Pressure drag coefficient vs α.
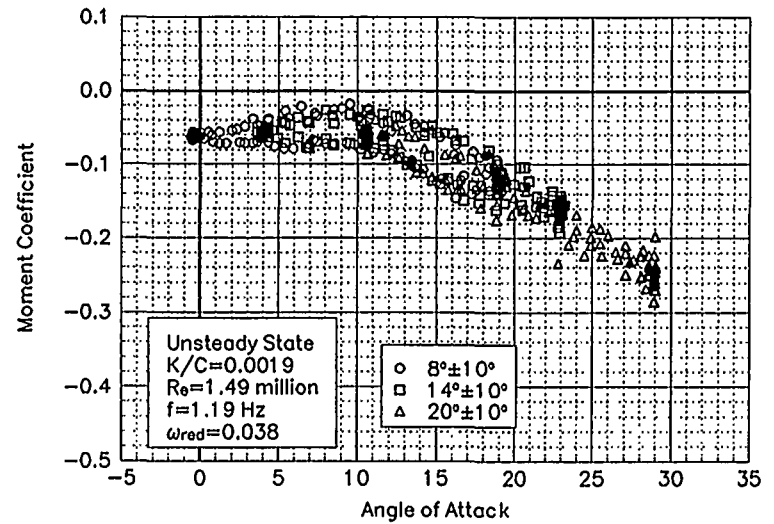
Figure C141. Moment coefficient vs α.
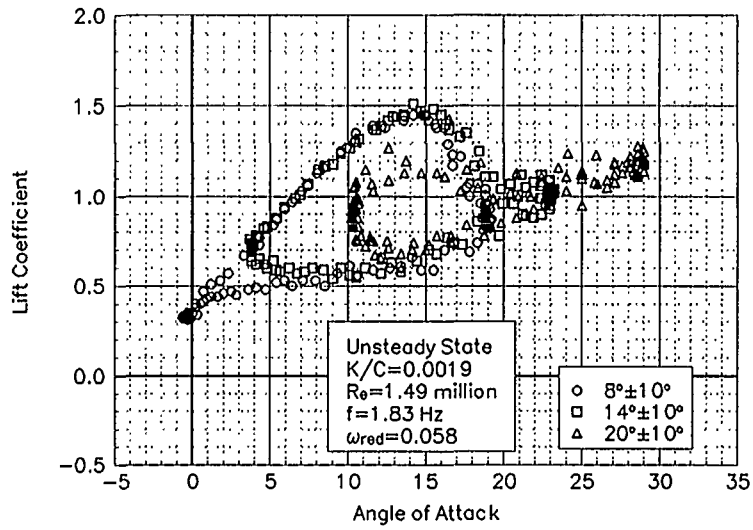
Figure C142. Lift coefficient vs α.

LS(1)-0421MOD
LEGR
Re = 1.5 Million
$\omega_{red} = 0.058$
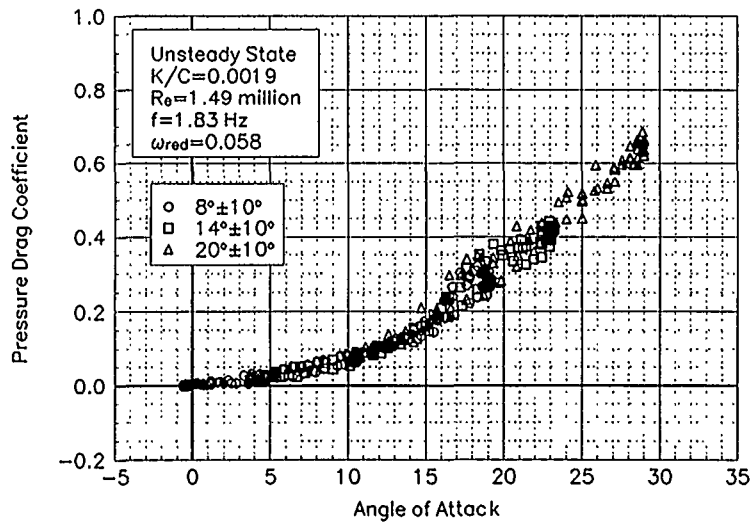
Figure C143. Pressure drag coefficient vs α.
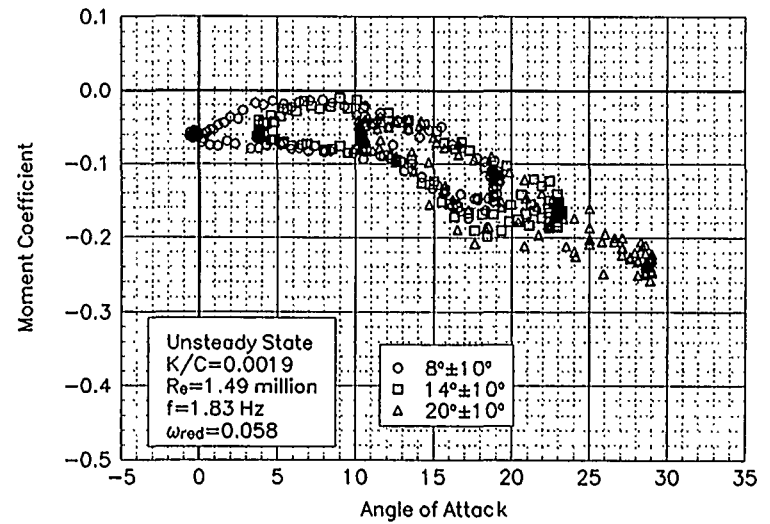
Figure C144. Moment coefficient vs α.

REPORT DOCUMENTATION PAGE

Public reporting burden for this collection of information is estimated to average 1 hour per response, including the time for reviewing instructions, searching existing data sources, gathering and maintaining the data needed, and completing and reviewing the collection of information. Send comments regarding this burden estimate or any other aspect of this collection of information, including suggestions for reducing this burden, to Washington Headquarters Services, Directorate for Information Operations and Reports, 1215 Jefferson Davis Highway, Suite 1204, Arlington, VA 22202-4302, and to the Office of Management and Budget, Paperwork Reduction Project (0704-0188), Washington, DC 20503.

1.	2. REPORT DATE December 1995	3. REPORT TYPE AND DATES COVERED Subcontract Report

4. TITLE AND SUBTITLE
Effects of Grit Roughness and Pitch Oscillations on the LS(1)-0421MOD Airfoil

6. AUTHOR(S)
R. L. Reuss, M. J. Hoffmann, G. M. Gregorek

5. FUNDING NUMBERS

C:

TA: WE618120

7. PERFORMING ORGANIZATION NAME(S) AND ADDRESS(ES)
Dr. Gerald Gregorek
The Ohio State University
Aero & Astronautical Research
2300 West Case Road
Columbus, Ohio 43220
(614) 292-5491

8. PERFORMING ORGANIZATION REPORT NUMBER

9. SPONSORING/MONITORING AGENCY NAME(S) AND ADDRESS(ES)

National Renewable Energy Laboratory
1617 Cole Blvd.
Golden, CO 80401-3393

10. SPONSORING/MONITORING AGENCY REPORT NUMBER

TP-442-6473
DE96000493

11. SUPPLEMENTARY NOTES

NREL Technical Monitor: C. P. Butterfield

12a. DISTRIBUTION/AVAILABILITY STATEMENT
National Technical Information Service
U.S. Department of Commerce
5285 Port Royal Road
Springfield, VA 22161

12b. DISTRIBUTION CODE

UC-1211

13. ABSTRACT *(Maximum 200 words)*

An LS(1)-0421MOD airfoil model was tested in The Ohio State University Aeronautical and Astronautical Research Laboratory (OSU/AARL) 3x5 subsonic wind tunnel (3x5) under steady flow and stationary model conditions, and also with the model undergoing pitch oscillations. In order to study the possible extent of performance loss due to surface roughness, a leading edge grit roughness (LEGR) pattern was developed to simulate leading edge contamination. After baseline cases were completed, the LEGR was applied for both steady state and model pitch oscillation cases. The Reynolds numbers for steady state conditions were 0.75, 1, and 1.25 million, while the angle of attack ranged from -10° to +40°. With the model undergoing pitch oscillations, data was acquired at Reynolds numbers of 0.75, 1, 1.25, and 1.5 million, at frequencies of 0.6, 1.2, and 1.8 Hz. Two sine wave forcing functions were used; ±5.5° and ±10°, at mean angles of attack of 8°, 14°, and 20°. For this report, unsteady conditions refer to the model in pitch oscillation.

In general, the maximum unsteady lift coefficient was from 10% to 50% higher than the steady state maximum lift coefficient. Variation in the quarter chord pitching moment coefficient was nearly two times greater than steady state values at high angles of attack. These findings indicate the importance of considering the unsteady flow behavior occurring in wind turbine operation for accurate load estimates.

14. SUBJECT TERMS

wind energy; horizontal-axis wind turbine; wind tunnel test data; wind turbine airfoil

15. NUMBER OF PAGES

16. PRICE CODE

17. SECURITY CLASSIFICATION OF REPORT Unclassified	18. SECURITY CLASSIFICATION OF THIS PAGE Unclassified	19. SECURITY CLASSIFICATION OF ABSTRACT Unclassified	20. LIMITATION OF ABSTRACT UL